

# **Algebraic Representation and Geometric Interpretation of Hilbert Transformed Signals**

**Dissertation**

**zur Erlangung des akademischen Grades  
Doktor der Ingenieurwissenschaften  
(Dr.-Ing.)**

**der Technischen Fakultät  
der Christian-Albrechts-Universität zu Kiel**

Dipl.-Inf. Lennart Wietzke

Kiel

2011

1. Gutachter: Prof. Dr. Gerald Sommer
2. Gutachter: Prof. Dr. Michael Felsberg

Datum der mündlichen Prüfung: 7. Dezember 2011

Für Mailin



# Abstract

This thesis covers a fundamental problem of local phase based signal processing: the isotropic generalization of the classical one dimensional analytic signal (D. Gabor) to higher dimensional signal domains. The classical analytic signal extends a real valued one dimensional signal to a complex valued signal by means of the classical 1D Hilbert transform. This signal extension enables the complete analysis of local phase and local amplitude information for each frequency component in the sense of Fourier analysis. In case of two dimensional signal domains, e.g. for images, additional geometric information is required to characterize higher dimensional signals locally. The local geometric information is called orientation, which consists of the main orientation and apex angle for two superimposed one dimensional signals. The problem of two dimensional signal analysis is the fact that in general those signals could consist of an unlimited number of superimposed one dimensional signals with individual orientations. Local phase, amplitude and additional orientation information can be extracted by the monogenic signal (M. Felsberg and G. Sommer) which is always restricted to the subclass of intrinsically one dimensional signals, i.e. the class of signals which only make use of one degree of freedom within the embedding signal domain. In case of 2D images the monogenic signal enables the rotationally invariant analysis of lines and edges. In contrast to the 1D analytic signal the monogenic signal extends all real valued signals of dimension  $n$  to a  $(n + 1)$  - dimensional vector valued monogenic signal by means of the generalized first order Hilbert transform, which is also known as the Riesz transform. The analytic signal and the monogenic signal show that a direct relation between analytical signals and their algebraic representation exists. This fact has motivated the work and the results of this thesis, namely the extension of the 2D monogenic signal to more general 2D analytic signals, their algebraic representation, and their most geometric embedding. In case of more general 2D signals the geometric algebra will be shown to be a natural representation, and the conformal space as the geometric embedding for the signal interpretation. In this thesis we present 2D analytic signals as generalizations of the 2D monogenic signal which now extend the original 2D signal to a multi-vector valued signal in homogeneous conformal space by means of higher order Hilbert transforms, and by means of a so called hybrid matrix geometric algebra representation. The 2D analytic signal and the more general multi-vector signal will be interpreted in conformal space which delivers a descriptive geometric interpretation and algebraic embedding of signals. In case of 2D image signals the 2D analytic signal and the multi-vector signal enable the rotationally invariant analysis of lines, edges, corners and junctions in one unified framework. Furthermore, additional local curvature can be determined by first order generalized Hilbert transforms without the need of derivatives. This so called conformal monogenic signal can be defined for any signal domain.



# Danksagung

Auf dieser Seite möchte ich mich bedanken bei denjenigen, die mich zu dieser nun hier vorliegenden Arbeit geführt und begleitet haben. Zuallererst danke ich meinem Doktorvater Herrn Professor Sommer, der mir diese Arbeit überhaupt erst ermöglicht hat im Rahmen des vierjährigen Projektes *SO-320/4-2* (Gerald Sommer) der deutschen Forschungsgesellschaft (DFG). Herr Sommer hat nicht nur mir, sondern auch meinen Kollegen aus der Forschungsgruppe der Kognitiven Systeme jederzeit jegliche Freiheitsgrade bei vielen Diskussionen, Kritiken und neuen Anregungen sowie Literaturhinweisen gelassen, ähnlich wie es mir die Clifford Algebra geboten hat. Besonders möchte ich mich auch für die Möglichkeit und Unterstützung für die vielen Reisen rund um die Welt bedanken. Ich danke auch meinem Gutachter Professor Felsberg für seine grundlegenden Arbeiten, die mich zu dieser Arbeit motiviert haben. Als nächstes bedanke ich mich bei meinem ehemaligen Kollegen Oliver Fleischmann für die fruchtbare Zusammenarbeit und die vielen Diskussionen, Kritiken und Ideen sowie den Spaß auf unseren Reisen. Ich wünsche ihm hiermit alles Gute für seinen weiteren akademischen Weg. Weiterhin möchte ich mich bei meinen ehemaligen Kollegen bedanken: Dr. Christian Gebken und Dr. Florian Hoppe, mit denen ich viel Spaß auch neben der Forschung, z.B. auf unseren gemeinsamen Reisen hatte. Ich danke auch Dr. Sven Buchholz, Dr. Stephan Zeitschel, Dr. habil. Christian Perwaß und Dr. Di Zang. Ich bedanke mich auch bei meinen drei ehemaligen Diplomanden, nochmals bei Oliver Fleischmann sowie Anne Sedlazeck und Felix Thomsen, die alle nach ihrem Diplom den Weg zur Promotion angetreten haben. Ich wünsche ihnen viel Erfolg dabei. Vielen Dank auch an Frau Armgard Wichmann, die sich wie jede Sekretärin am Institut für Informatik mit technischen Dingen wie z.B. mit Latex und Linux auseinandersetzen musste. Ein besonderer Dank geht auch an meine liebe Familie, meine Eltern Ernst-Otto und Christine Wietzke, die mir die Schulzeit am Einfelder Gymnasium bei Dr. Schwarze und das Studium an der TU-Clausthal bei Professor Lex ermöglicht haben, sowie an meine Schwester Kirstin Wischatta. Ich danke auch meiner lieben Partnerin Mailin Schmidt, die mich in der Zeit der Promotion mit viel humorvollem Verständnis ertragen konnte. Ich danke auch herzlich meinem besten Freund Sebastian Eiteljörge aus der Studienzeit in Clausthal-Zellerfeld sowie meinem besten Schulfreund Torben Kuschel. Diese Arbeit ist auch in Gedenken an meine Großeltern und besonders an den Autodidakten Hans Anker. Als letztem möchte ich noch dem mir bis jetzt unbekanntem Pförtner danken, der mir jeden Morgen frühzeitig und ohne Einsatz meiner Chipkarte das Tor zur Universität geöffnet hatte, sobald er aus der Ferne das Geräusch meines Zuffenhausener Automobiles vernehmen konnte.





# Contents

<b>1. Introduction</b>	<b>13</b>
1.1. The Analytic Signal . . . . .	18
1.1.1. Analytic Functions . . . . .	20
1.2. 2D Signal Classification . . . . .	20
1.3. Higher Order Generalized Hilbert Transforms . . . . .	22
1.3.1. First Order Hilbert Transform . . . . .	23
1.3.2. Second Order Hilbert Transform . . . . .	23
1.3.3. Relation of Hilbert Transforms to Radon Transform . . . . .	24
1.3.4. The Partial Hilbert Transform . . . . .	27
1.4. The Poisson Scale Space . . . . .	29
1.4.1. Second Order Hilbert Transform . . . . .	31
1.4.2. Third Order Hilbert Transform . . . . .	34
<b>2. The Monogenic Signal Revisited</b>	<b>37</b>
2.1. Local Signal Model . . . . .	37
2.2. First Order Hilbert Transform in Radon Space . . . . .	38
2.3. Interpretation of the Monogenic Signal . . . . .	38
2.3.1. Phase Vector . . . . .	40
2.3.2. Main Orientation . . . . .	40
2.4. Exploiting the Properties of Monogenic Signals . . . . .	43
<b>3. The Conformal Monogenic Signal</b>	<b>47</b>
3.1. Locally Curved Signal Model . . . . .	48
3.2. The Conformal Space . . . . .	48
3.3. 3D Hilbert Transforms in Conformal Space . . . . .	49
3.4. 3D Radon Transform in Conformal Space . . . . .	51
3.5. Local Signal Interpretation . . . . .	52
3.5.1. Local Signal Curvature . . . . .	54
3.5.2. Experimental Results . . . . .	57
3.6. The 3D Conformal Monogenic Signal . . . . .	57
<b>4. The Isotropic 2D Analytic Signal</b>	<b>63</b>
4.1. Second Order Hilbert Transform in Radon Space . . . . .	64
4.2. Third Order Hilbert Transform in Radon Space . . . . .	64
4.3. Algebraic Signal Representations . . . . .	65
4.3.1. Geometric Algebra of Euclidean Space . . . . .	66

4.3.2.	Matrix Geometric Algebra . . . . .	72
4.3.3.	Inverse Element . . . . .	74
4.3.4.	The Homogeneous Conformal Geometric Algebra . . . . .	75
4.3.5.	The Projective Space . . . . .	78
4.3.6.	The Homogeneous Conformal Space . . . . .	78
4.3.7.	Reflection . . . . .	79
4.3.8.	Rotation . . . . .	79
4.3.9.	Translation . . . . .	79
4.3.10.	Hybrid Matrix Valued Signal Representation . . . . .	79
4.4.	Interpretation of the 2D Analytic Signal . . . . .	82
4.4.1.	Geometrical Signal Features . . . . .	82
4.4.2.	Homogeneous Signal . . . . .	83
4.4.3.	Structural Signal Features . . . . .	84
4.4.4.	Proof Outline . . . . .	87
4.5.	Experimental Results and Comparisons . . . . .	88
4.6.	Application: Dense Optical Flow Estimation . . . . .	90
<b>5.</b>	<b>The Multi-Vector Signal</b>	<b>93</b>
5.1.	Local Signal Modeling in Scale Space . . . . .	93
5.2.	Signal Extension by Hilbert Transforms . . . . .	94
5.3.	Signal Intelligence in Radon Space . . . . .	96
5.4.	Algebraic Signal Representation . . . . .	100
5.5.	Geometry from the Multi-Vector Signal . . . . .	102
5.6.	Structure from the Multi-Vector Signal . . . . .	105
5.6.1.	The Multi-Vector Signal Generalizes the 2D Monogenic Signal . . . . .	105
5.7.	Applications . . . . .	107
5.7.1.	Multi-Layer Decomposition . . . . .	107
5.7.2.	Dense Optical Flow Estimation . . . . .	111
<b>6.</b>	<b>Conclusion and Outlook</b>	<b>115</b>
<b>A.</b>	<b>Proof: Geometric Information by the Multi-Vector Signal</b>	<b>119</b>
A.1.	Alternative . . . . .	122
<b>B.</b>	<b>Proof: Structural Information by the Multi-Vector Signal</b>	<b>125</b>
B.1.	Alternative . . . . .	127
<b>C.</b>	<b>Comparison: The Monogenic Curvature Tensor</b>	<b>129</b>
<b>D.</b>	<b>Comparison: The Structure Multi-Vector</b>	<b>131</b>
<b>E.</b>	<b>Implementation: The 2D Conformal Monogenic Signal</b>	<b>133</b>
<b>F.</b>	<b>Implementation: The 3D Conformal Monogenic Signal</b>	<b>135</b>

<b>G. Implementation: The Isotropic 2D Analytic Signal</b>	<b>137</b>
<b>H. Implementation: The Multi-Vector Signal</b>	<b>139</b>



# 1. Introduction

This thesis deals with local signal analysis of mainly two dimensions but also with signals of higher dimensional domains. But first of all what is signal analysis exactly? A given signal is known, but not the underlying process, with the task of being characterized or classified in such a way that certain signal features can be assigned to a local position within the signal. Therefore, each signal position will be mapped to a list of interesting local features. The most important question is: Which features does a certain signal carry? The pattern recognition community tries to answer this question and delivers a huge set of different approaches to characterize signals locally. In this thesis we concentrate on the transition of a cosine wave, i.e. signals will be locally described by a cosine wave with its amplitude, phase and frequency in the one dimensional case. Of course any other wave can be used as a reference signal model, e.g. any mother wavelet in wavelet analysis can be used. Anyway, we go on with the choice of using the cosine wave and try to find out how near a certain signal equals the model of a cosine wave. In this way, signal analysis can also be called "pattern matching", which is nothing else than comparing an arbitrary signal with a given pattern or a limited set of patterns. If we start with only one pattern to compare with our signal we can determine how close they come to each other. How can this be extended? Signal analysis should be able to map the original signal to the basis of the signal feature space since we only want to use a small set of patterns to speed up the process. If we use two patterns we should be able to be invariant against an arbitrary scaling factor  $a > 0$  of the signal. Why? If we compare the signal with two patterns we can divide the two results and cancel out some unknown scaling factor. Later on we will give examples on this idea. Now the question comes up how many patterns do we need? First of all, what is the mathematical operation of a comparison? And what patterns do we have to use? We will use the Hilbert transform convolution kernels for comparison in this thesis. And how can we make this comparison a local operation in such a way that we will not lose the spatial position of our comparison operation? We will make sure that this information will be saved by a windowed Fourier transform. How can this window be constructed? In signal analysis such a window will be formed by a filter which is parameterized by the spatial length of this window which coincides with the local frequency  $\nu$  of the assumed cosine wave. Please do not mix up the cosine wave, which is the local signal model, and the pattern, which will be used for comparison or convolution, respectively. Since a cosine wave can appear in many different ways as a local signal, we do not want to search for a static cosine wave with fixed phase  $\phi$ . Instead, we want to find every cosine wave with arbitrary transition (phase), which can change a cosine wave to a sine wave or a mix of both. Therefore, our pattern for comparison will not be the cosine wave itself but a transformation which will turn the given cosine wave with a given un-

## 1. Introduction

known phase into a cosine wave with a given unknown phase plus a shift of  $90^\circ$ . Which operator achieves this transformation? The derivative operator  $\mathcal{D}$  does this in such a way that the frequency of the wave  $g(x) = a \cos(\nu x + \phi)$  interferes with the amplitude  $a$ , i.e.  $\mathcal{D}\{g\}(x) = -\nu a \sin(\nu x + \phi)$ , which should be avoided. We are searching for a transformation which provides something of the kind:  $\mathcal{H}\{g\}(x) = a \sin(\nu x + \phi)$ , which is invariant against the frequency. As we already mentioned, this can be solved by the Hilbert transform  $\mathcal{H}$ . Since the Hilbert transform does not provide any filter kernel for the windowed Fourier transform, which makes sure that only a single frequency will be considered for signal analysis, the Hilbert transform has to be combined with such a filter kernel. The Gaussian filter and the difference of Gaussian is widely used for this task. Anyway, we will use the Poisson filter kernel, since it comes along with the Hilbert kernel in one and the same filter, which is called Cauchy kernel. Furthermore, it has been argued that the Poisson filter is optimum for phase based signal analysis [18]. Assuming that we have some operator like the Hilbert transform in combination with a frequency filter  $\mathcal{P}_s$ , we can obtain the amplitude  $a_\nu$  and phase  $\phi_\nu$  for a given frequency  $\nu$ . The so called scale space parameter  $s > 0$  of the Poisson filter corresponds to the frequency. The higher the frequency the smaller the scale space parameter  $s$  and viceversa. Assuming, we have an arbitrary signal  $g$ , we have to take a look at a single frequency by choosing the scale space parameter and applying the Poisson filter operator to the signal  $g$  and defining the so called even part of the signal  $g_s^e(x) = \mathcal{P}_s\{g\}(x)$  and the corresponding odd part  $g_s^o(x) = \mathcal{H}\{g_s^e\}(x)$ , we can now determine the phase and amplitude of the original signal for each scale space parameter  $s$  separately.

The aim of the thesis is to generalize this concept to two dimensions. Low level image analysis is often the first step of many computer vision tasks. Therefore, local signal features with geometrical and structural information determine the quality of subsequent higher level processing steps. It is important not to lose or to merge any of the original signal information within the local neighborhood of the test point<sup>1</sup>. The constraints of local signal analysis are: to span an orthogonal feature space (split of identity) and to be robust against stochastic and deterministic deviations between the actual signal and the assumed signal model.

One of the fundamental problems in signal processing is a good signal representation which enables signal analysis of important features. Such a signal feature is the local phase information which is a robust feature with respect to noise, contrast and illumination changes [34, 20, 19]. In case of image signals it is shown in [47] that the original signal can be recovered to a fairly large extend by using only its phase information while setting its amplitude information to unity (typically  $\frac{1}{f}$ ), see also Figure (1.1). In contrast to that, if only the amplitudes are obtained and the phases are set to zero, the recovered image signal is completely indiscernible. Therefore, phase based signal processing has found success in many applications, such as disparity estimation of stereo [20], matching [10], face recognition [75], etc.

---

<sup>1</sup>There is no method of signal analysis which is universal in respect of any arbitrary local 2D structure. Hence, it is necessary to formulate a model of local signal structure as basis of the analysis. The great challenge is the search for a most general model which can cope with as much as possible variants of local signal structure.



Figure 1.1.: This illustration by T. Bülow is one of the main motivations of this thesis. Top row from left to right: Original image of J. Fourier and D. Hilbert. Both images are transformed into the frequency domain by a two dimensional Fourier transform and each linear independent frequency vector is determined by its unique phase and amplitude information. Bottom row left image is reconstructed by the phase of J. Fourier and the amplitude of D. Hilbert. Bottom row right image is reconstructed by the phase of D. Hilbert and the amplitude of J. Fourier. It is interesting to observe that the phase information must be the dominant information in the spatial domain [55].

The main aim of this thesis is not the practical application of phase based approaches to image analysis problems, but to generalize the existing analytic and monogenic signals to a broader class of two dimensional and higher dimensional signal models, and to find a more natural algebraic embedding and its corresponding geometric interpretation in an appropriate space. This thesis is organized as follows, see also Figure (1.2): first we introduce the phase based low level signal analysis by the classical one dimensional analytic signal, and we will give an introduction to analytic functions. To solve two dimensional signal analysis problems we present the classification of signals by their intrinsic dimension. Based on this signal classification we will present different approaches for different signal models which belong to different signal classes. For the signal transformation we will use the generalized Hilbert transforms of order one up to order three. Therefore, we will give the explicit transforms in spatial domain and in Fourier domain. To understand the meaning of those transforms of any order we will present the very important relation of the Hilbert transform to the Radon transform. This relation offers

# 1. Introduction

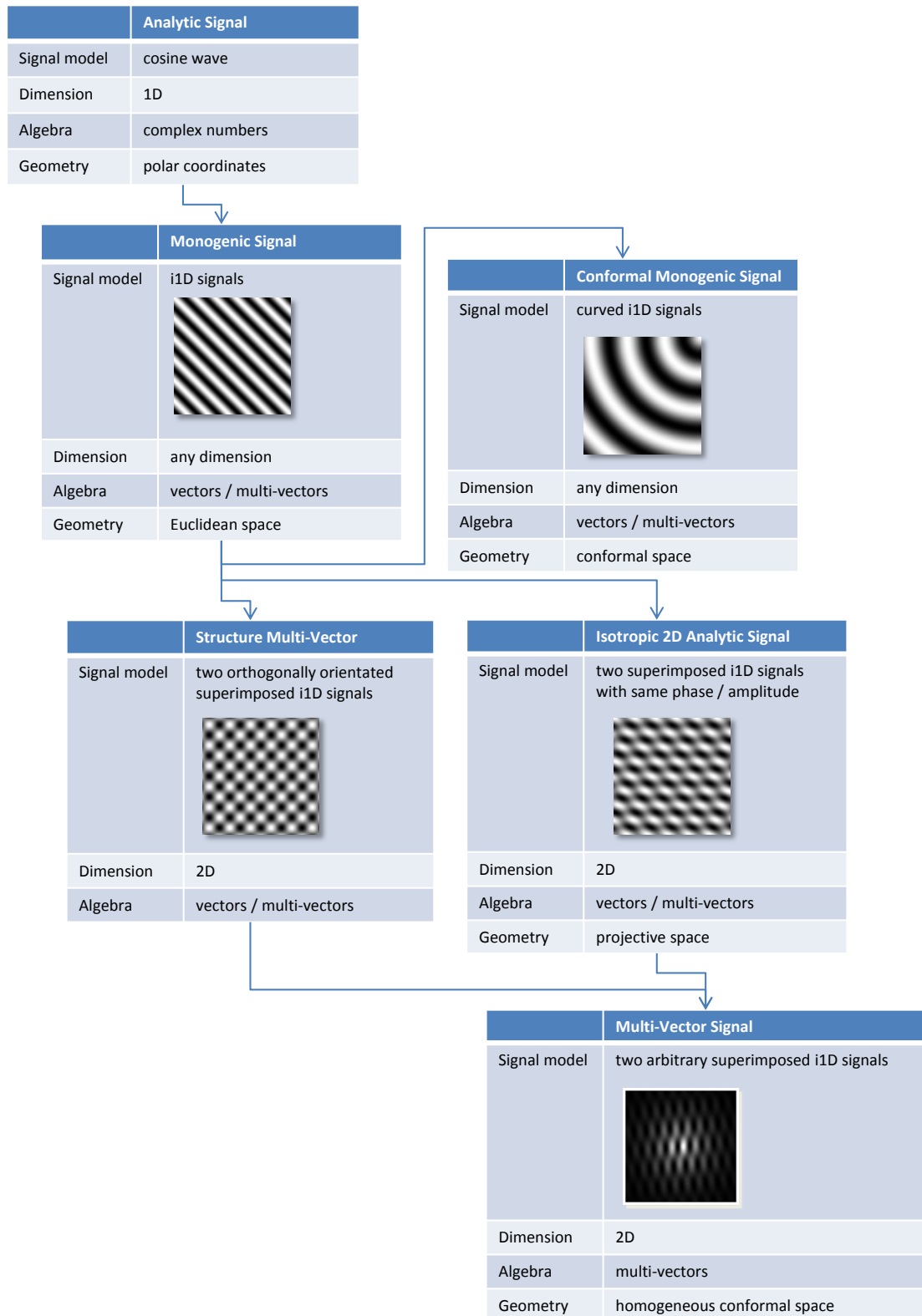


Figure 1.2.: Hierarchical and historical overview about isotropic low level and phased based analysis of Hilbert transformed signals which are being discussed in this thesis.



the direct geometric interpretation of the Hilbert transformed signals. As we already mentioned the Hilbert transform has to be applied to a signal in Poisson scale space. We will present the combination of the Poisson filter and the Hilbert transform up to order three. These filter kernels will be used by the subsequent low level phase based signal analysis approaches.

In chapter 2 the monogenic signals will be derived and the underlying signal model will be analyzed by the relation of the Radon transform to the first order generalized Hilbert transform. Furthermore, the limitations of the monogenic signal will be discussed and the generalization to the 2D analytic signal will be motivated. At the end of this chapter we will show the mathematical properties of monogenic functions and motivate possible applications of the property being monogenic in signal analysis.

Another generalization of the monogenic signal will be represented by its conformal extension in chapter 3. Same as the monogenic signal its conformal extension can be generalized to any dimension and it delivers additional curvature information without the need of any derivatives. Practical applications will be given for the 2D and 3D case in dense optical flow estimation.

The monogenic signal also introduced the class of intrinsic one dimensional signals as well as structural and geometric signal features. Motivated by the limitations of the monogenic signal we will introduce an extended version of a more general 2D signal model and the algebraic embedding of the higher order generalized Hilbert transforms. This approach will be called isotropic 2D analytic signal in chapter 4 and it represents a generalization of the monogenic signal for the case of superimposed intrinsic one dimensional signals. This includes a generalization of the signal model, the usage of higher order generalized Hilbert transforms, the generalization of the algebraic embedding of this structure and a more general geometric space to the Euclidean space which is the basic space of the monogenic signal. The 2D analytic signal is embedded in the projective space and shows the requirement of multi-vectors in the Euclidean vector space. Therefore, the geometric algebra and its corresponding hybrid matrix geometric algebra will be introduced. Since higher order generalized Hilbert transformed signals show a certain symmetry in matrix form, they can also be mapped to their corresponding multi-vector. The advantage of such a representation is its geometric interpretation. Practical applications are shown in the field of dense optical flow estimation and will be compared to existing methods.

In chapter 5 we present the generalization of the isotropic 2D analytic signal to the multi-vector signal for 2D signal domains. The multi-vector signal can be regarded as the generalization of the structure multi-vector [15] in appendix D. The main message of the multi-vector signal is the fact that the geometric product of the geometric algebra is a natural operation for complex geometric signal interpretation tasks. All approaches in this thesis correspond to a certain geometric space and its algebraic embedding as well as to the relation of the Radon transform to the generalized Hilbert transform. A complete overview about all different signal analysis approaches presented in this thesis is shown in Figure (1.2). We show the hierarchical order and the historical evolution of the approaches. Furthermore, the assumed signal models as well as the algebraic embedding and the geometric space of the signal interpretation is given. It can be seen, that

## 1. Introduction

the conformal monogenic signal represents a different stream compared to the isotropic 2D analytic signal followed by the multi-vector signal.

### 1.1. The Analytic Signal

To solve higher dimensional phase based signal analysis problems, first phase based one-dimensional signal analysis has to be considered. From Fourier analysis it is well known that each one-dimensional signal  $f \in L^2(\mathbb{R}, \mathbb{R}) \cap L^p(\mathbb{R}, \mathbb{R})$  with the  $L^p$  space

$$L^p(\Omega, \mathbb{R}) = \left\{ f : \Omega \mapsto \mathbb{R} : \int_{x \in \Omega} \|f(x)\|^p dx < \infty \right\} \quad (1.1)$$

can be approximated globally with infinite small error by

$$f(x) = \sum_{\nu=-\infty}^{\infty} a_{\nu} \cos(\nu x + \phi_{\nu}) \quad (1.2)$$

with  $\nu$  as the frequency, and  $a_0$  as the signal offset or DC-component. Each frequency component with its appropriated individual phase  $\phi_{\nu}$  and amplitude  $a_{\nu}$  can be analyzed separately. In this thesis signals are being analyzed locally at each position  $x \in \Omega$  in the spatial domain, i.e.

$$f(x) = \sum_{\nu=-\infty}^{\infty} a_{\nu}(x) \cos(\nu x + \phi_{\nu}(x)) . \quad (1.3)$$

The selected frequency component of interest carries the structural information of the original signal and has to be extracted by applying a filter operator to the original signal before the signal can be analyzed

$$\mathcal{P}_s\{f\}(x) = (p_s * f)(x) \quad (1.4)$$

with the one-dimensional Poisson convolution kernel [18]

$$p_s(x) = \frac{s}{\pi(x^2 + s^2)} , \quad (1.5)$$

where  $s > 0$  is the scale space parameter which corresponds to the local frequency. For  $s \rightarrow 0$  we obtain the Dirac delta distribution at position  $x$

$$\lim_{s \rightarrow 0} \frac{s}{\pi(x^2 + s^2)} = \delta_0(x) . \quad (1.6)$$

Therefore, the local one-dimensional signal model at the origin  $x = 0$  of the applied local coordinate system reads

$$f^e(x, s)|_{x=0} = a(x, s) \cos \phi(x, s)|_{x=0} = \mathcal{P}_s\{f\}(x)|_{x=0} \quad (1.7)$$

with  $s > 0$  as the scale space parameter of the Poisson filter operator  $\mathcal{P}_s\{\cdot\}$ . Since the local signal model is assumed to be an even function shifted by its phase parameter  $\phi(x, s)$ , i.e.

$$\cos(x) = \cos(-x) \quad \forall x \in \mathbb{R}, \quad (1.8)$$

it is called the even part  $f^e$  of the analytic signal  $f^a$ . The corresponding odd part

$$f^o(x, s) = a(x, s) \sin \phi(x, s) = (h * \mathcal{P}_s\{f\})(x) \quad (1.9)$$

can be calculated by means of convolution of the filtered original signal with the classical one-dimensional Hilbert transform kernel<sup>2</sup>

$$h(\tau) = \frac{1}{\pi\tau} \quad (1.10)$$

with  $*$  as the convolution operator in the spatial domain, and

$$(h * \mathcal{P}_s\{f\})(x) = \frac{1}{\pi} \text{P.V.} \int_{\tau \in \mathbb{R}} \frac{\mathcal{P}_s\{f\}(x - \tau)}{\tau} d\tau \quad (1.11)$$

as the classical one-dimensional Hilbert transform of the signal  $g$  in scale space, and P.V. as the Cauchy principal value. Since the Hilbert transform of the original signal is locally an odd function, i.e.

$$\sin(x) = -\sin(-x) \quad \forall x \in \mathbb{R}, \quad (1.12)$$

it is called the odd part  $f^o$  of the analytic signal  $f^a$ .

One important local structural feature of the filtered signal  $\mathcal{P}_s\{f\}$  is the local phase  $\phi(x, s) \in [0, 2\pi)$  [36] because it is independent of the local signal amplitude  $a(x, s) \in \mathbb{R}$  [28]. The local phase can be determined by

$$\phi(x, s) = \arctan \frac{f^o(x, s)}{f^e(x, s)} = \arctan \frac{\sin \phi(x, s)}{\cos \phi(x, s)} \quad (1.13)$$

and the local signal amplitude can be determined by

$$a(x, s) = \sqrt{(f^e(x, s))^2 + (f^o(x, s))^2} = a(x, s) \sqrt{\cos^2 \phi(x, s) + \sin^2 \phi(x, s)}. \quad (1.14)$$

The vector valued extension

$$f^a(x, s) = \begin{bmatrix} f^e(x, s) \\ f^o(x, s) \end{bmatrix} \quad (1.15)$$

---

<sup>2</sup>Note that  $c_a \exp(\mathbf{i}\nu x) = c_a (\cos(\nu x) + \mathbf{i} \sin(\nu x))$  with  $c_a \in \mathbb{C}$  as the eigenfunction value of the Hilbert transform, which does not change its absolute value  $\|c_a\|$  but only changes its argument by  $90^\circ$ , and determines the relation of the signal transform and its appropriated signal model, i.e. the signal model used in this thesis is not arbitrarily chosen. If one chooses another signal model, its corresponding transform has to be found also.

## 1. Introduction

of a scalar valued one-dimensional signal  $f$  is called analytic signal  $f^a$ , see Figure (1.3). Note that originally the analytic signal has been defined as a complex valued signal with  $f^e$  as the real part and  $f^o$  as the imaginary part [26]

$$f_A(x, s) = f^e(x, s) + \mathbf{i}f^o(x, s) \in \mathbb{C}, \quad (1.16)$$

where the local phase is the argument of the complex number  $\arg f_A$  and the amplitude is defined by its absolute value  $\|f_A\|$ .

### 1.1.1. Analytic Functions

The analytic signal can also be derived by the construction of a function fulfilling the Dirac equations, i.e. a holomorphic or monogenic function, whose real part is the real-valued original signal on the boundary. It appears that it is equivalent to find the solution  $f_A$  of a boundary value problem of the second kind, that is a von Neumann problem:

$$\begin{cases} \Delta f_A = \frac{\partial^2}{\partial x^2} f_A + \frac{\partial^2}{\partial s^2} f_A = 0, & s > 0, \\ \frac{\partial}{\partial s} f_A = f(x), & s = 0. \end{cases} \quad (1.17)$$

with

$$D = \mathbf{e}_1 \frac{\partial}{\partial x} + \mathbf{e}_2 \frac{\partial}{\partial s}, \quad (1.18)$$

$\Delta = D^2$  and  $\mathbf{e}_\nu$  as the basis vectors of the Euclidean space. The first Equation (1.17) is the 2D-Laplace equation restricted to the open domain  $s > 0$ . The second equation is called the boundary condition. Using the fundamental solution of the 2D-Laplace equation, the solution of the boundary problem is the complex valued analytic signal  $f_A : \mathbb{R} \times \mathbb{R}_+ \mapsto \mathbb{C}$

$$f_A(x, s) = \mathcal{P}_s\{f\}(x) + \mathbf{i}(h * \mathcal{P}_s\{f\})(x). \quad (1.19)$$

The one-dimensional analytic signal has also been used in higher dimensional signal processing. This makes it necessary to extend the classical one-dimensional Hilbert transform to multiple dimensions. There are several approaches in the literature which lack the required rotational invariance of the multidimensional Hilbert transform, refer to [31, 9].

One possible generalization of the one-dimensional Hilbert transform to higher dimensions is the Riesz transform [56] which will be called generalized Hilbert transform in this thesis.

## 1.2. 2D Signal Classification

Two-dimensional signals are functions  $f$  in the sense of distributions with compact support which will be classified into local regions  $N \subseteq \Omega$  of different intrinsic dimensions [78]. The intrinsic dimension expresses the number of degrees of freedom necessary to describe local structure. Constant signals are of intrinsic dimension zero (i0D), lines and

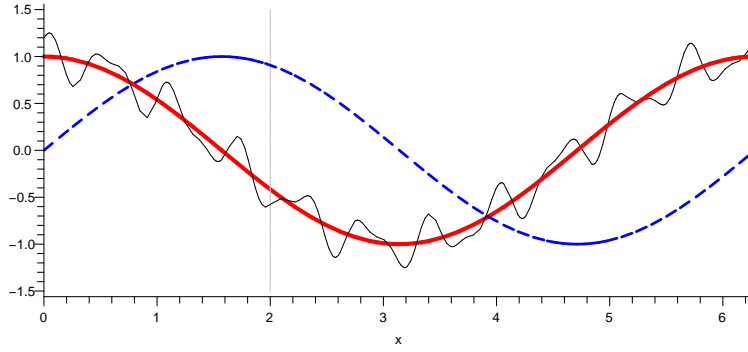


Figure 1.3.: Illustration of a one-dimensional signal with its even signal part  $f^e$  (red line) and odd signal part  $f^o$  (blue dashed line) in scale space (for the frequency  $\nu = 1\text{Hz}$ ) with local amplitude  $a(x, s) = 1$  and local phase  $\phi(2, s) = 2$  at the test point  $x = 2$ .

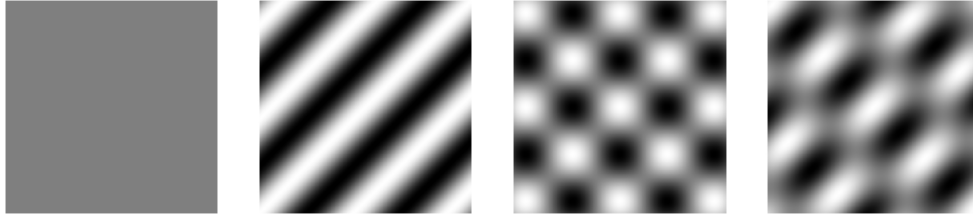


Figure 1.4.: From left to right: A constant signal (i0D), an arbitrarily rotated 1D signal (i1D) and two i2D signals which consist of two superposed i1D signals. Note that all signals displayed here preserve their intrinsic dimension globally.

edges are of intrinsic dimension one (i1D), and all other possible patterns are of intrinsic dimension two (i2D), see Figure (1.4),

$$\text{i0D} = \{f \mid f(z_\nu) = f(z_\mu) \forall z_\nu, z_\mu \in N\}, \quad (1.20)$$

$$\text{i1D} = \left\{f \mid f(z) = g\left(\left\langle z, \begin{bmatrix} \cos \theta \\ \sin \theta \end{bmatrix} \right\rangle\right) \forall z \in N\right\} \setminus \text{i0D}, \quad (1.21)$$

$$\text{i2D} = \{f \mid \exists z_\nu, z_\mu \in N : f(z_\nu) \neq f(z_\mu)\} \setminus \text{i1D} \quad (1.22)$$

with  $g$  as a one-dimensional function with compact support. In general i2D signals can be modeled by an arbitrary number of superimposed i1D signals. Therefore, it is essential to assume a certain signal model or a set of certain models for exact i2D signal analysis. Furthermore, the intrinsic dimension also depends on the scale at which the signal will be considered locally. From a statistical point of view, the frequency of occurrence of local regions with different intrinsic dimension in real images appears in the following upward order: i0D, i1D and i2D.

### 1.3. Higher Order Generalized Hilbert Transforms

Many low-level signal analysis approaches such as the SIFT features are based on partial derivatives and higher order derivatives. In this thesis we will substitute those derivatives by their analogous components of the generalized Hilbert transforms.

The  $m$ -dimensional Fourier transform  $\mathcal{F}_m\{\cdot\}$  of a function  $f \in L^2(\mathbb{R}^m, \mathbb{R})$  reads

$$\mathcal{F}_m\{f\}(u) = \hat{f}(u) = \frac{1}{(2\pi)^{\frac{m}{2}}} \int_{x \in \mathbb{R}^m} e^{i\langle u, x \rangle} f(x) dx \quad (1.23)$$

with  $u \in \mathbb{R}^m$ , the Euler's formula [46]

$$e^{i\alpha} = \cos \alpha + \mathbf{i} \sin \alpha \in \mathbb{C}, \quad (1.24)$$

and the inverse Fourier transform  $\mathcal{F}_m^{-1}\{\cdot\}$  reads

$$\mathcal{F}_m^{-1}\{\hat{f}\}(x) = f(x) = \frac{1}{(2\pi)^{\frac{m}{2}}} \int_{u \in \mathbb{R}^m} e^{-i\langle u, x \rangle} \hat{f}(u) du. \quad (1.25)$$

In Fourier space  $\mathcal{F}\{\cdot\}(u)$  [38] it can be seen clearly that the derivative operator of order  $n$ ,  $\mathcal{D}^{(n)}$ ,

$$\mathcal{F}_m\{\mathcal{D}^{(n)}\{f\}\}(u) = (2\pi u \mathbf{i})^n \hat{f}(u) \quad \text{with } u \in \mathbb{R}_m \quad (1.26)$$

is closely related to the generalized Hilbert transform operator of order  $n$ ,  $\mathcal{H}^{(n)}$ ,

$$\mathcal{F}_m\{\mathcal{H}^{(n)}\{f\}\}(u) = (2\pi \bar{u} \mathbf{i})^n \hat{f}(u) \quad \text{with } \bar{u} = \frac{u}{\|u\|}, u \in \mathbb{R}_m, \quad (1.27)$$

which are only well defined in  $\mathbb{R}_m$  [7]. Phase based [10] one-dimensional signal analysis will be done by the analytic signal and the classical one-dimensional Hilbert transform [26]. Analysis of higher dimensional signals can be done by the generalized Hilbert transform [7] which will be abbreviated by Hilbert transform. To enable local signal analysis in scale space with individual scale space parameters at every test point within the signal, it is essential that the Hilbert transform of arbitrary order can be done by convolution in the spatial domain and without the need of Fourier transformation.

Instead of writing the spatial domain coordinates in vector form  $(x, y) \in \mathbb{R}^2$ , they will now be expressed as complex numbers  $z \in \mathbb{C}$  with  $z = x + \mathbf{i}y$ . According to [35] for  $\xi = \xi_1 + \mathbf{i}\xi_2 \in \mathbb{C}$  and the two-dimensional signal  $f \in L^2(\mathbb{C}, \mathbb{R})$ , the Hilbert transform of order  $n \in \mathbb{N}$

$$\mathcal{H}^{(n)}\{f\}(z) = \underbrace{\mathcal{H}^{(1)}\{\mathcal{H}^{(1)}\{\dots\mathcal{H}^{(1)}\{f\}\}\}}_{n\text{-times concatenation}}(z) \quad (1.28)$$

which is a self-adjoint operator is related to the higher order Beurling-Ahlfors transform

$$-\frac{n}{2\pi} \int_{\xi \in \mathbb{C}} \frac{f(\xi)}{(z - \xi)^n \|z - \xi\|^{2-n}} d\xi. \quad (1.29)$$

Note, that we will write  $\mathcal{H}_{x^i y^j}^{(n)}$  for each real valued component of the  $n = i + j$  order Hilbert transform.

### 1.3.1. First Order Hilbert Transform

For  $n = 1$  the ordinary first order Hilbert transform in two dimensions is obtained as

$$\begin{aligned}
 \mathcal{H}^{(1)}\{f\}(z) &= -\frac{1}{2\pi} \int_{\xi \in \mathbb{C}} \frac{f(\xi)}{(z - \xi)\|z - \xi\|} d\xi \\
 &= -\frac{1}{2\pi} \int_{\xi \in \mathbb{C}} \frac{(x - \xi_1)}{\|z - \xi\|^3} f(\xi) d\xi + \mathbf{i} \frac{1}{2\pi} \int_{\xi \in \mathbb{C}} \frac{(y - \xi_2)}{\|z - \xi\|^3} f(\xi) d\xi \\
 &= -\mathcal{H}_x^{(1)}\{f\}(z) + \mathbf{i}\mathcal{H}_y^{(1)}\{f\}(z). \tag{1.30}
 \end{aligned}$$

This results in the following convolution kernels of the first order Hilbert transform

$$h^{(1)}(x, y) = \begin{bmatrix} h_x^{(1)} \\ h_y^{(1)} \end{bmatrix} (x, y) = \frac{1}{2\pi(x^2 + y^2)^{\frac{3}{2}}} \begin{bmatrix} x \\ y \end{bmatrix}. \tag{1.31}$$

These kernels can be directly used to calculate the first order Hilbert transform of a two-dimensional signal  $f \in L^2(\mathbb{R}^2, \mathbb{R})$  in the spatial domain without the need of any Fourier transform.

### 1.3.2. Second Order Hilbert Transform

The convolution kernel in the spatial domain of the second order Hilbert transform for ( $n = 2$ ) results in the Beurling-Ahlfors transform for the signal  $f \in L^2(\mathbb{C}, \mathbb{R})$ , which is without loss of generality defined on the complex numbers, and reads

$$\begin{aligned}
 \mathcal{H}^{(2)}\{f\}(z) &= -\frac{1}{\pi} \int_{\xi \in \mathbb{C}} \frac{f(\xi)}{(z - \xi)^2} d\xi \\
 &= -\frac{1}{\pi} \int_{\xi \in \mathbb{C}} \frac{(x - \xi_1)^2 f(\xi)}{[(x - \xi_1)^2 - (y - \xi_2)]^2 + 4(x - \xi_1)^2(y - \xi_2)^2} d\xi \\
 &\quad + \frac{1}{\pi} \int_{\xi \in \mathbb{C}} \frac{(y - \xi_2)^2 f(\xi)}{[(x - \xi_1)^2 - (y - \xi_2)]^2 + 4(x - \xi_1)^2(y - \xi_2)^2} d\xi \\
 &\quad + \mathbf{i} \frac{2}{\pi} \int_{\xi \in \mathbb{C}} \frac{(x - \xi_1)(y - \xi_2) f(\xi)}{[(x - \xi_1)^2 - (y - \xi_2)]^2 + 4(x - \xi_1)^2(y - \xi_2)^2} d\xi \\
 &= -(\mathcal{H}_{xx}^{(2)}\{f\}(z) - \mathcal{H}_{yy}^{(2)}\{f\}(z)) + \mathbf{i}2\mathcal{H}_{xy}^{(2)}\{f\}(z). \tag{1.32}
 \end{aligned}$$

This results in the following convolution kernels of the second order Hilbert transform

$$h^{(2)}(x, y) = \begin{bmatrix} h_{xx}^{(2)} \\ h_{xy}^{(2)} \\ h_{yy}^{(2)} \end{bmatrix} (x, y) = \frac{1}{\pi(x^2 + y^2)^2} \begin{bmatrix} x^2 \\ xy \\ y^2 \end{bmatrix}. \tag{1.33}$$

### 1.3.3. Relation of Hilbert Transforms to Radon Transform

The Hilbert transform can be expressed using the Radon transform, its inverse and the classical one-dimensional Hilbert transform [73, 74]. Note that the relation of the Hilbert transform to the Radon transform is solely required for signal interpretation and theoretical results. Neither the Radon transform nor its inverse are ever applied to the signal in practice, see Figure (1.5). Instead, the Hilbert transformed signal will be determined by convolution with the Hilbert kernels in the spatial domain. The two-dimensional Radon transform  $f_r(t, \theta) = \mathcal{R}\{f\}(t, \theta)$  [5] is defined by

$$\mathcal{R}\{f\}(t, \theta) = \int_{(x,y) \in \mathbb{R}^2} f(x, y) \delta_0(x \cos \theta + y \sin \theta - t) d(x, y) \quad (1.34)$$

with  $\theta \in [0, \pi)$  as the orientation,  $t \in \mathbb{R}$  as the minimal distance of the integral line to the origin of the local coordinate system, and  $\delta_0$  as the Dirac delta distribution at position 0. The most important properties of the Radon transform for  $\alpha, \beta \in \mathbb{R}$ ,  $z = (x, y) \in \mathbb{R}^2$  and the rotation matrix

$$R_\beta = \begin{bmatrix} \cos \beta & -\sin \beta \\ \sin \beta & \cos \beta \end{bmatrix} \quad (1.35)$$

are:

1. Linearity of the Radon transform:

$$\mathcal{R}\{\alpha f + \beta g\} = \alpha \mathcal{R}\{f\} + \beta \mathcal{R}\{g\} \quad (1.36)$$

2. Rotation by an angle  $\beta \in [0, 2\pi)$  and its resulting rotation matrix  $R_\beta$ :

$$\mathcal{R}\{f(z R_\beta)\}(t, \theta) = \mathcal{R}\{f\}(t, \theta + \beta) \quad (1.37)$$

3. Scaling by  $\alpha, \beta \in \mathbb{R}$ :

$$\mathcal{R}\left\{f\left(\frac{1}{\alpha}x, \frac{1}{\beta}y\right)\right\}(t, \theta) = \frac{\alpha\beta}{\gamma} \mathcal{R}\{f\}\left(\gamma^{-1}, \arctan\left(\frac{\beta}{\alpha} \tan \theta\right)\right) \quad (1.38)$$

$$\text{with } \gamma = \sqrt{\alpha^2 \cos^2 \theta + \beta^2 \sin^2 \theta}$$

The inverse 2D Radon transform  $\mathcal{R}^{-1}\{(t, \theta) \mapsto f_r\}(x, y)$  exists and is defined by

$$\mathcal{R}^{-1}\{f_r\}(x, y) = \frac{1}{2\pi^2} \int_{\theta \in [0, \pi)} \text{P.V.} \int_{t \in \mathbb{R}} \frac{\frac{\partial}{\partial t} f_r(t, \theta)}{x \cos \theta + y \sin \theta - t} dt d\theta. \quad (1.39)$$

Now the Hilbert transform will be expressed by the classical one-dimensional Hilbert transform, the Radon transform and its inverse



**Theorem 1.3.1.**

$$\mathcal{H}^{(1)}\{f\}(x, y) = \mathcal{R}^{-1} \left\{ (t, \theta) \mapsto \left[ \begin{array}{c} \cos \theta \\ \sin \theta \end{array} \right] \underbrace{(h * f_r(\cdot, \theta))(t)}_{\mathcal{H}\{f_r\}(t; \theta)} \right\} (x, y) \quad (1.40)$$

with

$$\mathcal{H}\{f_r\}(t; \theta) = \frac{1}{\pi} \text{P.V.} \int_{\tau \in \mathbb{R}} \frac{f_r(\tau - t, \theta)}{\tau} d\tau \quad (1.41)$$

as the classical one-dimensional Hilbert transform in Radon space. In other words, the Hilbert transform applies a one-dimensional Hilbert transform to the Radon space representation  $f_r(t; \theta)$  of the original signal along the parameter  $t \in \mathbb{R}$  for each orientation angle  $\theta \in [0, \pi)$  separately.

*Proof:* Like in [16] we will show that the first order Hilbert transform can be written in terms of the Radon transform  $\mathcal{R}\{\cdot\}$ , its inverse  $\mathcal{R}^{-1}\{(t, \theta) \mapsto f_r\}$  and the classical one-dimensional Hilbert transform. The proof will be shown in Fourier domain by means of the Fourier slice theorem (FST). The one-dimensional Hilbert transform can be written in Fourier space as

$$\hat{h}(u) = \mathcal{F}_1\{h\}(u) = \mathbf{i} \text{sign}(u), \quad u \in \mathbb{R} \quad (1.42)$$

with

$$\text{sign}(u) = \begin{cases} 1, & u > 0, \\ -1, & u < 0, \\ 0, & u = 0. \end{cases} \quad (1.43)$$

which can also be written in terms of  $\frac{u}{\|u\|} = \text{sign}(u)$  for  $u \in \mathbb{R} \setminus \{0\}$  and  $\mathbf{i}$  as the imaginary unit of the complex numbers  $(\mathbb{C}, +, \cdot)$ . The two-dimensional Hilbert transform kernel can be represented in Fourier space by

$$\hat{h}^{(1)}(u) = \mathcal{F}_2\{h^{(1)}\}(u) = \mathbf{i} \frac{u}{\|u\|}, \quad u \in \mathbb{R}^2 \setminus \{(0, 0)\} \quad (1.44)$$

and is written as components in  $x$  and  $y$  direction

$$\hat{h}_x^{(1)}(u n_\theta) = \mathcal{F}_2\{h_x^{(1)}\}(u n_\theta) = \mathbf{i} \frac{u \cos \theta}{\|u\|}, \quad u \in \mathbb{R} \setminus \{0\} \quad (1.45)$$

and

$$\hat{h}_y^{(1)}(u n_\theta) = \mathcal{F}_2\{h_y^{(1)}\}(u n_\theta) = \mathbf{i} \frac{u \sin \theta}{\|u\|}, \quad u \in \mathbb{R} \setminus \{0\}. \quad (1.46)$$

By means of the Fourier slice theorem

$$\mathcal{F}_1\{\mathcal{R}\{\cdot\}\}(u, \theta) = \mathcal{F}_2\{\cdot\}(u n_\theta) = \mathcal{F}_2\{\cdot\}(u \cos \theta, u \sin \theta) \quad (1.47)$$

## 1. Introduction

with  $u \in \mathbb{R}$ ,  $\mathcal{F}_1 \{ \cdot \} (u, \theta) \in \mathbb{C}$  as the one-dimensional partial Fourier transform of a two-dimensional signal in direction of  $\theta \in [0, 2\pi)$  and  $n_\theta = [\cos \theta, \sin \theta]^T$ , it will be shown that the Hilbert transform can be written in terms of the Radon transform as

$$\begin{aligned}
\mathcal{F}_1 \{ \mathcal{R} \{ \mathcal{H}^{(1)} \{ f \} \} \} (u, \theta) &= \begin{bmatrix} \mathcal{F}_1 \left\{ \mathcal{R} \left\{ \mathcal{H}_x^{(1)} \{ f \} \right\} \right\} (u, \theta) \\ \mathcal{F}_1 \left\{ \mathcal{R} \left\{ \mathcal{H}_y^{(1)} \{ f \} \right\} \right\} (u, \theta) \end{bmatrix} \\
&\stackrel{FST}{=} \begin{bmatrix} \mathcal{F}_2 \left\{ \mathcal{H}_x^{(1)} \{ f \} \right\} (u n_\theta) \\ \mathcal{F}_2 \left\{ \mathcal{H}_y^{(1)} \{ f \} \right\} (u n_\theta) \end{bmatrix} \\
&= \mathcal{F}_2 \{ f \} (u n_\theta) \begin{bmatrix} \hat{h}_x^{(1)}(u n_\theta) \\ \hat{h}_y^{(1)}(u n_\theta) \end{bmatrix} \\
&= \mathcal{F}_2 \{ f \} (u n_\theta) \begin{bmatrix} \mathbf{i} \frac{u \cos \theta}{\|u\|} \\ \mathbf{i} \frac{u \sin \theta}{\|u\|} \end{bmatrix} \\
&= \mathbf{i} \operatorname{sign}(u) \mathcal{F}_2 \{ f \} (u n_\theta) \begin{bmatrix} \cos \theta \\ \sin \theta \end{bmatrix} \\
&= \mathcal{F}_1 \{ h \} (u) \underbrace{\mathcal{F}_2 \{ f \} (u n_\theta)}_{\stackrel{FST}{=} \mathcal{F}_1 \{ \mathcal{R} \{ f \} \} (u, \theta)} \begin{bmatrix} \cos \theta \\ \sin \theta \end{bmatrix} \\
&= \mathcal{F}_1 \{ h \} (u) \mathcal{F}_1 \{ \mathcal{R} \{ f \} \} (u, \theta) \begin{bmatrix} \cos \theta \\ \sin \theta \end{bmatrix}. \tag{1.48}
\end{aligned}$$

Because of the existence of the inverse Radon transform  $\mathcal{R}^{-1} \{ (t, \theta) \mapsto f_r \}$ , now the relation of the Radon transform to the Hilbert transform follows

$$\mathcal{F}_1 \{ \mathcal{R} \{ \mathcal{H}^{(1)} \{ f \} \} \} (u, \theta) = \mathcal{F}_1 \{ h \} (u) \mathcal{F}_1 \{ \mathcal{R} \{ f \} \} (u, \theta) \begin{bmatrix} \cos \theta \\ \sin \theta \end{bmatrix} \tag{1.49}$$

$$\begin{aligned}
\Rightarrow \mathcal{R} \{ \mathcal{H}^{(1)} \{ f \} \} (t, \theta) &= (h * \mathcal{R} \{ f \} (\cdot, \theta))(t) \begin{bmatrix} \cos \theta \\ \sin \theta \end{bmatrix} \\
\Rightarrow \mathcal{H}^{(1)} \{ f \} (x, y) &= \mathcal{R}^{-1} \left\{ (t, \theta) \mapsto (h * \mathcal{R} \{ f \} (\cdot, \theta))(t) \begin{bmatrix} \cos \theta \\ \sin \theta \end{bmatrix} \right\} (x, y) \tag{1.50}
\end{aligned}$$

□

Please note that because of the important property  $\mathcal{R} \{ \mathcal{R}^{-1} \{ f_r \} \} = f_r$ , the  $n$ -th order Hilbert transform  $\mathcal{H}^{(n)} \{ f \}$  of a signal can easily be written as the concatenation of a number of  $n$  first order Hilbert transforms expressed in Radon space. This fact is very important for the higher order Hilbert transforms such as the second order Hilbert transform

$$\mathcal{H}^{(2)} \{ f \} (x, y) = \mathcal{H}^{(1)} \{ \mathcal{H}^{(1)} \{ f \} \} (x, y) \tag{1.51}$$

and the third order Hilbert transform

$$\mathcal{H}^{(3)} \{ f \} (x, y) = \mathcal{H}^{(1)} \{ \mathcal{H}^{(1)} \{ \mathcal{H}^{(1)} \{ f \} \} \} (x, y) \tag{1.52}$$

which will be intensively used in this thesis.

In case of the second order Hilbert transform the concatenation of the two first order Hilbert transforms can be done componentwise. This will now be demonstrated exemplarily with the  $\mathcal{H}_{xx}^{(2)}(x, y)$  component of the second order Hilbert transform. By definition

$$\mathcal{H}_x^{(1)}\{f\}(x, y) = \mathcal{R}^{-1} \left\{ (t, \theta) \mapsto \cos \theta (h * \mathcal{R}\{f\}(\cdot, \theta))(t) \right\} (x, y) \quad (1.53)$$

the second order Hilbert transform can be expressed as a concatenation

$$\begin{aligned} \mathcal{H}_{xx}^{(2)}\{f\}(x, y) &= \mathcal{H}_x^{(1)}\{\mathcal{H}_x^{(1)}\{f\}\}(x, y) \\ &= \mathcal{R}^{-1} \left\{ (t, \theta) \mapsto \cos \theta (h * \mathcal{R}\{\mathcal{R}^{-1} \{ \cos \theta (h * \mathcal{R}\{f\}(\cdot, \theta))(t) \}(\cdot, \theta)(t)) \right\} (x, y) \\ &= \mathcal{R}^{-1} \left\{ (t, \theta) \mapsto \cos \theta (h * [\cos \theta (h * \mathcal{R}\{f\}(\cdot, \theta))(t]) (\cdot, \theta)(t)) \right\} (x, y) \\ &= \mathcal{R}^{-1} \left\{ (t, \theta) \mapsto \cos^2 \theta ((h * h) * \mathcal{R}\{f\}(\cdot, \theta))(t) \right\} (x, y) \\ &= -\mathcal{R}^{-1} \left\{ (t, \theta) \mapsto \cos^2 \theta \mathcal{R}\{f\}(t, \theta) \right\} (x, y) . \end{aligned} \quad (1.54)$$

This can be done analogously for all other components of the second order Hilbert transform

$$\mathcal{H}_{xx}^{(2)}\{f\}(x, y) = -\mathcal{R}^{-1} \left\{ (t, \theta) \mapsto \cos^2 \theta f_r(t; \theta) \right\} (x, y) , \quad (1.55)$$

$$\mathcal{H}_{xy}^{(2)}\{f\}(x, y) = -\mathcal{R}^{-1} \left\{ (t, \theta) \mapsto \cos \theta \sin \theta f_r(t; \theta) \right\} (x, y) , \quad (1.56)$$

$$\mathcal{H}_{yy}^{(2)}\{f\}(x, y) = -\mathcal{R}^{-1} \left\{ (t, \theta) \mapsto \sin^2 \theta f_r(t; \theta) \right\} (x, y) \quad (1.57)$$

with  $f_r(t; \theta) = \mathcal{R}\{f\}(t; \theta)$ .

The third order Hilbert transform can be expressed as a concatenation of three first order Hilbert transforms

$$\mathcal{H}_{xxx}^{(3)}\{f\}(x, y) = -\mathcal{R}^{-1} \left\{ (t, \theta) \mapsto \cos^3 \theta (h * f_r(\cdot, \theta))(t) \right\} (x, y) , \quad (1.58)$$

$$\mathcal{H}_{xxy}^{(3)}\{f\}(x, y) = -\mathcal{R}^{-1} \left\{ (t, \theta) \mapsto \cos^2 \theta \sin \theta (h * f_r(\cdot, \theta))(t) \right\} (x, y) , \quad (1.59)$$

$$\mathcal{H}_{xyy}^{(3)}\{f\}(x, y) = -\mathcal{R}^{-1} \left\{ (t, \theta) \mapsto \cos \theta \sin^2 \theta (h * f_r(\cdot, \theta))(t) \right\} (x, y) , \quad (1.60)$$

$$\mathcal{H}_{yyy}^{(3)}\{f\}(x, y) = -\mathcal{R}^{-1} \left\{ (t, \theta) \mapsto \sin^3 \theta (h * f_r(\cdot, \theta))(t) \right\} (x, y) \quad (1.61)$$

since  $(h * h * h)(t) = -h(t)$ .

#### 1.3.4. The Partial Hilbert Transform

The partial two-dimensional function in direction  $\theta$  at the origin of the applied local coordinate system reads

$$f_\theta(\tau) = f(\tau \cos \theta, \tau \sin \theta) . \quad (1.62)$$

The classical one-dimensional Hilbert transform

$$(h * g)(t) = -\frac{1}{\pi} \text{P.V.} \int_{\tau \in \mathbb{R}} \frac{g(\tau + t)}{\tau} d\tau \quad (1.63)$$

## 1. Introduction

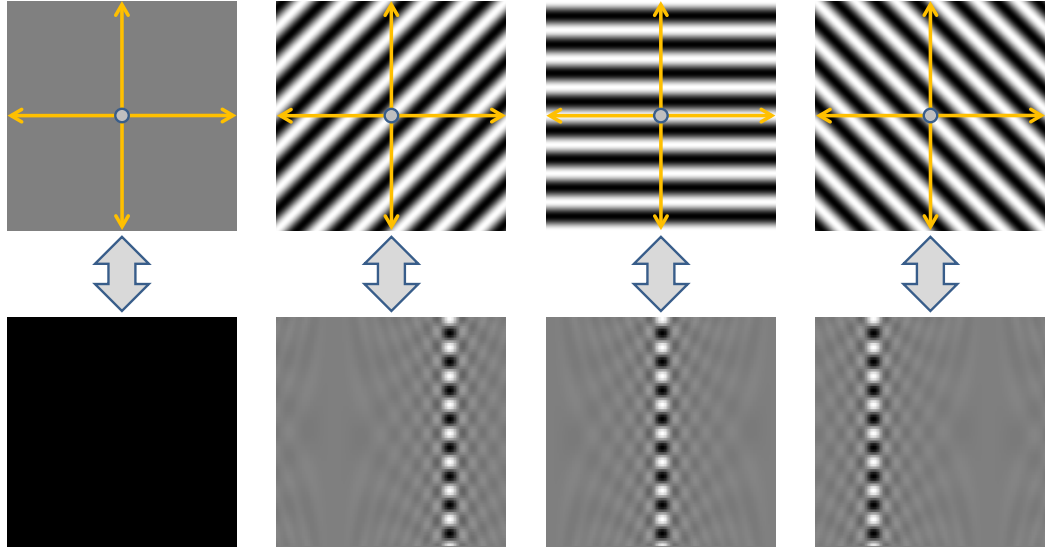


Figure 1.5.: One i0D signal and three i1D signals with orientation  $45^\circ$ ,  $90^\circ$  and  $135^\circ$  in the spatial domain (first row) and in the corresponding Radon space (second row).

is defined for one-dimensional signals  $g \in L^2(\mathbb{R}, \mathbb{R})$ , and therefore can also be done in any direction  $\theta \in [0, 2\pi)$  within the i1D signal by the so called partial Hilbert transform [31]

$$(h * f_\theta)(t) = -\frac{1}{\pi} \text{P.V.} \int_{\tau \in \mathbb{R}} \frac{1}{\tau} f((\tau + t) \cos \theta, (\tau + t) \sin \theta) d\tau . \quad (1.64)$$

In case the main orientation of the i1D signal is unknown, the partial Hilbert transform has to be done in all possible directions. Of course, exact approaches must not try out all of these directions. This problem can be solved by the generalized Hilbert transform. Now it will be shown, that the generalized Hilbert transform contains the partial one-dimensional Hilbert transform as a special case

### Theorem 1.3.2.

$$\mathcal{R}^{-1} \{(t, \theta) \mapsto (h * f_r(\cdot, \theta))(t)\} (x, y)|_{(x,y)=(0,0)} = (h * f_\theta)(t)|_{t=0} . \quad (1.65)$$

*Proof:* Without loss of generality this will be shown for the class of i1D signals at the origin of the local coordinate system. With the inverse two-dimensional Radon transform  $\mathcal{R}^{-1} \{(t, \theta) \mapsto f_r\}$  the relation of the partial Hilbert transform to the generalized Hilbert

transform can be shown by

$$\begin{aligned}
 & \mathcal{R}^{-1} \left\{ (t, \theta) \mapsto (h * f_r(\cdot, \theta))(t) \right\} (x, y) \Big|_{(x,y)=(0,0)} \\
 &= \mathcal{R}^{-1} \left\{ (t, \theta) \mapsto \frac{1}{\pi} \text{P.V.} \int_{\tau \in \mathbb{R}} \frac{f_r(\tau + t; \theta)}{-\tau} d\tau \right\} (x, y) \Big|_{(x,y)=(0,0)} \\
 &= \frac{1}{2\pi^2} \int_{\theta \in [0, \pi)} \text{P.V.} \int_{t \in \mathbb{R}} \frac{\frac{\partial}{\partial t} \left[ \frac{1}{\pi} \text{P.V.} \int_{\tau \in \mathbb{R}} \frac{f_r(\tau + t; \theta)}{-\tau} d\tau \right]}{x \cos \theta + y \sin \theta - t} dt d\theta \Big|_{(x,y)=(0,0)} \\
 &= \frac{1}{q} 2\pi^3 \int_{\theta \in [0, \pi)} \text{P.V.} \int_{t \in \mathbb{R}} \frac{1}{-t} \left[ \frac{\partial}{\partial t} \text{P.V.} \int_{\tau \in \mathbb{R}} \frac{f_r(\tau + t; \theta)}{-\tau} d\tau \right] dt d\theta \\
 &= \frac{1}{\pi} \text{P.V.} \int_{\tau \in \mathbb{R}} \frac{1}{-\tau} \left[ \frac{1}{2\pi^2} \int_{\theta \in [0, \pi)} \text{P.V.} \int_{t \in \mathbb{R}} \frac{1}{-t} \frac{\partial}{\partial t} f_r(\tau + t; \theta) dt d\theta \right] d\tau \\
 &= \frac{1}{\pi} \text{P.V.} \int_{\tau \in \mathbb{R}} \frac{1}{-\tau} \underbrace{\left[ \frac{1}{2\pi^2} \int_{\theta \in [0, \pi)} \text{P.V.} \int_{t \in \mathbb{R}} \frac{\frac{\partial}{\partial t} f_r(\tau + t; \theta)}{(0 \cos \theta + 0 \sin \theta) - t} dt d\theta \right]}_{=g(\tau)} d\tau \\
 &= \frac{1}{\pi} \text{P.V.} \int_{\tau \in \mathbb{R}} \frac{g(\tau + t)}{-\tau} d\tau \Big|_{t=0} \\
 &= (h * g)(t) \Big|_{t=0} \\
 &= (h * \mathcal{R}^{-1} \{ (t, \theta) \mapsto f_r(\cdot, \theta) \})(t) \Big|_{t=0} \\
 &= -\frac{1}{\pi} \text{P.V.} \int_{\tau \in \mathbb{R}} \frac{f(\tau \cos \theta, \tau \sin \theta)}{\tau} d\tau \\
 &= (h * f_\theta)(t) \Big|_{t=0} \tag{1.66}
 \end{aligned}$$

□

This reveals that, although the generalized Hilbert transform is one possible generalization of the one-dimensional Hilbert transform to multi-dimensional signal domains, it still applies a one-dimensional Hilbert transform along every orientation, and therefore also along the main orientation  $\theta$  of an i1D signal to the original two-dimensional signal.

## 1.4. The Poisson Scale Space

Since all signals  $f \in L^2(\Omega, \mathbb{R})$  with  $\Omega \subseteq \mathbb{R}^2$  can be decomposed into their corresponding Fourier series [6], for each frequency a certain amplitude and phase can be obtained.

## 1. Introduction

Therefore, the local frequency of interest must be filtered out locally of the original signal. The frequency corresponds to the so called scale space parameter  $s > 0$ . The representation of a signal  $f$  in Poisson scale space [18] can be computed by convolution  $*$  with the Poisson filter kernel  $p_s$  in the spatial domain. The kernel of the two-dimensional Poisson operator  $\mathcal{P}_s$ ,

$$p_s(x, y) = \frac{s}{2\pi (s^2 + x^2 + y^2)^{\frac{3}{2}}}, \quad (1.67)$$

acts as a low pass filter which degrades to the Dirac delta distribution  $\delta$  for  $s$  tending to zero, i.e.  $s \rightarrow 0$ .

**Theorem 1.4.1.**

$$\lim_{s \rightarrow 0} \frac{s}{2\pi (s^2 + x^2 + y^2)^{\frac{3}{2}}} = \delta_0(x) \delta_0(y) \quad (1.68)$$

*Proof:* Like in [15] the one-dimensional Dirac delta distribution can be defined by

$$\delta_0(t) = \begin{cases} 0 & , t \neq 0, \\ \infty & , t = 0 \end{cases} \quad (1.69)$$

and

$$\int_{t \in \mathbb{R}} \delta_0(t) dt = 1. \quad (1.70)$$

The two-dimensional Dirac delta impulse is defined by the product of the one-dimensional Dirac delta distributions in all directions. The integral property changes to

$$\int_{(x,y) \in \mathbb{R}^2} \delta_0(x) \delta_0(y) d(x, y) = 1. \quad (1.71)$$

In case  $s = 0$  and  $(x, y) \neq (0, 0)$  we have  $p_s(x, y) = 0$ . For  $s > 0$ ,  $p_s(0, 0) = \frac{1}{2\pi s^2}$  so that  $\lim_{s \rightarrow 0} p_s(0, 0) = \infty$ . Furthermore,

$$\int_{(x,y) \in \mathbb{R}^2} p_s(x, y) d(x, y) = \frac{1}{2\pi} \int_{\psi=0}^{2\pi} \int_{\theta=0}^{\pi/2} \sin \theta d\theta d\psi = 1 \quad \forall s > 0 \quad \square \quad (1.72)$$

The Poisson filter kernel maps the original signal to the Poisson scale space component  $f_p$  of the signal,

$$f_p = \mathcal{P}_s\{f\}(z) = (p_s * f)(x, y). \quad (1.73)$$

Besides, there are two conjugate Poisson kernels as the scale space representation of the generalized Hilbert transform. Note, that in the following we will write  $f_{x^i y^j}(x, y, s)$  for the real valued Hilbert transformed signal component of order  $n \geq 0$ , with  $n = i + j$  and  $f_{x^0 y^0} = f$ . The Hilbert transformed signal component will be evaluated at the position  $(x, y, s)$  with spatial coordinates  $(x, y) \in \mathbb{R}^2$  and scale space parameter  $s \in \mathbb{R}_+$ . Please do not mix this notation up with the well known notation of the partial derivatives. Furthermore, we will abbreviate  $f_{x^i y^j}(x, y, s)$  by the instance

$$f_{x^i y^j} := f_{x^i y^j}(x, y, s)|_{(x,y,s)=(x_0,y_0,s_0)} \quad (1.74)$$

evaluated at a certain test point.

$$\begin{aligned}
 \begin{bmatrix} f_x \\ f_y \end{bmatrix} (x, y, s) &= \begin{bmatrix} \mathcal{Q}_x^{(1)}\{f\} \\ \mathcal{Q}_y^{(1)}\{f\} \end{bmatrix} (x, y, s) \\
 &= \begin{bmatrix} (q_x^{(1)}(\cdot, s) * f) \\ (q_y^{(1)}(\cdot, s) * f) \end{bmatrix} (z) \\
 &= \begin{bmatrix} (h_x^{(1)} * p_s * f) \\ (h_y^{(1)} * p_s * f) \end{bmatrix} (x, y)
 \end{aligned} \tag{1.75}$$

with the convolution kernels in the spatial domain

$$\begin{bmatrix} q_x^{(1)} \\ q_y^{(1)} \end{bmatrix} (x, y; s) = \frac{1}{2\pi (s^2 + x^2 + y^2)^{\frac{3}{2}}} \begin{bmatrix} x \\ y \end{bmatrix}, \tag{1.76}$$

see Figure (1.6). The vector

$$[f_p, f_x, f_y]^T \tag{1.77}$$

constitutes the monogenic scale space of the original signal  $f$ . For signal analysis a small passband of the original signal spectrum must be created. This can be done by the so called difference of Poisson (DoP) operator kernel

$$p_{s_c, s_f}(x, y) = p_{s_f}(x, y) - p_{s_c}(x, y) \tag{1.78}$$

which is defined by the coarse scale space parameter  $s_c$  and the fine scale space parameter  $s_f$  with  $s_c > s_f > 0$ .

### 1.4.1. Second Order Hilbert Transform

In order to use the higher order generalized Hilbert kernels in the Poisson scale space concept, their Poisson transforms in the spatial domain are needed. They can be obtained by convolution of the kernels with the Poisson kernel in  $\mathbb{R}^2$ . We will demonstrate that in this section for the second order Hilbert transform [21], and in the next section for the third order Hilbert transform.

To calculate the convolution in frequency space, the Fourier transforms  $\mathcal{F}\{\cdot\}(u)$  of the convolution kernels  $h^{(2)}(x, y)$  and  $p_s(x, y)$  are considered. According to the convolution theorem, the convolution in the spatial domain corresponds to a multiplication in Fourier space and viceversa. The Fourier transform of  $h^{(2)}(x, y)$  results in the multiplier

$$\mathcal{F}\{h^{(2)}\}(u) = -\frac{\bar{u}}{u} \tag{1.79}$$

with  $u = u_1 + \mathbf{i}u_2 \in \mathbb{C}$  and the conjugate  $\bar{u} = u_1 - \mathbf{i}u_2$ . The Fourier transform of the Poisson convolution kernel  $p_s(x, y)$  is obtained as

$$\mathcal{F}\{p_s\}(u) = e^{-2\pi\|u\|s}. \tag{1.80}$$

1. Introduction

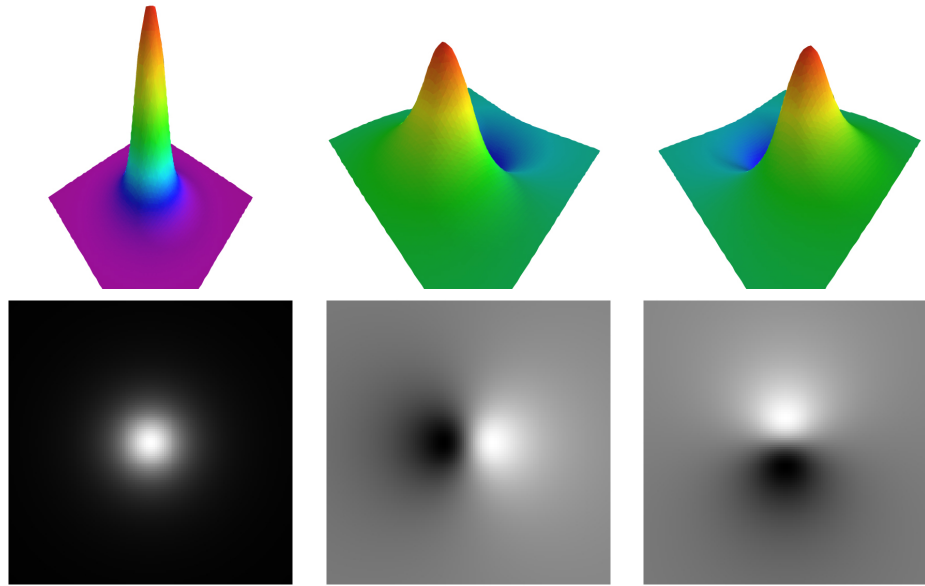


Figure 1.6.: From left to right: Poisson convolution kernel  $p_s$  and conjugate Poisson convolution kernels  $q_x^{(1)}$  and  $q_y^{(1)}$  in the spatial domain for a certain scale space parameter  $s > 0$ .

By representing the frequency domain in polar coordinates, with  $u = r [\cos \theta + \mathbf{i} \sin \theta]$ , and  $z = x + \mathbf{i}y = k [\cos \varphi + \mathbf{i} \sin \varphi]$ , the frequency transfer functions of these kernels read

$$\mathcal{F}\{h^{(2)}\}(u) = -\frac{e^{-\mathbf{i}\theta}}{e^{\mathbf{i}\theta}} = -e^{-\mathbf{i}2\theta} \quad (1.81)$$

and

$$\mathcal{F}\{p_s\}(u) = e^{-2\pi r s} . \quad (1.82)$$



Using the polar coordinate representation of the inverse two-dimensional Fourier transform to obtain the spatial domain representation of the kernels yields

$$\begin{aligned}
 (p_s * h^{(2)})(z) &= \mathcal{F}^{-1}\{-e^{-2\pi r s} e^{-i2\theta}\}(z) \\
 &= 2\pi \int_{r=0}^{\infty} \int_{\theta=0}^{2\pi} -e^{-2\pi r s} e^{-i2\theta} e^{i2\pi k r \cos(\theta-\varphi)} r \, d\theta \, dr \\
 &= 2\pi \int_{r=0}^{\infty} \int_{\theta=0}^{2\pi} -e^{-2\pi r s} e^{-i2(\theta+\varphi)} e^{i2\pi k r \cos(\theta-\varphi+\varphi)} r \, d\theta \, dr \\
 &= -2\pi e^{-i2\varphi} \int_{r=0}^{\infty} e^{-2\pi r s} \underbrace{\left[ \int_{\theta=0}^{2\pi} e^{-i2\theta} e^{-i2\pi k r \cos \theta} \, d\theta \right]}_{=J_2(2\pi k r)} r \, dr \\
 &= -2\pi e^{-i2\varphi} \int_{r=0}^{\infty} e^{-2\pi r s} J_2(2\pi k r) r \, dr \tag{1.83}
 \end{aligned}$$

where  $J_2$  is a Bessel function of the first kind and second order [56]. In the following the abbreviations  $\alpha = 2\pi s$  and  $\beta = 2\pi k$  will be used. According to the recurrence relation for Bessel functions  $J_2$  can be written as

$$J_2(2\pi k r) = J_2(\beta r) = \frac{2}{\beta r} J_1(\beta r) - J_0(\beta r) \tag{1.84}$$

since the recurrence relation reads

$$J_\nu(x) = \frac{2(\nu-1)}{x} J_{\nu-1}(x) - J_{\nu-2}(x) . \tag{1.85}$$

These results lead to

$$\begin{aligned}
 (p_s * h^{(2)})(z) &= -2\pi e^{-i2\varphi} \int_{r=0}^{\infty} e^{-\alpha r} J_2(2\pi k r) r \, dr \\
 &= -2\pi e^{-i2\varphi} \int_{r=0}^{\infty} e^{-\alpha r} \frac{2}{\beta r} J_1(\beta r) r \, dr + 2\pi e^{-i2\varphi} \int_{r=0}^{\infty} e^{-\alpha r} J_0(\beta r) r \, dr \\
 &= -2\pi e^{-i2\varphi} \left[ \frac{2}{\beta} \int_{r=0}^{\infty} e^{-\alpha r} J_1(\beta r) dr - \int_{r=0}^{\infty} e^{-\alpha r} J_0(\beta r) r \, dr \right] . \tag{1.86}
 \end{aligned}$$

According to the common integral table [27] one obtains the evaluation of the two Bessel integrals as

$$\frac{2}{\beta} \int_{r=0}^{\infty} e^{-\alpha r} J_1(\beta r) \, dr = \frac{2 \left[ \sqrt{\alpha^2 + \beta^2} - \alpha \right]}{\beta^2 \sqrt{\alpha^2 + \beta^2}} \tag{1.87}$$

## 1. Introduction

since

$$\int_{r=0}^{\infty} e^{-\alpha r} J_{\nu}(\beta r) dr = \frac{[\sqrt{\alpha^2 + \beta^2} - \alpha]^{\nu}}{\beta^{\nu} \sqrt{\alpha^2 + \beta^2}}, \quad (1.88)$$

see [27] on page 694 for  $\nu = 1$ , and

$$\int_{r=0}^{\infty} e^{-\alpha r} J_0(\beta r) r dr = \frac{2\alpha \Gamma(\frac{3}{2})}{\sqrt{\pi}(\alpha^2 + \beta^2)^{\frac{3}{2}}} = \frac{\alpha}{(\alpha^2 + \beta^2)^{\frac{3}{2}}} \quad (1.89)$$

since  $\Gamma(\frac{3}{2}) = \frac{\sqrt{\pi}}{2}$  and

$$\int_{r=0}^{\infty} e^{-\alpha r} J_{\nu}(\beta r) r^{\nu+1} dr = \frac{2\alpha(2\beta)^{\nu} \Gamma(\nu + \frac{3}{2})}{\sqrt{\pi}(\alpha^2 + \beta^2)^{\nu + \frac{3}{2}}}, \quad (1.90)$$

see [27] on page 702 for  $\nu = 0$ . Plugging these results in the equations above results in

$$\begin{aligned} (h^{(2)} * p_s)(z) &= -2\pi e^{-i2\varphi} \int_{r=0}^{\infty} e^{-\alpha r} J_2(2\pi k r) r dr \\ &= \frac{s(2s^2 + 3\|z\|^2) - 2(s^2 + \|z\|^2)^{\frac{3}{2}}}{2\pi\|z\|^4 (s^2 + \|z\|^2)^{\frac{3}{2}}} (x^2 - 2ixy - y^2) \end{aligned} \quad (1.91)$$

with

$$e^{-i2\varphi} = [e^{-i\varphi}]^2 = \left[ \frac{\bar{z}}{\|z\|} \right]^2 = \frac{(x - iy)^2}{\|z\|^2} = (x^2 - 2ixy - y^2) \frac{1}{\|z\|^2}. \quad (1.92)$$

These results lead to the three different two-dimensional convolution kernels in the spatial domain of the second order generalized Hilbert transform in Poisson scale space

$$\begin{bmatrix} q_{xx}^{(2)} \\ q_{xy}^{(2)} \\ q_{yy}^{(2)} \end{bmatrix} (x, y; s) = \frac{s(2s^2 + 3(x^2 + y^2)) - 2(s^2 + x^2 + y^2)^{\frac{3}{2}}}{2\pi(x^2 + y^2)^2 (s^2 + x^2 + y^2)^{\frac{3}{2}}} \begin{bmatrix} x^2 \\ xy \\ y^2 \end{bmatrix} \quad (1.93)$$

with  $q_{\nu\mu}^{(2)}(z; s) = (h_{\nu\mu}^{(2)} * p_s)(z)$ , see Figure (1.7) and refer to [15].

### 1.4.2. Third Order Hilbert Transform

The Fourier transform of the convolution kernel  $h^{(3)}$  results in the multiplier

$$\mathcal{F}\{h^{(3)}\}(u) = -e^{-i3\theta}. \quad (1.94)$$

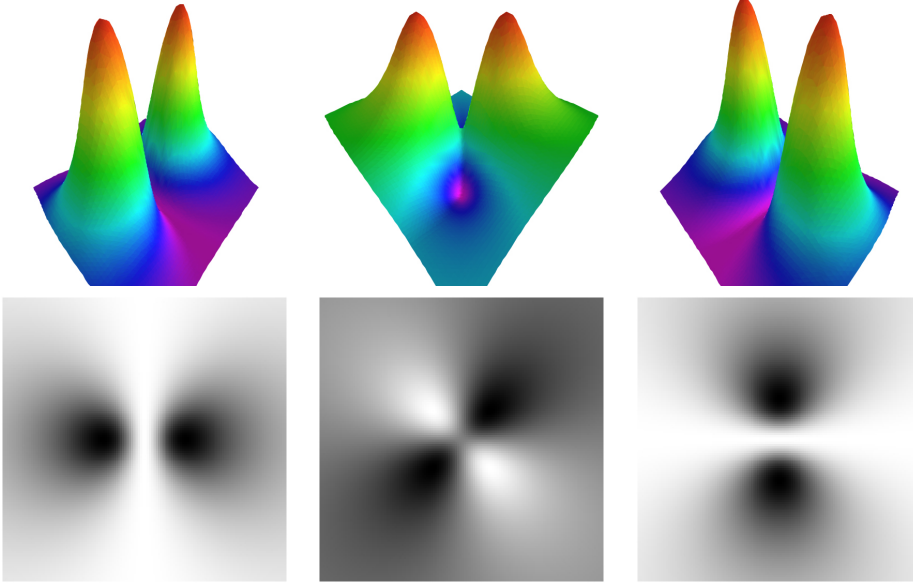


Figure 1.7.: From left to right: Second order Hilbert transform convolution kernels in the spatial domain  $q_{xx}^{(2)}$ ,  $q_{xy}^{(2)}$  and  $q_{yy}^{(2)}$  for a certain scale space parameter  $s > 0$ .

In the same way as for the second order Hilbert transform we now compute the representation of the third order Hilbert transform in Poisson scale space

$$\begin{aligned}
 (h^{(3)} * p_s)(z) &= \mathcal{F}^{-1}\{-e^{-2\pi r s} e^{-i3\theta}\}(z) \\
 &= 2\pi \int_{r=0}^{\infty} \int_{\theta=0}^{2\pi} -e^{-2\pi r s} e^{-i3\theta} e^{i2\pi k r \cos(\theta-\varphi)} r \, d\theta \, dr \\
 &= 2\pi \int_{r=0}^{\infty} \int_{\theta=0}^{2\pi} -e^{-2\pi r s} e^{-i3(\theta+\varphi)} e^{i2\pi k r \cos(\theta-\varphi+\varphi)} r \, d\theta \, dr \\
 &= -2\pi e^{-i3\varphi} \int_{r=0}^{\infty} e^{-2\pi r s} \underbrace{\left[ \int_{\theta=0}^{2\pi} e^{-i3\theta} e^{-i2\pi k r \cos \theta} \, d\theta \right]}_{=J_3(2\pi k r)} r \, dr \\
 &= -2\pi e^{-i3\varphi} \int_{r=0}^{\infty} e^{-2\pi r s} J_3(2\pi k r) r \, dr \tag{1.95}
 \end{aligned}$$

## 1. Introduction

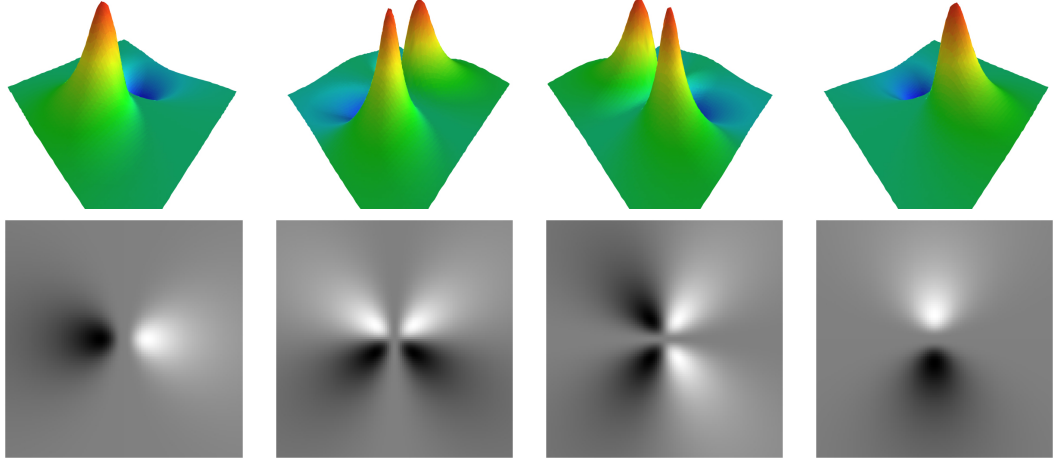


Figure 1.8.: From left to right: Third order generalized Hilbert transform convolution kernels in the spatial domain  $q_{xxx}^{(3)}$ ,  $q_{xxy}^{(3)}$ ,  $q_{xyy}^{(3)}$  and  $q_{yyy}^{(3)}$  for a certain scale space parameter  $s > 0$ .

with

$$J_3(2\pi kr)r = J_3(\beta r)r = \frac{4}{\beta r} J_2(\beta r)r - J_1(\beta r)r \quad (1.96)$$

$$J_3(\beta r) = \frac{4}{\beta r} \left( \frac{1}{\beta r} J_1(\beta r)r - J_0(\beta r)r \right) - J_1(\beta r)r \quad (1.97)$$

$$J_3(\beta r) = \frac{4}{\beta^2 r} J_1(\beta r) - \frac{4}{\beta} J_0(\beta r) - J_1(\beta r)r \quad (1.98)$$

and with

$$\int_{r=0}^{\infty} e^{-\alpha r} J_\nu(\beta r)r^\nu dr = \frac{(2\beta)^\nu \Gamma(\nu + \frac{1}{2})}{\sqrt{\pi}(\alpha^2 + \beta^2)^{\nu + \frac{1}{2}}}. \quad (1.99)$$

The two-dimensional convolution kernels in the spatial domain of the third order Hilbert transform in Poisson scale space read

$$\begin{bmatrix} q_{xxx}^{(3)} \\ q_{xxy}^{(3)} \\ q_{xyy}^{(3)} \\ q_{yyy}^{(3)} \end{bmatrix} (z; s) = \frac{4s^2 (2s^2 + 3\|z\|^2) + 3\|z\|^4 - 8s (s^2 + \|z\|^2)^{3/2}}{2\pi\|z\|^6 (s^2 + \|z\|^2)^{3/2}} \begin{bmatrix} x^3 \\ x^2y \\ xy^2 \\ y^3 \end{bmatrix} \quad (1.100)$$

with  $q_{\nu^i \mu^j}^{(i+j)}(z; s) = \left( h_{\nu^i \mu^j}^{(i+j)} * p_s \right) (z)$  for  $i, j \in \mathbb{N}$ , see Figure (1.8) and refer to [15].

## 2. The Monogenic Signal Revisited

Generalizing the construction of the one-dimensional analytic signal in Section (1.1.1) to multi-dimensional signals, the analytic signal becomes a monogenic (holomorphic) signal. Now we are looking for a function with the property of being monogenic. The associated boundary value problem of the second kind is

$$\begin{cases} \Delta f_M = \frac{\partial^2}{\partial x^2} f_M + \frac{\partial^2}{\partial y^2} f_M + \frac{\partial^2}{\partial s^2} f_M = 0, & s > 0, \\ \frac{\partial}{\partial s} f_M = f(x, y), & s = 0. \end{cases} \quad (2.1)$$

with

$$D = \mathbf{e}_1 \frac{\partial}{\partial x} + \mathbf{e}_2 \frac{\partial}{\partial y} + \mathbf{e}_3 \frac{\partial}{\partial s}, \quad (2.2)$$

$\Delta = D^2$ , and  $\mathbf{e}_\nu$  as the basis vectors of the Euclidean space. The first Equation (2.1) is the 3D-Laplace equation restricted to the open half-space  $s > 0$  and the second equation is the boundary condition. Using the fundamental solution of the 3D-Laplace equation, the solution of this problem is the monogenic signal  $f_M : \Omega \times \mathbb{R}_+ \mapsto \mathbb{H}$

$$f_M = \mathcal{P}_s\{f\}(z) + \mathbf{i} (h_x^{(1)} * \mathcal{P}_s\{f\})(z) + \mathbf{j} (h_y^{(1)} * \mathcal{P}_s\{f\})(z) \quad (2.3)$$

with  $z = (x, y) \in \Omega \subseteq \mathbb{R}^2$  and  $(\mathbb{H}, +, \cdot)$  as the quaternions. The novelty of the monogenic signal is the interpretation of the underlying local i1D signal structure. In this thesis all of our signal functions can be extended to a monogenic function, but the question is what kind of signals can be analyzed by the monogenic signal and how the results of the monogenic signal can be interpreted. Because of that a local signal model must be defined with certain signal properties, which can be retrieved by the monogenic signal.

### 2.1. Local Signal Model

The i1D signal model, which is an arbitrarily orientated one-dimensional signal in higher-dimensional domain, in Poisson scale space for each scale parameter  $s > 0$  reads

$$\mathcal{P}_s\{f\}(z) = a \cos(x \cos \theta + y \sin \theta + \phi). \quad (2.4)$$

The resulting local signal model at the origin  $z = (x, y) \in \mathbb{R}^2$  of the local coordinate system reads

$$f_p = \mathcal{P}_s\{f\}(z) = a \cos \phi. \quad (2.5)$$

## 2. The Monogenic Signal Revisited

For a real two-dimensional signal  $f \in L^2(\Omega, \mathbb{R})$  with  $\Omega \subseteq \mathbb{R}^2$  the monogenic signal  $f_M$  [16] can be defined in vector notation

$$f_M = \begin{bmatrix} f_p \\ f_x \\ f_y \end{bmatrix} = \frac{1}{2\pi} \int_{\mathbb{R}^2} \frac{f(\mu, \nu)}{(s^2 + (x - \mu)^2 + (y - \nu)^2)^{\frac{3}{2}}} \begin{bmatrix} s \\ x - \mu \\ y - \nu \end{bmatrix} d(\mu, \nu) \quad (2.6)$$

in Poisson scale space for each scale parameter  $s > 0$ . The restriction of the monogenic signal is, that it can only be interpreted exactly in the case of pure i1D signals.

## 2.2. First Order Hilbert Transform in Radon Space

The two-dimensional Radon transform of the original signal  $f$  will be abbreviated by

$$f_r(t, \theta, s) = \mathcal{R} \{ \mathcal{P}_s \{ f \} \} (t, \theta) \quad (2.7)$$

and the inverse two-dimensional Radon transform by  $\mathcal{R}^{-1}$  [45], see Figure (2.1). By the important relation

$$\begin{bmatrix} f_x \\ f_y \end{bmatrix} = \mathcal{R}^{-1} \left\{ (t, \theta) \mapsto \begin{bmatrix} \cos \theta \\ \sin \theta \end{bmatrix} (h * f_r(\cdot, \theta, s))(t) \right\} (z), \quad (2.8)$$

in two-dimensional signal domain, which can be reduced to the one-dimensional Hilbert transform

$$(h * g(\cdot, s))(t)|_{t=t_0} = a \sin \phi \quad (2.9)$$

with the partial one-dimensional function in direction  $\theta$

$$g(t, s) = \mathcal{P}_s \{ f \} (t \cos \theta, t \sin \theta), \quad (2.10)$$

and the one-dimensional Hilbert transform kernel  $h(t) = \frac{1}{\pi t}$ , it can be shown that the conjugate part of the monogenic signal results in

$$\begin{bmatrix} f_x \\ f_y \end{bmatrix} = \begin{bmatrix} \mathcal{Q}_x^{(1)} \{ f \} \\ \mathcal{Q}_y^{(1)} \{ f \} \end{bmatrix} = \begin{bmatrix} \cos \theta \\ \sin \theta \end{bmatrix} a \sin \phi \quad (2.11)$$

for all i1D signals.

## 2.3. Interpretation of the Monogenic Signal

Now the monogenic signal, which is a vector valued function

$$f_M = \begin{bmatrix} f_p \\ f_x \\ f_y \end{bmatrix}, \quad (2.12)$$

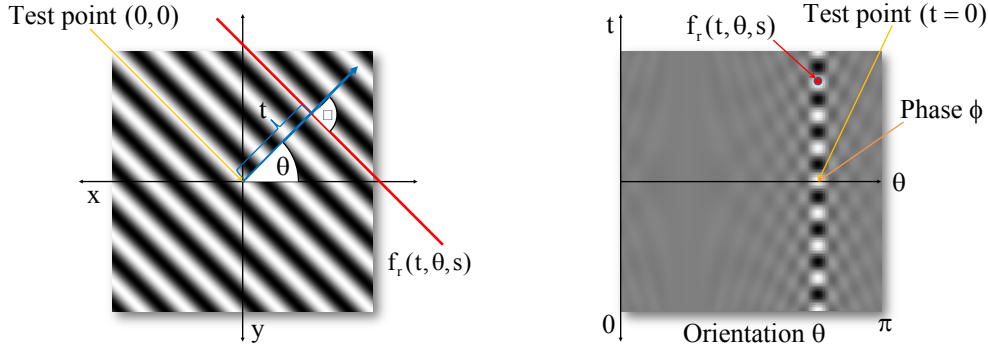


Figure 2.1.: Left figure: 1D signal  $f_p$  in the spatial domain with orientation  $\theta_m$  and local phase  $\phi = 0$  at the origin  $z = (x, y) \in \mathbb{R}^2$  of the applied local coordinate system. Right figure: 1D signal  $f_p$  in Radon space. Each point in Radon space represents the integral in the spatial domain on a line which is uniquely defined by the minimal distance  $t \in \mathbb{R}$  to the origin and the orientation  $\theta \in [0, \pi)$ . The Radon transform of the Poisson filtered signal will be abbreviated by  $f_r(t, \theta, s) = \mathcal{R}\{\mathcal{P}_s\{f\}\}(t, \theta)$ .

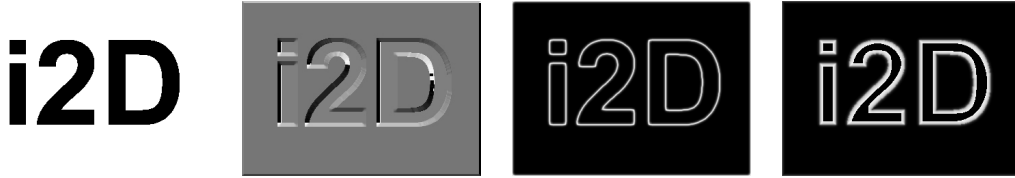


Figure 2.2.: Illustration of the experimental results from left to right: original image signal, local orientation, local amplitude and local phase by the 2D monogenic signal in Poisson scale space for a certain scale space parameter  $s > 0$ .

see Figure (2.3), can be used to solve for the unknown local amplitude  $a \in \mathbb{R}_+$ , the local orientation  $\theta \in [0, \pi)$  and the local phase  $\phi \in [0, \pi)$

$$\theta = \arctan \frac{f_y}{f_x}, \quad (2.13)$$

$$\phi = \arctan \frac{\sqrt{f_x^2 + f_y^2}}{f_p}, \quad (2.14)$$

$$a = \sqrt{f_p^2 + f_x^2 + f_y^2}, \quad (2.15)$$

see Figure (2.2) for experimental results.

*Proof:* The proof will be easy with the previous results of the expression in two-dimensional Radon space

$$\begin{bmatrix} f_p \\ f_x \\ f_y \end{bmatrix} = a \begin{bmatrix} \cos \phi \\ \sin \phi \cos \theta \\ \sin \phi \sin \theta \end{bmatrix}. \quad (2.16)$$

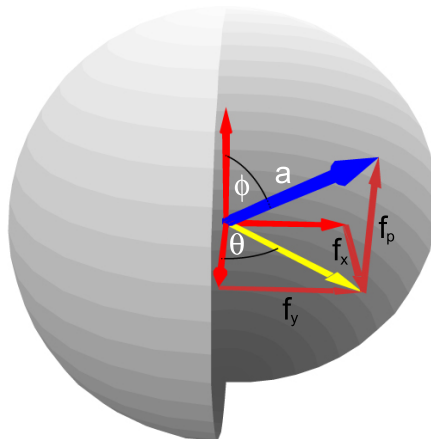


Figure 2.3.: Geometric illustration and interpretation of the 2D monogenic signal vector  $[f_p, f_x, f_y]^T$  in 3D Euclidean space.

□

At phase positions  $\phi = k\pi$  for all  $k \in \mathbb{Z}$  the orientation cannot be evaluated. Note that the local features must be evaluated for each scale space parameter  $s > 0$  since in general the signal consists locally of different frequency components, see Figure (2.2). Now the problem of isotropic i1D signal analysis is totally solved. The next step will be the modeling of i1D and i2D signals and the exact solution for their parameters. Abstractly spoken, local signal analysis is the solution of its corresponding inverse problem [4].

### 2.3.1. Phase Vector

The phase vector  $\Phi_{2D} \in \mathbb{R}^2$  of the monogenic signal is defined by

$$\Phi_{2D} = \begin{bmatrix} \Phi_x \\ \Phi_y \end{bmatrix} = \phi \begin{bmatrix} \cos \theta \\ \sin \theta \end{bmatrix} \quad (2.17)$$

consisting of the local main orientation  $\theta$  and the local phase  $\phi$ . The original signal can be reconstructed from the amplitude and phase information by using the definition of the signal model

$$f = a \cos \phi + f_{DC}(z) \quad (2.18)$$

up to the signals DC-component  $f_{DC}$  (offset). Since the monogenic signal is strictly limited to the class of i1D signals, the aim of this thesis is to find and solve an appropriate geometrical interpretation for i1D and i2D signals in one single framework.

### 2.3.2. Main Orientation

For a general derivation of the main orientation of the original signal by the first order generalized Hilbert transform, the assumed i1D signal model will be extended to a



superposition of i1D signals with arbitrary but same amplitude  $a$  and phase  $\phi$  and with arbitrary and individual orientations  $\theta_i$

$$\mathcal{P}_s\{f\}(x, y) = \sum_{i \in I} a \cos(x \cos \theta_i + y \sin \theta_i + \phi) \quad (2.19)$$

for each individual scale space parameter  $s$  and with  $I$  as the index set of the individual orientations  $\theta_i$ . To be able to extract orientation and phase information from the generalized Hilbert transformed signal, the inverse Radon transform must be simplified. This can be achieved by two assumptions.

- Firstly, without loss of generality the point of interest where local feature information should be obtained will be translated to the origin of the local coordinate system for each point  $(x, y) \in \Omega \subset \mathbb{R}^2$  so that the inverse two-dimensional Radon transform has to be evaluated only at  $z = (x, y)$ . Let

$$\Theta = [0, \pi) \setminus \bigcup_{i \in I} \{\theta_i\} \quad (2.20)$$

be the set of all orientations where no i1D signal information exists.

- Secondly, the  $\theta$ -integral of the inverse Radon transform vanishes, see Figure (2.4), because

$$\begin{aligned} f_r(t_1, \theta, s) &= f_r(t_2, \theta, s) \quad \forall t_1, t_2 \in \mathbb{R} \quad \forall \theta \in \Theta \\ \Rightarrow \frac{\partial}{\partial t} f_r(t, \theta, s) &= 0 \quad \forall t \in \mathbb{R} \quad \forall \theta \in \Theta \end{aligned} \quad (2.21)$$

for a finite number  $\|I\| \in \mathbb{N}$  of superimposed i1D signals. Because of this fact (and the linearity property of the Radon transform), the  $\theta$ -integral of the inverse Radon transform can be replaced by a finite sum of discrete angles  $\theta_i$  to enable modeling the superposition of an arbitrary number of i1D signals. Therefore, the inverse Radon transform for a finite number of superimposed i1D signals can be written as

$$\mathcal{R}^{-1} \{(t, \theta) \mapsto f_r\}(x, y)|_{(x,y)=(0,0)} = -\frac{1}{2\pi^2} \sum_{i \in I} \text{P.V.} \int_{t \in \mathbb{R}} \frac{1}{t} \frac{\partial}{\partial t} f_r(t, \theta_i) dt, \quad (2.22)$$

with  $(x, y) = (0, 0)$  as the test point without loss of generality. Now the first order 2D generalized Hilbert transform and therefore the monogenic signal can be interpreted in an explicit way for the application to i1D signals and the extended but restricted set of superimposed i1D signals.

Because of the property [56]

$$\frac{\partial}{\partial t} [(h * f_r(\cdot, \theta, s))(t)] = (h * \frac{\partial}{\partial t} f_r(t, \theta, s))(t) \quad (2.23)$$

## 2. The Monogenic Signal Revisited

the 2D generalized Hilbert transform of any i1D signal with orientation  $\theta_m$  results in

$$\begin{aligned}
\begin{bmatrix} f_x \\ f_y \end{bmatrix} &= \mathcal{R}^{-1} \left\{ (t, \theta) \mapsto \begin{bmatrix} \cos \theta \\ \sin \theta \end{bmatrix} (h * f_r(\cdot, \theta))(t) \right\} \\
&= -\frac{1}{2\pi^2} \sum_{i \in \{m\}} \text{P.V.} \int_{t \in \mathbb{R}} \frac{1}{t} \frac{\partial}{\partial t} \left\{ \begin{bmatrix} \cos \theta_i \\ \sin \theta_i \end{bmatrix} (h * f_r(\cdot, \theta_i))(t) \right\} dt \\
&= -\frac{1}{2\pi^2} \text{P.V.} \int_{t \in \mathbb{R}} \frac{1}{t} \frac{\partial}{\partial t} \left\{ \begin{bmatrix} \cos \theta_m \\ \sin \theta_m \end{bmatrix} (h * f_r(\cdot, \theta_m, s))(t) \right\} dt \\
&= \underbrace{-\frac{1}{2\pi^2} \text{P.V.} \int_{t \in \mathbb{R}} \frac{1}{t} \left( h * \frac{\partial}{\partial t} f_r(t, \theta_m, s) \right) (t) dt}_{c_m} \begin{bmatrix} \cos \theta_m \\ \sin \theta_m \end{bmatrix}. \tag{2.24}
\end{aligned}$$

With the assumption that two superimposed i1D signals have arbitrary but same phase and arbitrary but same amplitude, the main orientation  $\theta_m$ , or in other words: the main orientation of the resulting i2D signal can be calculated by

$$\begin{aligned}
\begin{bmatrix} f_x \\ f_y \end{bmatrix} &= c_m \begin{bmatrix} \cos \theta_1 + \cos \theta_2 \\ \sin \theta_1 + \sin \theta_2 \end{bmatrix} \\
\Rightarrow \arctan \frac{f_y}{f_x} &= \frac{1}{2} (\theta_1 + \theta_2) = \theta_m. \tag{2.25}
\end{aligned}$$

This result can now be extended to the superposition of an arbitrary number of i1D signals

$$\begin{bmatrix} f_x \\ f_y \end{bmatrix} = \sum_{i \in I} \underbrace{\left[ -\frac{1}{2\pi^2} \text{P.V.} \int_{t \in \mathbb{R}} \frac{1}{t} \left( h * \frac{\partial}{\partial t} f_r(t, \theta_i, s) \right) (t) dt \right]}_{c_i} \begin{bmatrix} \cos \theta_i \\ \sin \theta_i \end{bmatrix}. \tag{2.26}$$

In general the mean value of a number  $\|I\|$  of superimposed i1D signals can now be easily calculated by

$$\begin{aligned}
c_m &= c_1 = \dots = c_{\|I\|} \\
\Rightarrow \begin{bmatrix} f_x \\ f_y \end{bmatrix} &= c_m \begin{bmatrix} \sum_{i \in I} \cos \theta_i \\ \sum_{i \in I} \sin \theta_i \end{bmatrix} \\
\Rightarrow \arctan \frac{f_y}{f_x} &= \frac{1}{\|I\|} \sum_{i \in I} \theta_i = \theta_m. \tag{2.27}
\end{aligned}$$

The most important conclusion of this result is that the monogenic signal can be used not only to interpret pure i1D signals but also to calculate the main orientation of the superposition of two and more i1D signals with arbitrary but same phase and arbitrary but same amplitude at the test point of local interest. This does not hold for the exact

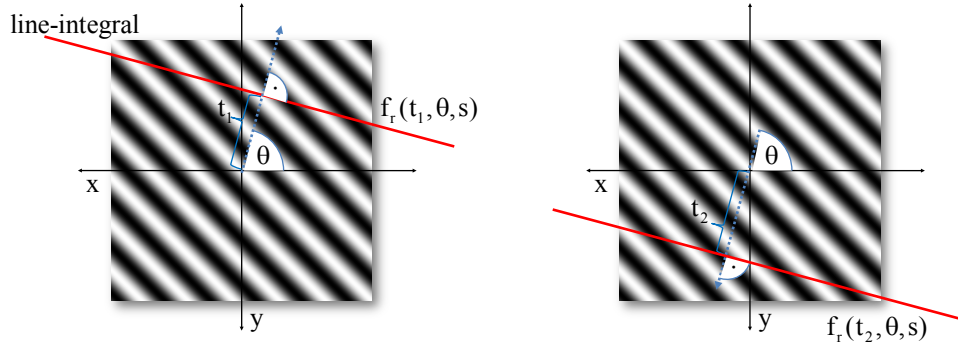


Figure 2.4.: For each distance parameter  $t$  and for all orientations  $\theta$  - except for the main orientation  $\theta_m$  - the line integral on all function values in the signal domain is the same, i.e.  $f_r(t_1, \theta, s) = f_r(t_2, \theta, s)$ .

phase and the amplitude interpretation of an arbitrary signal. In this case the monogenic signal can only be applied to pure 1D signals.

Summarized, the problem of exact signal analysis will always be that a certain signal model must be assumed. If the assumed signal model deviates from the original signal, which is being analyzed, the interpretation degrades and generates errors which cannot be avoided.

## 2.4. Exploiting the Properties of Monogenic Signals

The monogenic signal is the extension of the classical analytic signal to signal domains of any dimension. Remember that the analytic signal is restricted to one-dimensional signals and the monogenic signal of any signal domain is always restricted to signals of intrinsic dimension one. The monogenic signal, which results of the Poisson kernel and the conjugated Poisson kernels in all signal directions, is a left and right monogenic function, i.e. the application of the Dirac operator  $\partial$  (with its conjugated part written as  $\bar{\partial}$ ) from any side to the monogenic signal is zero. The monogenic signal can be interpreted at any signal position except for the points of singularity. It has already been shown that especially those singularities carry the most interesting signal information [61]. The monogenic signal has not been used to measure the local signal features at those points. Unfortunately, the monogenic signal cannot be interpreted at those points, so the use of monogenic signals at these points has no advantage at first glance. Nevertheless, by using the results of function theory [30] the properties of monogenic functions can be used to calculate the numerical values of the points of singularity. The central results come from the integral theorem of Cauchy. For the integral formula the Cauchy kernel has to be introduced. The Cauchy kernel is defined by

$$E_m(z) = \frac{1}{\sigma_m} \frac{\bar{z}}{\|z\|^{m+1}} \quad (2.28)$$

## 2. The Monogenic Signal Revisited

with  $z \neq \mathbf{0}$  and

$$\sigma_m = 2 \frac{\Gamma^{m+1} \left( \frac{1}{2} \right)}{\Gamma \left( \frac{m+1}{2} \right)} = \frac{2\pi^{\frac{m+1}{2}}}{\Gamma \left( \frac{m+1}{2} \right)} \quad (2.29)$$

at the surface of the unit sphere  $\mathbb{S}^m$  in the Euclidean space  $\mathbb{R}^{m+1}$ . For instance, the Cauchy kernel of the analytic signal in case of complex numbers, i.e.  $m = 1$ , simplifies to

$$E_1(z) = \frac{1}{2\pi} \frac{1}{z} \quad (2.30)$$

with  $z \in \mathbb{C}$ .

**Theorem 2.4.1.** *The Cauchy kernel is left and right monogenic.*

*Proof:*

$$\bar{\partial} \frac{\bar{z}}{\|z\|^{m+1}} = (\bar{\partial} \bar{z}) \frac{1}{\|z\|^{m+1}} + \left( \bar{\partial} (\|z\|^2)^{-\frac{m+1}{2}} \right) \bar{z} \quad (2.31)$$

and with

$$\bar{\partial} \bar{z} = \sum_{\nu=0}^m \mathbf{e}_\nu \bar{\mathbf{e}}_\nu = m + 1 \quad (2.32)$$

and

$$\bar{\partial} \|z\|^2 = 2 \sum_{\nu=0}^m z_\nu \mathbf{e}_\nu = 2z \quad (2.33)$$

it follows the left monogenic property of the Cauchy kernel

$$\bar{\partial} \frac{\bar{z}}{\|z\|^{m+1}} = 0 \quad (2.34)$$

The proof for the right monogenic property is analogous [30]. □

Let  $\Omega \subset \mathbb{R}^{m+1}$  be a restricted area with smooth border with outpointing normal vector, and let  $f_M = [f_p, f_x, f_y]^T \in C^1(\bar{\Omega})$  be a monogenic signal which is left and right monogenic. Now the Cauchy formula for monogenic signals can be introduced by

$$\int_{t \in \partial\Omega} E_m(t-z) dt^* f_M(t,s) = \int_{t \in \partial\Omega} f_M(t,s) dt^* E_m(t-z) = \begin{cases} f_M, & z \in \Omega, \\ \mathbf{0}, & z \in \mathbb{R}^{m+1} \setminus \bar{\Omega}. \end{cases} \quad (2.35)$$

For the case of two-dimensional signals ( $m = 1$ ) the Cauchy formula reads

$$-\frac{\mathbf{i}}{2\pi} \int_{w \in \partial\Omega} \frac{f_M(w,s)}{w-z} dw = \begin{cases} f_M, & z \in \Omega, \\ \mathbf{0}, & z \notin \bar{\Omega}. \end{cases} \quad (2.36)$$

which shows clearly that the monogenic signal  $f_M$  is completely defined by its border on  $\partial\Omega$ . For practical applications the integral over a closed Jordan curve  $L$  (e.g. a circle)

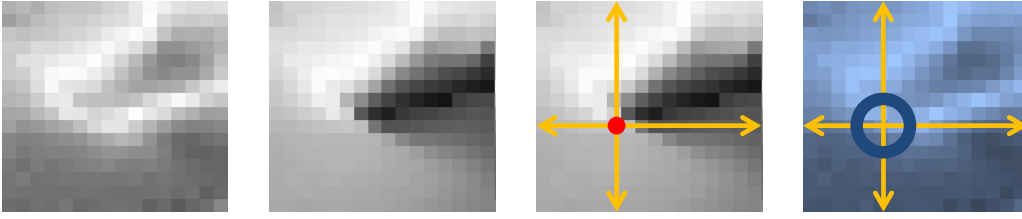


Figure 2.5.: Illustration of a phase singularity from left to right: Original image, local phase, point of phase singularity and the calculation of the Cauchy integral on a unit circle around this singularity.

around the point of interest  $z$  can be used to calculate the numerical value at the pixel position  $z$

$$f_M = -\mathbf{i} \frac{1}{2\pi} \oint_{l \in L} \frac{f_M(l, s)}{l - z} \Big|_{s=0} dl \quad (2.37)$$

for those pixel positions where a phase singularity makes the local signal interpretation impossible, see Figure (2.5).



### 3. The Conformal Monogenic Signal

The feature space of the 2D monogenic signal is spanned by amplitude, phase and orientation information. This restriction correlates to the dimension of the associated Radon space [73, 74]. Therefore, the feature space of the 2D signal can only be extended by lifting up the original signal to higher dimensions. This is one of the main ideas of the conformal monogenic signal [67, 64]. In the following the 2D monogenic signal will be generalized to analyze both i1D and i2D signals in one framework by embedding the 2D signal into the conformal space [23, 22, 24].

In Chapter 2 we have shown that the generalized 2D Hilbert transform can be expressed by the 2D Radon transform, which integrates all function values on lines. This restriction to lines is one of the reasons why the 2D monogenic signal is limited to i1D signals (such as lines and edges) with zero isophote curvature. To analyze i2D signals in addition and to measure curvature  $\kappa = \frac{1}{\rho}$  as an additive local feature, a 2D Radon transform is preferable which integrates on curved lines, i.e. circles with radius  $\rho$ . Unfortunately, the inverse Radon transform on arbitrary circles is not unique [1]. Now it will be proposed how to solve this problem in conformal space. In a 3D signal domain the Radon transform integrates on planes, although at first sight 3D planes are not related to 2D signals. The idea is that circles form the intersection of a sphere (with center at  $(0, 0, \frac{1}{2})$  and radius  $\frac{1}{2}$ ) and planes passing through the origin  $(0, 0, 0)$ . Since the generalized Hilbert transform can be extended to any dimension and the 3D generalized Hilbert transform can be expressed by the 3D Radon transform, the 2D signal coordinates must be mapped appropriately to the sphere. This mapping must be conformal, i.e. angle preserving, so that interpretation of the 3D generalized Hilbert transform in conformal space is still reasonable. Analogously to the  $(t, \theta)$  line parametrization of the 2D Radon transform, the planes of the 3D Radon transform are uniquely defined by the parameters  $(t, \theta, \varphi)$ . This parametrization truly extends the interpretation space of the monogenic signal by one dimension, see Figure (3.3). Now the 2D signal will be embedded into a

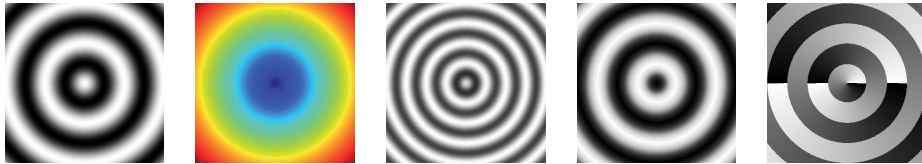


Figure 3.1.: From left to right: original synthetic i2D signal  $f(x, y) = a_0 \cos(\sqrt{x^2 + y^2} + \phi)$ , conformal monogenic signal curvature, conformal monogenic signal amplitude, phase and direction. Convolution mask size:  $11 \times 11$  pixels. Rotational invariance and isotropic properties can clearly be seen.

### 3. The Conformal Monogenic Signal

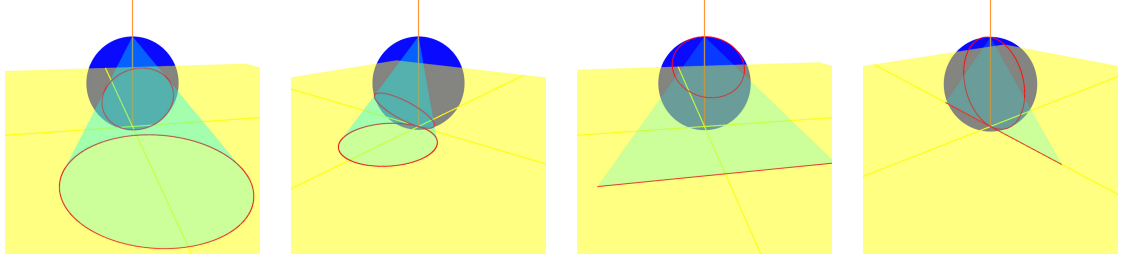


Figure 3.2.: From left to right: The first two figures illustrate circles on the plane being mapped to circles not passing through the north pole  $(0, 0, 1)$  of the sphere; and the next two figures illustrate lines on the plane being mapped to circles passing through the north pole of the sphere, i.e. lines are a special case of circles with infinite large radius.

two-dimensional subspace of the conformal space.

## 3.1. Locally Curved Signal Model

The conformal monogenic signal is able to analyze all kinds of locally curved signals

$$f(x, y) = g \left( \left\| \begin{bmatrix} x \\ y \end{bmatrix} - \frac{1}{\kappa} \begin{bmatrix} \cos \theta \\ \sin \theta \end{bmatrix} \right\|_2 \right) \in \text{i1D} \cup \text{i2D} \quad (3.1)$$

with  $\kappa$  as the local curvature and  $\theta$  as the local direction of the signal for  $\kappa \neq 0$ . For the special case of  $\kappa = 0$  the curved 2D signal degrades to an i1D function, e.g. consider the following synthetic signal shown in Figure (3.1)

$$\mathcal{P}_s\{f\}(x, y) = a \cos \left( \sqrt{\left[ x - \frac{\cos \theta}{\kappa} \right]^2 + \left[ y - \frac{\sin \theta}{\kappa} \right]^2} + \phi \right). \quad (3.2)$$

Hence the conformal monogenic signal model consists of all 2D signals, which can be locally approximated by a circle with curvature  $\kappa$  and radius  $\rho = \frac{1}{\kappa}$ .

## 3.2. The Conformal Space

One idea of the conformal monogenic signal is that the concept of lines in 2D Radon space becomes the more abstract concept of hyper-planes in 3D Radon space. These planes determine circles on the sphere in conformal space. Since lines and circles of the two-dimensional signal domain are mapped to circles [46, 30] on the sphere, see Figure (3.2), the integration on these circles determines points in the 3D Radon space. The set of points on the sphere in conformal space is defined by

$$S = \left\{ (x, y, z) : x^2 + y^2 + \left( z - \frac{1}{2} \right)^2 = \frac{1}{4} \right\}. \quad (3.3)$$



### 3.3. 3D Hilbert Transforms in Conformal Space

For dimension  $n = 2$  the inverse stereographic projection  $\mathcal{C} : \mathbb{R}^2 \mapsto S$  known from complex analysis [30] maps the 2D signal domain to the sphere

$$\mathcal{C}(x, y) = \frac{1}{1 + x^2 + y^2} \begin{bmatrix} x \\ y \\ x^2 + y^2 \end{bmatrix}. \quad (3.4)$$

The inversion  $\mathcal{C}^{-1} : S \mapsto \mathbb{R}^2$  for all elements of  $S \subset \mathbb{R}^3$  reads

$$\mathcal{C}^{-1}(x, y, z) = \frac{1}{1 - z} \begin{bmatrix} x \\ y \end{bmatrix}. \quad (3.5)$$

The inverse stereographic projection maps the Euclidian space  $\mathbb{R}^n$  to the hyper-sphere  $\mathbb{R}^{n+1}$  with radius  $\frac{1}{2}$  and the south pole of the hyper-sphere touching the origin

$$\underbrace{(0, \dots, 0)}_n \in \mathbb{R}^n \quad (3.6)$$

of the Euclidian space  $\mathbb{R}^n$  and the north pole of the hyper-sphere with coordinates

$$\underbrace{(0, 0, \dots, 0)}_n, 1 \in \mathbb{R}^{n+1}. \quad (3.7)$$

The conformal mapping  $\mathcal{C}$  has the property that the origin of the 2D signal domain will be mapped to the south pole  $\mathbf{0} = (0, 0, 0)$  of the sphere and all points at infinity  $-\infty, +\infty$  will be mapped to the north pole  $(0, 0, 1)$  of the sphere. Lines and circles of the 2D signal domain will be mapped to circles on the sphere and can be determined uniquely by planes in 3D Radon space. The integration on these planes corresponds to points  $(t, \theta, \varphi)$  in the 3D Radon space.

### 3.3. 3D Hilbert Transforms in Conformal Space

Since the signal domain  $\Omega \subset \mathbb{R}^2$  is bounded, not the whole sphere is covered by the original signal, see left part of Figure (3.3). Anyway, all planes corresponding to circles remain unchanged. That is the reason why the conformal monogenic signal models i1D lines and all kinds of curved i2D signals which can be locally approximated by circles. To give the generalized Hilbert transform more degrees of freedom, the original two-dimensional signal will be embedded in an applicable subspace of the conformal space by the so called conformal signal  $c : \mathbb{R}^3 \mapsto \mathbb{R}$  of the original 2D signal  $f$ :

$$c(\mathbf{z}) = \begin{cases} \mathcal{P}_s\{f\}(\mathcal{C}^{-1}(\mathbf{z})^T) & , x^2 + y^2 + (z - \frac{1}{2})^2 = \frac{1}{4} \\ 0 & , \text{else} \end{cases} \quad (3.8)$$

with  $\mathbf{z} = (x, y, z)$ . Thus, the 3D generalized Hilbert transform can be applied to all points on the sphere. The center of convolution in the spatial domain is the south pole

### 3. The Conformal Monogenic Signal

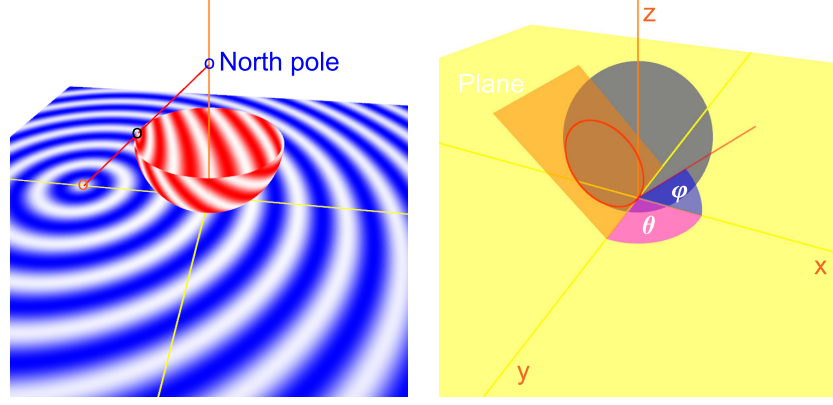


Figure 3.3.: Left figure: The inverse stereographic projection ray passes through each 2D point  $(x, y)$  and through the north pole  $(0, 0, 1)$  of the sphere. The conformal mapping of the point  $(x, y)$  is defined by the intersection of its projection ray and the sphere. Right figure: Each intersection of the sphere and a plane passing through the origin  $(0, 0, 0)$  delivers a circle. Those planes and thus all circles on the sphere are uniquely defined by the angles  $(\theta, \varphi)$  of the normal vector.

$(0, 0, 0)$  where the origin of the 2D signal domain meets the sphere. At this point the 3D generalized Hilbert transform of the conformal signal  $c$  will be evaluated

$$\mathcal{H}\{c\}(\xi)|_{\xi=(0,0,0)} = \frac{2}{A_4} \text{P.V.} \int_{x \in \mathbb{R}^3} \frac{x}{\|x\|^4} c(x - \xi) dx \quad (3.9)$$

with  $A_4$  as the surface area of the unit sphere  $\mathbb{S}^3$ . The conformal monogenic signal  $f_{\text{CMS}}$  is defined by the even part and the three odd parts of the 3D generalized Hilbert transform in conformal space

$$f_{\text{CMS}}(x, y) = \begin{bmatrix} c_p \\ c_x \\ c_y \\ c_z \end{bmatrix} = \begin{bmatrix} c(\mathbf{z}) \\ \mathcal{H}_x \{c\}(\mathbf{z}) \\ \mathcal{H}_y \{c\}(\mathbf{z}) \\ \mathcal{H}_z \{c\}(\mathbf{z}) \end{bmatrix} = \begin{bmatrix} c(\mathbf{z}) \\ \mathcal{H} \{c\}(\mathbf{z}) \end{bmatrix}. \quad (3.10)$$

Note that the coordinates  $(x, y)$  are relative to the local coordinate system for each test point of the original 2D signal and  $\mathbf{z}$  are the corresponding relative coordinates in conformal space.

Analogously to the monogenic signal in 2D the conformal monogenic signal can also be written in terms of the 3D Radon transform and its inverse

$$\mathcal{H} \{c\}(\mathbf{z}) = \mathcal{R}^{-1} \left\{ (t, \theta) \mapsto \begin{bmatrix} \sin \varphi \cos \theta \\ \sin \varphi \sin \theta \\ \cos \varphi \end{bmatrix} (h * \mathcal{R} \{c\}(\cdot, \theta, \varphi))(t) \right\}(\mathbf{z}). \quad (3.11)$$

Remember that without loss of generality the signal will be analyzed at the origin  $\mathbf{z}$  of the local coordinate system of the test point.

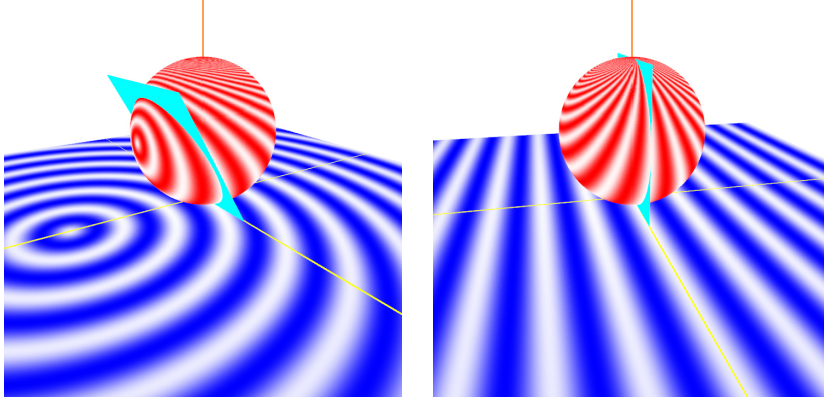


Figure 3.4.: Left figure: The plane indicates an i2D signal. Right figure: The plane of an i1D signal passes through the north pole of the sphere.

### 3.4. 3D Radon Transform in Conformal Space

To interpret the conformal monogenic signal, the relation to the 3D Radon transform in conformal space must be taken into account, see Figure (3.5). The 3D Radon transform is defined as the integral of all function values on the plane defined by  $(t, \theta, \varphi) \in \mathbb{R} \times [0, 2\pi) \times [0, \pi)$

$$c_r(t, \theta, \varphi) = \mathcal{R}\{c\}(t, \theta, \varphi) = \int_{\mathbf{x} \in \mathbb{R}^3} c(\mathbf{x}) \delta\left(\mathbf{x} \begin{bmatrix} \sin \varphi \cos \theta \\ \sin \varphi \sin \theta \\ \cos \varphi \end{bmatrix} - t\right) d\mathbf{x}. \quad (3.12)$$

Since the signal is mapped on the sphere and all other points of the conformal space are set to zero, the 3D Radon transform actually sums up all signal values lying on the intersection of the plane and the sphere. For all planes this intersection can be either empty or a circle. The concept of circles in the conformal 3D Radon transform can be compared to the concept of lines known from the 2D Radon transform. Since lines in the 2D domain are also mapped to circles, the conformal monogenic signal can analyze i1D as well as curved i2D signals in one single framework. The inverse 3D Radon transform reads

$$\mathcal{R}^{-1}\{(t, \theta, \varphi) \mapsto c_r\}(x, y, z) = -\frac{1}{8\pi^2} \int_{\theta=0}^{2\pi} \int_{\varphi=0}^{\pi} \frac{\partial^2}{\partial t^2} c_r \left( \underbrace{\mathbf{x} \begin{bmatrix} \sin \varphi \cos \theta \\ \sin \varphi \sin \theta \\ \cos \varphi \end{bmatrix}}_{=t}, \theta, \varphi \right) d\varphi d\theta \quad (3.13)$$

with  $\mathbf{x} = (x, y, z)$  which differs from the 2D inverse Radon transform such that the 3D inverse Radon transform is a local transformation [4]. That means the generalized Hilbert transform at  $\mathbf{x} = (0, 0, 0)$  is completely determined by all hyper-planes passing through the origin, i.e.  $t = 0$ . In contrast to that result, the 2D monogenic signal

### 3. The Conformal Monogenic Signal

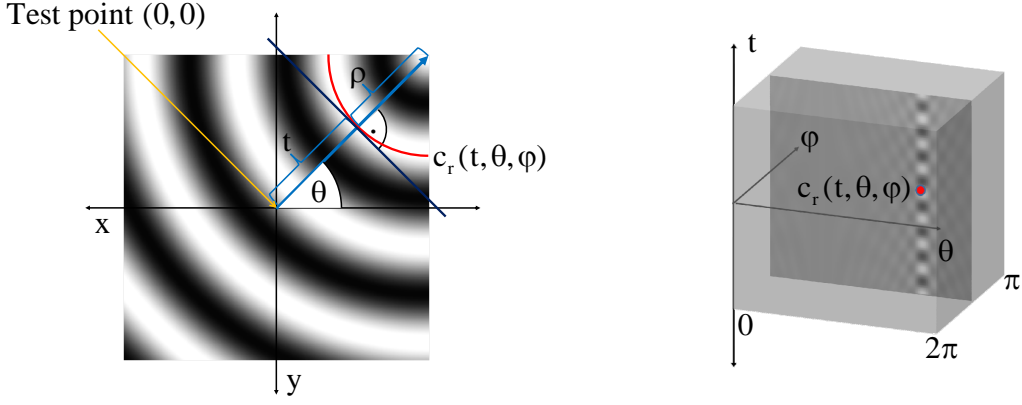


Figure 3.5.: Left figure: Curved i2D signal with direction  $\theta$  and curvature  $\kappa = \frac{1}{\rho}$ . Right figure: Corresponding 3D Radon space representation of the i2D signal spanned by the parameters  $t$ ,  $\theta$  and  $\varphi$ . Since the Radon transform on circles directly on the plane of the original 2D signal is not invertible, the Radon transform has to be done in higher dimensional 3D conformal space where circles correspond to planes.

requires all integrals on all 2D lines  $(t, \theta)$  to reconstruct the original signal at a certain point and is therefore called a global transform. This interesting fact turns out from the following 3D inverse Radon transform at the origin of the local coordinate system

$$\mathcal{R}^{-1}\{c_r\}(\mathbf{0}) = -\frac{1}{8\pi^2} \int_{\theta=0}^{2\pi} \int_{\varphi=0}^{\pi} \frac{\partial^2}{\partial t^2} c_r(t, \theta, \varphi)|_{t=0} d\varphi d\theta . \quad (3.14)$$

Therefore, the local features of i1D and i2D signals can be determined by the conformal monogenic signal at the origin of the 2D signal without knowledge of the whole Radon space. Hence, the relation of the Radon to the generalized Hilbert transform is essential to interpret the generalized Hilbert transform in conformal space.

## 3.5. Local Signal Interpretation

Analogously to the interpretation of the monogenic signal in [74], the parameters of the plane within the 3D Radon space determine the local features of the curved i2D signal, see Figure (3.4). The norm of the 3D generalized Hilbert transform in conformal space reads

$$\|\mathcal{H}\{c\}(\mathbf{0})\| = \sqrt{c_x^2 + c_y^2 + c_z^2} . \quad (3.15)$$

The curvature, see Figure (3.9), can be measured by the parameter  $\varphi$  of the 3D Radon space,

$$\varphi = \arctan \frac{\sqrt{c_x^2 + c_y^2}}{c_z} . \quad (3.16)$$

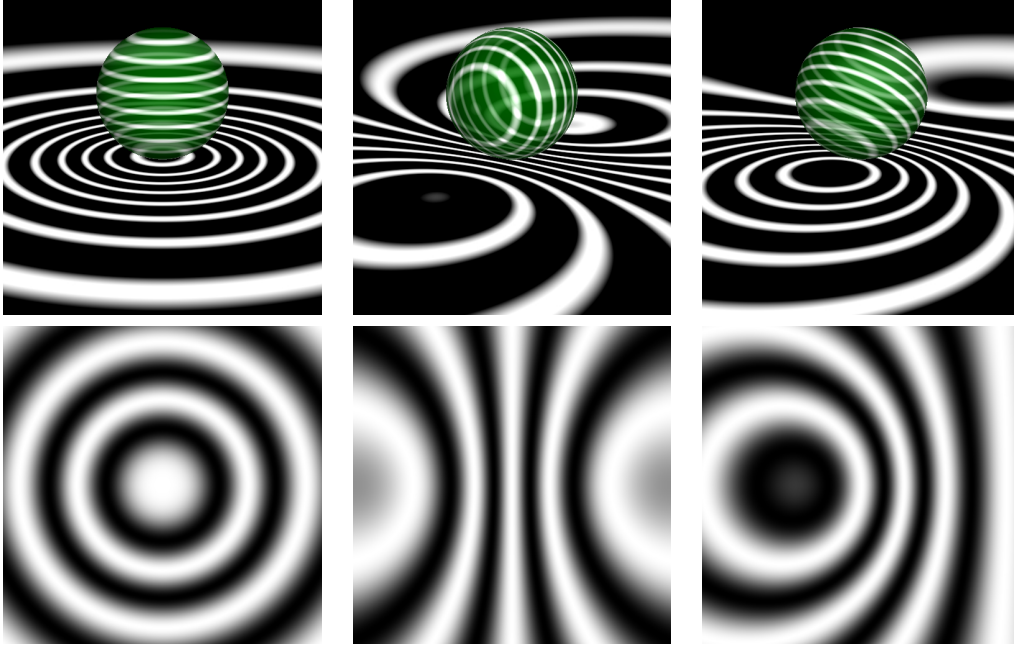


Figure 3.6.: Illustration by O. Fleischmann of the conformal mapping of 2D signals to the 3D conformal space.

It will be shown in Section (3.5.1) that  $\varphi$  corresponds to the isophote curvature  $\kappa$  [43] known from differential geometry and also used in [60] and [59],

$$\kappa = \frac{-\frac{\partial^2}{\partial x^2} f \frac{\partial}{\partial y} f^2 + 2 \frac{\partial}{\partial x} f \frac{\partial}{\partial y} f \frac{\partial^2}{\partial xy} f - \frac{\partial^2}{\partial y^2} f \frac{\partial}{\partial x} f^2}{\left( \frac{\partial}{\partial x} f^2 + \frac{\partial}{\partial y} f^2 \right)^{\frac{3}{2}}} . \quad (3.17)$$

Besides, the curvature of the conformal monogenic signal naturally indicates the intrinsic dimension of the signal. The parameter  $\theta$  will be interpreted as the orientation  $\theta \in [0, \pi)$  in i1D case and naturally deploys to direction  $\theta \in [0, 2\pi)$  for the i2D case

$$\theta = \text{atan2}(c_y, c_x) . \quad (3.18)$$

The amplitude of the signal is defined by

$$a = \sqrt{c_p^2 + \|\mathcal{H}\{c\}(\mathbf{0})\|^2} . \quad (3.19)$$

The phase of curved 2D signals is defined by

$$\phi = \text{atan2}(\|\mathcal{H}\{c\}(\mathbf{0})\|, c_p) . \quad (3.20)$$

In both cases of intrinsic dimension the phase indicates a measure of parity symmetry. Note that all proofs are analogous to those for the 2D monogenic signal shown in [74].

### 3. The Conformal Monogenic Signal

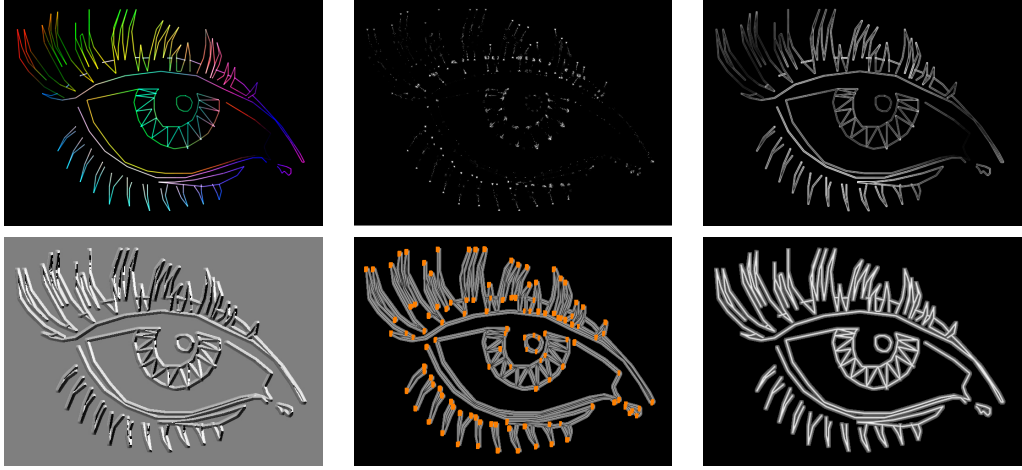


Figure 3.7.: Top row from left to right: Original signal, isophote curvature [43], and Sobel detector output. Bottom row from left to right: Conformal monogenic signal direction, curvature, and phase. Note the observable illumination invariance of the conformal curvature and phase. Convolution mask size:  $7 \times 7$  pixels.

*Proof:* Due to Equation (3.11) the explicit formulation of the local curved signal model in Poisson scale space in Equation (3.6) reads

$$\begin{bmatrix} c_p \\ c_x \\ c_y \\ c_z \end{bmatrix} = a \begin{bmatrix} \cos \phi \\ \sin \phi \sin \varphi \cos \theta \\ \sin \phi \sin \varphi \sin \theta \\ \sin \phi \cos \varphi \end{bmatrix} \quad (3.21)$$

which can easily be solved for the local amplitude  $a$ , the phase  $\phi$ , the orientation/direction  $\theta$  and for the - to the curvature corresponding - parameter  $\varphi$ , see Figures (3.7) and (3.8).  $\square$

#### 3.5.1. Local Signal Curvature

In this section it will be shown that the conformal monogenic signal determines the exact local curvature of all curved 2D signals which can be locally approximated by circles. Let  $f \in L^2(\Omega, \mathbb{R})$  with  $\Omega \subseteq \mathbb{R}^2$  be the 2D signal in Poisson scale space, i.e.

$$f = (p_s * f)(z) \quad (3.22)$$

with  $p_s$  as the Poisson kernel in the spatial domain for a certain scale parameter  $s > 0$ . Let

$$\gamma(t) = [\rho(\cos \theta + \cos t), \rho(\sin \theta + \sin t)]^T, \quad t \in [0, 2\pi) \quad (3.23)$$

be a parametrization of a circle in the 2D plane touching the origin  $(0, 0) \in \mathbb{R}^2$  with radius  $\rho$  and tangential orientation  $\theta$ . This circle will be the model for the osculating

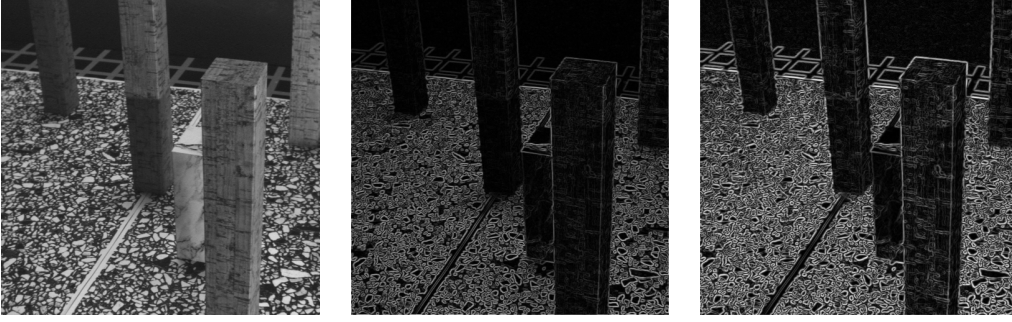


Figure 3.8.: From left to right: Original marble image, Sobel detector output, and conformal monogenic signal curvature. The difference between the Sobel output and the conformal monogenic signal curvature can be seen clearly. Convolution mask size:  $7 \times 7$  pixels.

circle touching the isophote curve of the 2D signal  $f$  at the origin  $(0, 0) \in \mathbb{R}^2$  of the local coordinate system for each test point. Therefore, it follows that

$$f(\gamma(t_1)) = f(\gamma(t_2)) \quad \forall t_1, t_2 \in [0, 2\pi) . \quad (3.24)$$

Define

$$\gamma_S(t) = \mathcal{C}(\gamma(t)) \quad (3.25)$$

as the inverse stereographic projection of  $\gamma$  to the sphere

$$\mathbb{S}^2(m_S, \rho_S) = \{v \in \mathbb{R}^3 : \|v - m_S\| = \rho_S\} \quad (3.26)$$

with the center  $m_S = (0, 0, \frac{1}{2})^T$  and the radius  $\rho_S = \frac{1}{2}$ . Furthermore, define

$$f_S(\gamma_S(t)) = f(\mathcal{C}^{-1}(\gamma_S(t))) \quad (3.27)$$

where  $\mathcal{C}^{-1}$  is the stereographic projection. The conjugate Poisson kernel reads

$$q = (q_x, q_y, q_z)^T = (h_3 * p_s)(z) \quad (3.28)$$

with the Poisson kernel  $p_s$  and the generalized Hilbert kernel  $h_n$  in the spatial domain of dimension  $n \in \mathbb{N}$ .

**Theorem 3.5.1.** *The curvature  $\kappa$  of the osculating circle described by the parameterized curve  $\gamma$  reads*

$$\kappa = \frac{2 \mathcal{H}_z\{f_S\}(\mathbf{0})}{\sqrt{[\mathcal{H}_x\{f_S\}(\mathbf{0})]^2 + [\mathcal{H}_y\{f_S\}(\mathbf{0})]^2}} = \frac{2(q_z * f_S)(\mathbf{0})}{\sqrt{[(q_x * f_S)(\mathbf{0})]^2 + [(q_y * f_S)(\mathbf{0})]^2}} . \quad (3.29)$$

with  $\mathbf{0} = (0, 0, 0)$ .

### 3. The Conformal Monogenic Signal

*Proof:* Consider the convolution

$$\begin{aligned}
\mathcal{H}\{f_S\}(\mathbf{0}) &= (q * f_S)(\mathbf{0}) \\
&= \int_{z \in \mathbb{R}_+^3} q(\mathbf{0} - z) f_S(z) dz \\
&= \int_{z \in \mathbb{R}_+^3} q(-z) f_S(z) dz \\
&= \frac{2}{A_4} \int_{z \in \mathbb{R}_+^3} \left[ \frac{z}{\|z\|^4} * p_s(z) \right] f_S(z) dz .
\end{aligned} \tag{3.30}$$

Since the values of  $f_S(z)$  will only be nonzero for  $z \in \mathbb{S}^2(m_S, \rho_S)$ , the integration can be restricted to

$$\int_{z \in \mathbb{R}_+^3} q(z) f_S(z) dz = \int_{z \in \mathbb{S}^2(m_S, \rho_S)} q(z) f_S(z) dz . \tag{3.31}$$

Furthermore,  $f_S(x)$  is only nonzero for

$$M = \{\gamma_S(t) : t \in [0, 2\pi)\} \tag{3.32}$$

which describes the circle projected onto the sphere. Now let  $\mathbb{S}^2(m, \rho)$  be the sphere whose intersection with  $\mathbb{S}^2(m_S, \rho_S)$  results in  $M$ . Then the set  $M$  is a circle on the surface of  $\mathbb{S}^2(m_S, \rho_S)$  and  $\mathbb{S}^2(m, \rho)$ . The integration over  $\mathbb{S}^2(m, \rho)$  and  $\mathbb{S}^2(m_S, \rho_S)$  will be the same

$$\int_{z \in \mathbb{S}^2(m_S, \rho_S)} q(z) f_S(z) dz = \int_{z \in \mathbb{S}^2(m, \rho)} q(z) f_S(z) dz . \tag{3.33}$$

According to the results from harmonic analysis [2] the convolution of a function in  $\mathbb{R}^n$  with the Poisson kernel  $p$  in the upper half space  $\mathbb{R}_+^{n+1}$  results in a harmonic function in  $\mathbb{R}_+^{n+1}$ . Therefore,  $q$  is harmonic in  $\mathbb{R}_+^{3+1}$ . Using the mean value theorem for harmonic functions it follows that

$$\int_{z \in \mathbb{S}^2(m, \rho)} q(z) dz = k Q(m) \tag{3.34}$$

with the components of  $Q(m)$  written in spherical coordinates

$$\begin{bmatrix} Q_x \\ Q_y \\ Q_z \end{bmatrix} (m) = \frac{1}{(m_x^2 + m_y^2 + m_z^2 + s^2)^2} \begin{bmatrix} \sin \varphi_m \cos \theta_m \\ \sin \varphi_m \sin \theta_m \\ \cos \varphi_m \end{bmatrix} \tag{3.35}$$

with  $m = (m_x, m_y, m_z)$  and  $s > 0$  as the scale space parameter. Since  $f_S$  is the signal model for the isophote curve of a signal in the plane, it is a curve consisting of constant values. Therefore,  $f_S(z)$  will be constant for all  $z \in M$  which results in

$$\int_M q(z) f_S(z) dz = c \int_M q(z) dz = c k Q(m) . \tag{3.36}$$



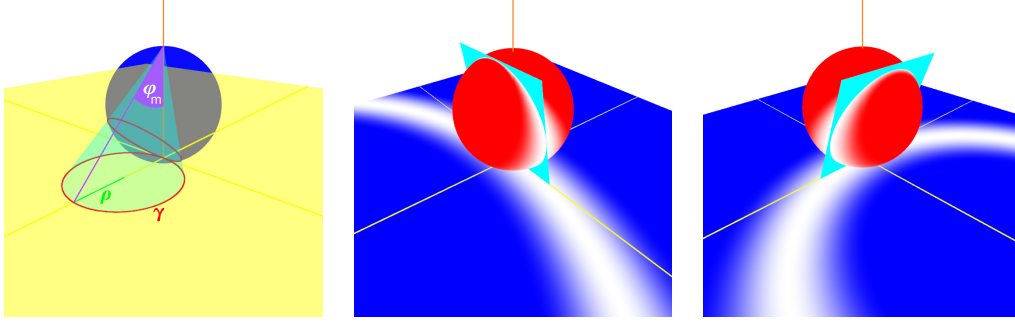


Figure 3.9.: From left to right: The first figure illustrates the circle described by  $\gamma$  which is projected on  $\mathbb{S}^2(m_S, \rho_S)$ . It can be seen that  $\frac{1}{\kappa} = \rho = \frac{1}{2} \tan \varphi_m$ . The second and third figure illustrate two signals with different local curvature which corresponds to the parameter  $\varphi$  of the hyper-plane. This hyper-plane will be delivered by the generalized Hilbert transform and encodes amplitude, phase, direction and curvature.

With Equation (3.29) it is now possible to determine  $\frac{\sin \varphi_m}{\cos \varphi_m}$ . Figure (3.9) illustrates that this is exactly  $\frac{\rho}{\rho_S}$ . Since  $\rho_S = \frac{1}{2}$  it follows that the radius of the local curvature can be determined by

$$\frac{1}{\kappa} = \rho = \frac{\sin \varphi_m}{2 \cos \varphi_m} = \frac{\sqrt{Q_x^2(m) + Q_y^2(m)}}{2 Q_z(m)}. \quad (3.37) \quad \square$$

### 3.5.2. Experimental Results

On synthetic signals with known ground truth the average error of the feature extraction converges to zero with increasing refinement of the convolution mask size. Under the presence of noise the conformal monogenic signal curvature performs more robust than e.g. the gradient based Sobel detector, see Figure (3.10). The curvature feature delivered by the conformal monogenic signal performs better in dense optical flow applications with an average angular error (AAE) of  $1.99^\circ$  compared to [77] (with  $AAE = 2.67^\circ$ ) on the cloudy Yosemite sequence, see Figure (3.10).

## 3.6. The 3D Conformal Monogenic Signal

The conformal monogenic signal can be extended to any signal dimension analogously to the monogenic signal [64, 67, 72, 69]. The generalized Hilbert transform [7] in Euclidean space reads

$$h_n(z) = \frac{2}{A_{n+1}} \frac{z}{\|z\|^{n+1}}, \quad z \in \mathbb{R}^n, \quad n \in \mathbb{N} \setminus \{1\}. \quad (3.38)$$

### 3. The Conformal Monogenic Signal

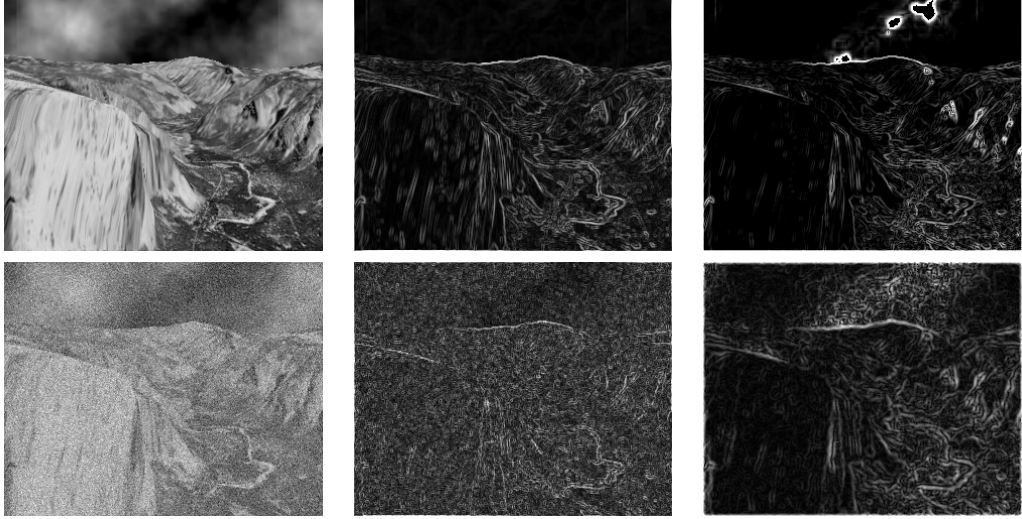


Figure 3.10.: Top row from left to right: Original Yosemite image, Sobel detector output and conformal monogenic signal curvature which delivers much more structural information (see cloudy sky). Bottom row from left to right: Noise degraded image (SNR=10dB), blurred Sobel output and conformal monogenic signal curvature. Convolution mask size:  $7 \times 7$  pixels.

The concatenation of the Hilbert kernel and the Poisson kernel to one unified kernel, called the conjugate kernel, reads

$$q_n = (h_n * p_n(\cdot, s))(z) = \frac{2}{A_{n+1}} \frac{z}{(s^2 + \|z\|^2)^{(n+1)/2}}. \quad (3.39)$$

In case of visual motion analysis three dimensional isotropic quadrature filters are needed [41, 29].

The conformal monogenic signal of a 3D signal  $f \in L^2(\Omega, \mathbb{R})$  with  $\Omega \subset \mathbb{R}^3$  delivers amplitude, 3D orientation, phase and curvature. For image sequences (3D signals) the concept of planes in 3D Radon space becomes the more abstract concept of hyper-planes in 4D Radon space. These 4D hyper-planes determine 3D spheres on the 4D hyper-sphere in 4D conformal space. Since 3D planes and 3D spheres of the three-dimensional signal domain are mapped to 3D spheres on the 4D hyper-sphere, the integration on these 3D spheres determines points in the 4D Radon space, see Figures (3.11) and (3.5).

The general inverse stereographic projection for any dimension  $n \in \mathbb{N}$  which maps the Euclidian space  $\mathbb{R}^n$  to the conformal space  $\mathbb{R}^{n+1}$  reads

$$\mathcal{S}^{-1}(x_1, x_2, \dots, x_n) = \frac{1}{1 + \sum_{\nu=1}^n x_\nu^2} \begin{bmatrix} x_1 \\ x_2 \\ \vdots \\ x_n \\ \sum_{\nu=1}^n x_\nu^2 \end{bmatrix}. \quad (3.40)$$

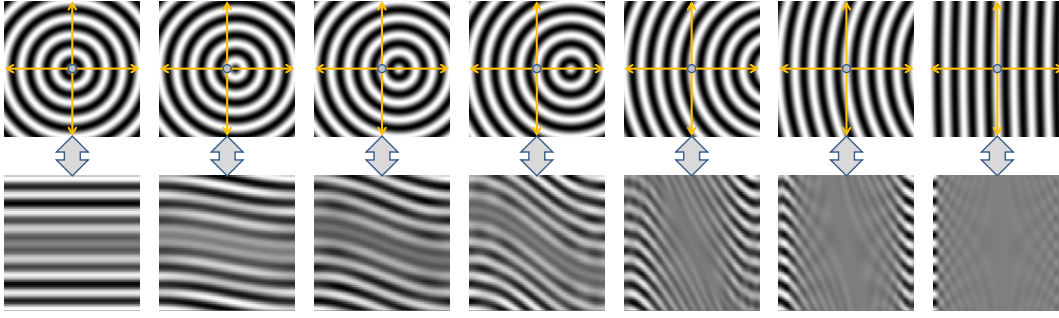


Figure 3.11.: From left to right: signal with varying curvature in the spatial domain (top row) and in the corresponding 2D Radon space (bottom row). Obviously the 2D Radon space is too flat for analyzing and parameterizing the orientation and curvature of signals. Therefore the dimension of the 2D Radon space must be extended to 3D. This is the idea of the conformal signal.

The inverse stereographic projection maps the Euclidian space  $\mathbb{R}^n$  to the hyper-sphere in  $\mathbb{R}^{n+1}$  with radius  $\frac{1}{2}$  and the south pole of the hyper-sphere touching the origin  $\mathbf{0} \in \mathbb{R}^n$  of the Euclidian space  $\mathbb{R}^n$  and the north pole of the hyper-sphere with coordinates  $(\mathbf{0}, 1) \in \mathbb{R}^{n+1}$ . This projection is conformal and can be inverted by the general formula

$$\mathcal{S}(\xi_1, \xi_2, \dots, \xi_n, \xi_{n+1}) = \frac{1}{1 - \xi_{n+1}} \begin{bmatrix} \xi_1 \\ \xi_2 \\ \vdots \\ \xi_n \end{bmatrix}. \quad (3.41)$$

For the signal dimension  $n = 3$  the inverse stereographic projection  $\mathcal{S}^{-1}$  known from complex analysis [30] maps the 3D signal domain to the hyper-sphere. This mapping has the property that the origin of the 3D signal domain will be mapped to the south pole  $\mathbf{0}$  of the hyper-sphere and both  $-\infty, +\infty$  will be mapped to the north pole  $(0, 0, 0, 1)$  of the hyper-sphere. 3D planes and spheres of the 3D signal domain will be mapped to spheres on the hyper-sphere and can be determined uniquely by hyper-planes in 4D Radon space. The integration on these hyper-planes corresponds to points  $(t, \theta_1, \theta_2, \varphi)$  in the 4D Radon space. Since the signal domain  $\Omega \subset \mathbb{R}^3$  is bounded, not the whole hyper-sphere is covered by the original signal. Anyway, all hyper-planes corresponding to spheres on the hyper-sphere remain unchanged. That is the reason why the conformal signal models 3D planes and all kinds of curved 3D planes which can be locally approximated by spheres. To provide more degrees of freedom to the generalized Hilbert transform, the original three-dimensional signal will be embedded in an applicable subspace of the conformal space by the so called conformal signal  $c : \mathbb{R}^4 \mapsto \mathbb{R}$  of the original 3D signal  $f$

$$c(\xi) = \begin{cases} f(\mathcal{S}(\xi_1, \xi_2, \xi_3, \xi_4)^T) & , \quad \sum_{\nu=1}^3 \xi_\nu^2 + (\xi_4 - \frac{1}{2})^2 = (\frac{1}{2})^2 \\ 0 & , \quad \text{else} \end{cases} \quad (3.42)$$

by which the even signal part  $c^e = (c * p_4)(\mathbf{0}; s)$  can be defined. Thus, the 4D generalized Hilbert transform can be applied to all points on the hyper-sphere. The center

### 3. The Conformal Monogenic Signal

of convolution in the spatial domain is the south pole where the origin of the 3D signal domain meets the hyper-sphere. At this point the generalized Hilbert transform will be evaluated in the spatial domain by convolution for each test point

$$c^o = \begin{bmatrix} c_1^o \\ c_2^o \\ c_3^o \\ c_4^o \end{bmatrix} = (q_4 * c)(\mathbf{0}; s) = \frac{2}{A_5} \int_{z \in \mathbb{R}^4} \frac{z}{(s^2 + \|x\|^2)^{5/2}} c(z - \mathbf{0}) dz . \quad (3.43)$$

The conformal signal for 3D signals is defined by the even part and the four odd parts of the 4D Hilbert transform. Note that the coordinates are relative to the local coordinate system for each test point of the original 3D signal and  $\mathbf{0} = (0, 0, 0, 0)$  are the corresponding relative coordinates in conformal space, i.e. this is no restriction. The Hilbert transform of the 3D signal embedded in the conformal space can also be written in terms of the 4D Radon transform and its inverse

$$c^o = \mathcal{R}^{-1} \{ (t, \theta_1, \theta_2, \varphi) \mapsto v_4 (h * \mathcal{R} \{ (c * p_4(\cdot, s)) (z) \} (\cdot, \theta_1, \theta_2, \varphi)) (t) \} (\mathbf{0}) \quad (3.44)$$

with

$$v_4 = \begin{bmatrix} \cos \varphi \sin \theta_1 \sin \theta_2 \\ \sin \varphi \sin \theta_1 \sin \theta_2 \\ \cos \theta_1 \sin \theta_2 \\ \cos \theta_2 \end{bmatrix} . \quad (3.45)$$

This representation of the Hilbert transform is essential for the subsequent interpretation of the conformal signal. Remember that without loss of generality the signal will be analyzed at the origin of the local coordinate system of the test point of local interest. Compared to the monogenic signal the conformal signal is based on a Hilbert transformation in conformal space. Analogously to the interpretation of the monogenic signal in [74], the parameters of the hyper-plane within the 4D Radon space determine the local features of the curved 3D signal. The conformal signal can be called the generalized monogenic signal for 3D signals, because the special case of planes in the original 3D signal can be considered as spheres with zero curvature. These planes are mapped to spheres passing through the north pole in conformal space. The 3D curvature corresponds to the parameter  $\varphi$  of the 4D Radon space,

$$\varphi = \arctan \frac{c_2^o}{c_1^o} . \quad (3.46)$$

Besides, the curvature of the conformal signal naturally indicates the intrinsic dimension of the signal. The parameters  $(\theta_1, \theta_2)$  will be interpreted as the orientation of the signal in the original 3D space

$$\theta_1 = \arcsin \frac{\sqrt{[c_1^o]^2 + [c_2^o]^2}}{c_4^o} , \quad (3.47)$$

$$\theta_2 = \arctan \frac{\sqrt{[c_1^o]^2 + [c_2^o]^2 + [c_3^o]^2}}{c_4^o} . \quad (3.48)$$

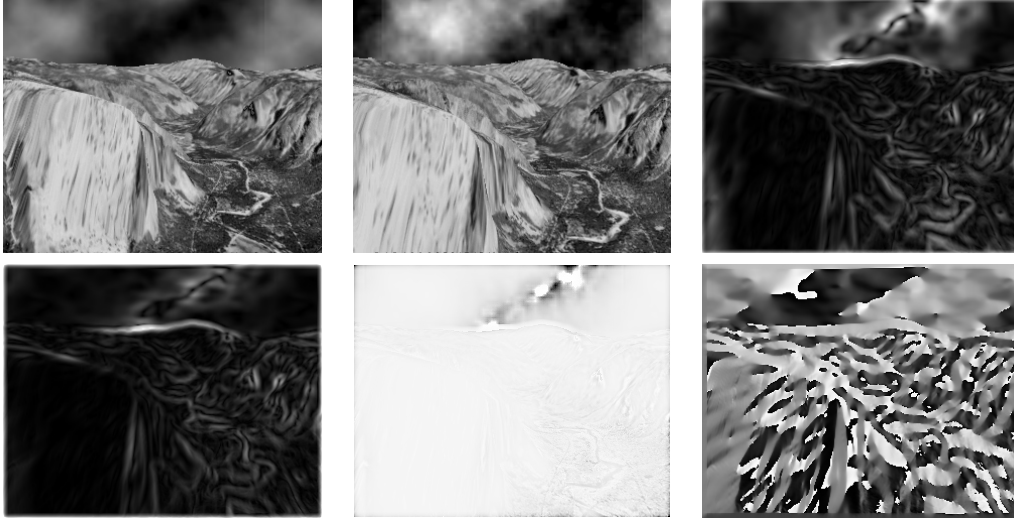


Figure 3.12.: The 3D conformal monogenic signal delivers four local features which can be used for image sequence analysis such as optical flow and motion analysis. Top row from left to right: First picture, last picture of the original Yosemite image sequence, and local curvature. Second row from left to right: Local phase, and the two parts of the local orientation information. 3D convolution mask size:  $5 \times 5 \times 5$  pixels.

The amplitude and phase are defined by

$$a = \sqrt{[c^e]^2 + \|c^o\|^2}, \quad (3.49)$$

$$\phi = \arctan \frac{\|c^o\|}{c^e}, \quad (3.50)$$

see Figures (3.12) and (3.13). In all different intrinsic dimensions the phase indicates a measure of parity symmetry. Note that all proofs are analogous to those for the monogenic signal shown in [74].

### 3. The Conformal Monogenic Signal

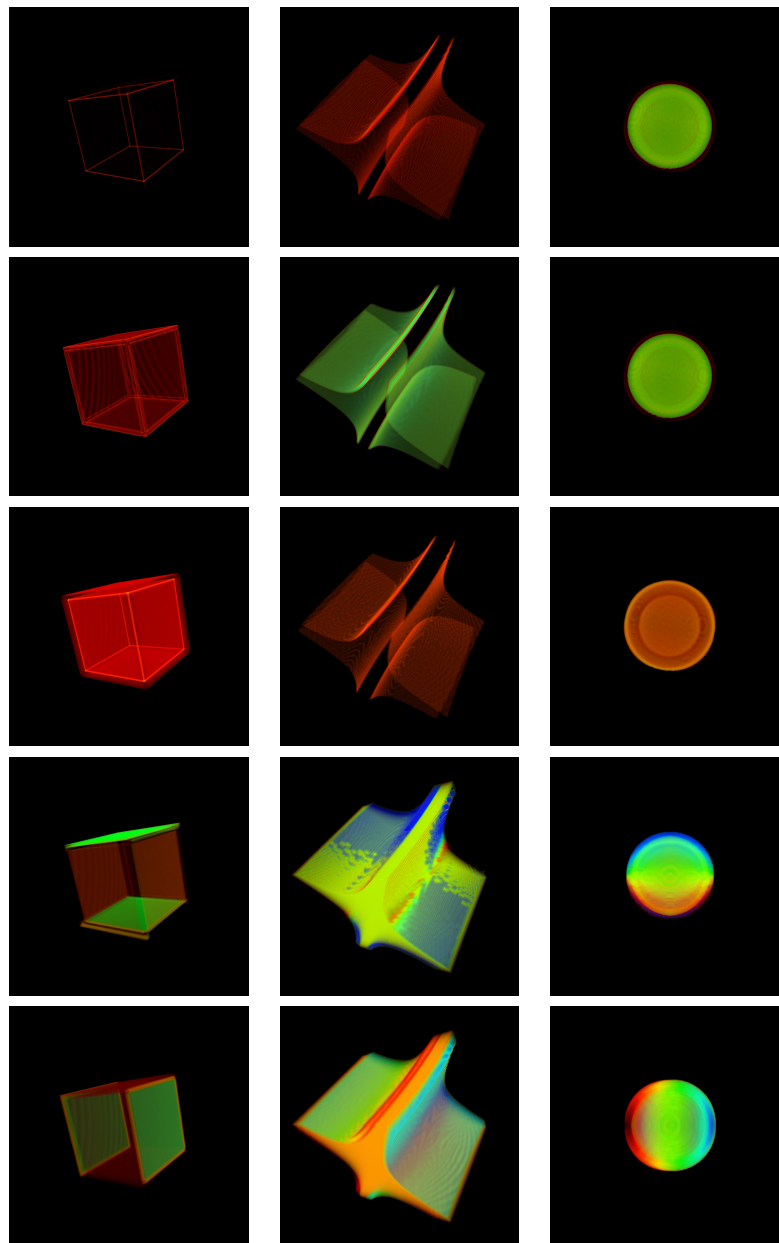


Figure 3.13.: Illustration by O. Fleischmann [24] of the local features of the 3D conformal monogenic signal from top to bottom: amplitude, phase, curvature and the two orientations.

## 4. The Isotropic 2D Analytic Signal

The monogenic signal can be used to analyze i1D signals such as lines and edges. Unfortunately, the monogenic signal cannot distinguish between i1D and i2D signals. The most interesting class of signals is the set of i2D signals. In general i2D signals can only be described by an infinite number of superimposed i1D signals. In this chapter the isotropic properties of the monogenic signal will be conserved for a subclass of i2D signals by introducing the isotropic 2D analytic signal. Furthermore, we want to show the relation of the signal representation to geometric spaces [71]. The 2D monogenic signal can be represented in 3D Euclidean space. The results of this thesis show that the generalizations of the monogenic signal can be represented in subspaces of the homogeneous space and more general in conformal spaces. Therefore, a signal model must be defined. This model subsumes all i1D signals and also a subclass of i2D signal structures (such as corners and junctions in the case of image signals). The basic signal model of the isotropic 2D analytic signal reads

$$\mathcal{P}_s\{f\}(z) = \sum_{i=1}^2 a \cos(x \cos \theta_i + y \sin \theta_i + \phi) \quad (4.1)$$

which will be generalized in Chapter 5. The resulting local signal model at the origin  $z = (x, y)$  of the test point is given by

$$f_p = 2a \cos \phi = \mathcal{P}_s\{f\}(z) . \quad (4.2)$$

Note that equal amplitudes and phases are assumed for both i1D signals. In case of

$$\theta_1 \pmod{\pi} = \theta_2 \pmod{\pi} \quad (4.3)$$

this is the ordinary i1D signal model. The i1D signal model has three unknown structure features (phase, amplitude and orientation) and the monogenic signal vector consists of three signal components

$$[f_p, f_x, f_y]^T \in \mathbb{R}^3 \quad (4.4)$$

to solve the system of equations. Since our restricted i2D signal model consists of four unknowns, more signal components are required. Therefore, the next step will be the exploitation of the components of the second order Hilbert transform

$$[\mathcal{Q}_{xx}^{(2)}, \mathcal{Q}_{xy}^{(2)}, \mathcal{Q}_{yy}^{(2)}]^T , \quad (4.5)$$

which are related to the entries of the well known Hessian matrix. Motivated by the first and second order derivatives of the Weingarten map

$$\left[ \frac{\partial}{\partial x}, \frac{\partial}{\partial y}, \frac{\partial^2}{\partial x^2}, \frac{\partial^2}{\partial xy}, \frac{\partial^2}{\partial y^2} \right]^T \quad (4.6)$$

#### 4. The Isotropic 2D Analytic Signal

known from differential geometry [14], here the first and second order Hilbert transform operators will be used for signal analysis

$$[\mathcal{Q}_x^{(1)}, \mathcal{Q}_y^{(1)}, \mathcal{Q}_{xx}^{(2)}, \mathcal{Q}_{xy}^{(2)}, \mathcal{Q}_{yy}^{(2)}]^T . \quad (4.7)$$

Analogously to the pure i1D signal model, the first order Hilbert transform of the i1D/i2D signal model reads

$$\begin{bmatrix} f_x \\ f_y \end{bmatrix} = \sum_{i=1}^2 a \sin \phi \begin{bmatrix} \cos \theta_i \\ \sin \theta_i \end{bmatrix} \quad (4.8)$$

at the origin  $z = (x, y) \in \mathbb{R}^2$  of the local coordinate system.

### 4.1. Second Order Hilbert Transform in Radon Space

Same as shown for the first order Hilbert transform the second order Hilbert transform of the i1D / i2D signal can also be evaluated by the relation of the Radon transform to the Hilbert transform [17] by concatenation of two first order Hilbert transforms

$$\begin{bmatrix} f_{xx} \\ f_{xy} \\ f_{yy} \end{bmatrix} = -\mathcal{R}^{-1} \left\{ (t, \theta) \mapsto \begin{bmatrix} \cos^2 \theta \\ \sin \theta \cos \theta \\ \sin^2 \theta \end{bmatrix} f_r(t, \theta, s) \right\} (z) \quad (4.9)$$

since  $(h * h * g)(t) = -g(t)$ , see Figure (4.1). The second order Hilbert transform of the assumed signal model results in

$$\begin{bmatrix} f_{xx} \\ f_{xy} \\ f_{yy} \end{bmatrix} = \sum_{i=1}^2 a \cos \phi \begin{bmatrix} \cos^2 \theta_i \\ \frac{1}{2} \sin(2\theta_i) \\ \sin^2 \theta_i \end{bmatrix} . \quad (4.10)$$

The first result is the reconstruction of the Poisson filtered original signal

$$f_{xx} + f_{yy} = 2a \cos \phi = f_p . \quad (4.11)$$

With these results the system of equations has to be solved and the four unknown local features such as amplitude, orientation, phase and apex angle have to be derived.

### 4.2. Third Order Hilbert Transform in Radon Space

Analogously to the second order Hilbert transform of the signal  $f$  the third order Hilbert transform expressed in Radon space reads

$$\begin{bmatrix} f_{xxx} \\ f_{xxy} \\ f_{xyy} \\ f_{yyy} \end{bmatrix} = -\mathcal{R}^{-1} \left\{ (t, \theta) \mapsto \begin{bmatrix} \cos^3 \theta \\ \cos^2 \theta \sin \theta \\ \cos \theta \sin^2 \theta \\ \sin^3 \theta \end{bmatrix} (h * f_r(\cdot, \theta, s))(t) \right\} (z) \quad (4.12)$$



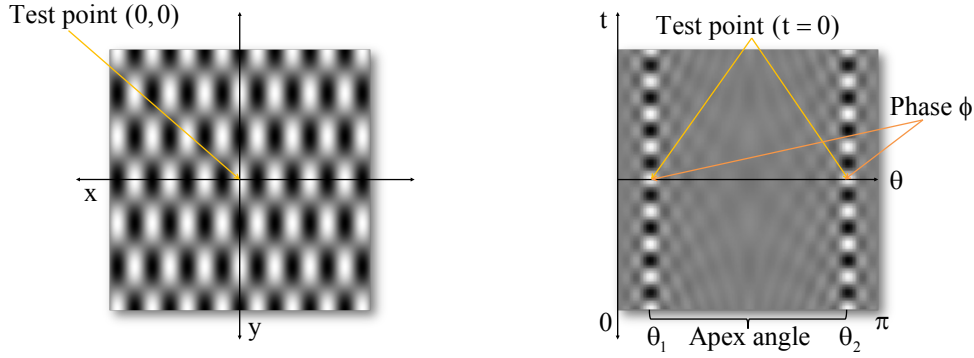


Figure 4.1.: Left figure: The i2D checkerboard signal in the spatial domain with orientations  $\theta_1, \theta_2$  and local phase  $\phi = 0$  at the test point  $z$  at the origin of the local coordinate system. Right figure: The i2D signal is separated into two independent i1D signals with different orientations and same phase at  $t = 0$  in Radon space.

since  $(h * h * h)(t) = -h(t)$ . We use the abbreviation  $f_r(t, \theta, s) = \mathcal{R}\{\mathcal{P}_s\{f\}\}(t, \theta)$  for the Radon transformed signal in Poisson scale space. For the given signal model the third order Hilbert transform results in the following system of equations

$$\begin{bmatrix} f_{xxx} \\ f_{xxy} \\ f_{xyy} \\ f_{yyy} \end{bmatrix} = \sum_{i=1}^2 a \sin \phi \begin{bmatrix} \cos^3 \theta_i \\ \cos^2 \theta_i \sin \theta_i \\ \cos \theta_i \sin^2 \theta_i \\ \sin^3 \theta_i \end{bmatrix} \quad (4.13)$$

with the first obvious result, namely, that the first order Hilbert transform can be reconstructed by

$$f_{xxx} + f_{xyy} = f_x, \quad (4.14)$$

$$f_{xxy} + f_{yyy} = f_y. \quad (4.15)$$

### 4.3. Algebraic Signal Representations

In this section we will show how to map signal representations in tensor form to so called multi-vectors for geometric interpretation. For complete signal analysis problems the original signal has to be extended by the generalized Hilbert transforms. The resulting signal can be complex valued, quaternionic valued or tensor valued. In case of generalized Hilbert transforms of higher orders, the extended signal is tensor-valued or matrix-valued with multi-vector-valued entries. To analyze such signals geometrically, the matrix or tensor forms will be mapped to a multi-vector. Such multi-vectors can be interpreted in a geometric way. The objective of this section is to introduce an isomorphic mapping

#### 4. The Isotropic 2D Analytic Signal

from tensor and matrix structures to multi-vectors.

The structures of matrix algebra and geometric algebra [44] are completely compatible and in many ways complimentary, each having their own advantages and disadvantages. In this section we present a detailed study of the hybrid  $2 \times 2$  matrix geometric algebra (HMGA) [53]

$$M(2, \mathbb{R}_3) = \left\{ \begin{bmatrix} M_{11} & M_{12} \\ M_{21} & M_{22} \end{bmatrix} : M_{\nu\mu} \in \mathbb{R}_3 \right\} \quad (4.16)$$

with elements of the 8-dimensional geometric algebra  $\mathbb{R}_3$  of Euclidean space. The resulting hybrid structure, which is isomorphic to the geometric algebra  $\mathbb{R}_{4,1}$  of de Sitter space, combines the simplicity of  $2 \times 2$  matrices and the clear geometric interpretation of the elements of  $\mathbb{R}_{4,1}$ , which will be used in this thesis for signal analysis.

$$M(2, \mathbb{R}_3) \cong \mathbb{R}_{4,1} \quad (4.17)$$

It is well known that the geometric algebra  $\mathbb{R}_{4,1}$  contains the 3-dimensional affine, projective and conformal spaces of Möbius transformations, together with the 3-dimensional horosphere which has attracted the attention of computer scientists and engineers as well as mathematicians and physicists.

#### 4.3.1. Geometric Algebra of Euclidean Space

Since only finite-dimensional geometric algebras are used in this section, the following axioms are specialized to this case. Let  $\mathbb{R}^{p,q}$  denote a  $p + q$ -dimensional vector space over the field  $(\mathbb{R}, +, \cdot)$ . Furthermore, let a commutative scalar product be defined as

$$* : \mathbb{R}^{p,q} \times \mathbb{R}^{p,q} \mapsto \mathbb{R} \quad (4.18)$$

That is, for  $a, b \in \mathbb{R}^{p,q}$ ,

$$a * b = b * a \in \mathbb{R} \quad (4.19)$$

The canonical basis of  $\mathbb{R}^{p,q}$ , denoted by  $\bar{\mathbb{R}}^{p,q}$ , is defined as the totally ordered set

$$\bar{\mathbb{R}}^{p,q} = \{\mathbf{e}_1, \dots, \mathbf{e}_p, \mathbf{e}_{p+1}, \dots, \mathbf{e}_{p+q}\} \subset \mathbb{R}^{p,q} \quad (4.20)$$

where the  $\{\mathbf{e}_\nu\}$  have the property

$$\mathbf{e}_\nu * \mathbf{e}_\mu = \begin{cases} 1, & 1 \leq \nu = \mu \leq p, \\ -1, & p < \nu = \mu \leq p + q, \\ 0, & \nu \neq \mu. \end{cases} \quad (4.21)$$

The combination of a vector space with a scalar product  $*$  is called a quadratic space. Quadratic spaces form the basis for the construction of geometric algebras. While the quadratic space  $(\mathbb{R}^{p,q}, *)$  plays a central role in applications, geometric algebras can be constructed over any type of quadratic spaces, e.g. over Hilbert spaces. It is therefore possible to construct a geometric algebra over a finite Fourier basis.

### Axioms

Let  $\mathbb{A}(\mathbb{R}^{p,q})$  denote the associative algebra over the quadratic space  $(\mathbb{R}^{p,q}, *)$  and let  $\circ$  denote the algebraic product. Note that the field  $\mathbb{R}$  and the vector space  $\mathbb{R}^{p,q}$  can both be regarded as subspaces of  $\mathbb{A}(\mathbb{R}^{p,q})$ . The algebra  $\mathbb{A}(\mathbb{R}^{p,q})$  is said to be a geometric algebra if for  $a \in \mathbb{R}^{p,q}$ ,

$$a \circ a = a * a. \quad (4.22)$$

The geometric algebra over  $\mathbb{R}^{p,q}$  is denoted by  $\mathbb{R}(\mathbb{R}^{p,q})$  or simply  $\mathbb{R}_{p,q}$  and the algebra product is called the Clifford or geometric product. Although the geometric product is denoted here by  $\circ$ , it can also be abbreviated by juxtaposition. In the following, all axioms of a geometric algebra will be given explicitly. First of all, the elements of the geometric algebra  $\mathbb{R}_{p,q}$ , which are called multi-vectors or Clifford numbers, satisfy the axioms of a vector space over the field  $\mathbb{R}$  or  $\mathbb{C}$ .

The following two operations exist in  $\mathbb{R}_{p,q}$ :

1. Addition of two multi-vectors:

$$a + b \in \mathbb{R}_{p,q} \quad \forall a, b \in \mathbb{R}_{p,q} \quad (4.23)$$

2. Scalar multiplication:

$$\alpha a \in \mathbb{R}_{p,q} \quad \forall \alpha \in \mathbb{R}, \forall a \in \mathbb{R}_{p,q} \quad (4.24)$$

which is called the  $\alpha$ -multiple of  $a$ .

The vector space axioms:

Let  $a, b, c \in \mathbb{R}_{p,q}$  and  $\alpha, \beta \in \mathbb{R}$

1. Associativity:

$$(a + b) + c = a + (b + c) \quad \forall a, b, c \in \mathbb{R}_{p,q} \quad (4.25)$$

2. Commutativity:

$$a + b = b + a \quad \forall a, b \in \mathbb{R}_{p,q} \quad (4.26)$$

3. Neutral element:

$$\exists 0 \in \mathbb{R}_{p,q} : a + 0 = a \quad \forall a \in \mathbb{R}_{p,q} \quad (4.27)$$

4. Associativity:

$$\alpha(\beta a) = (\alpha\beta)a \quad \forall \alpha, \beta \in \mathbb{R} \quad \forall a \in \mathbb{R}_{p,q} \quad (4.28)$$

5. Commutativity:

$$\alpha a = a\alpha \quad \forall \alpha \in \mathbb{R} \quad \forall a \in \mathbb{R}_{p,q} \quad (4.29)$$

6. Neutral element:

$$\exists 1 \in \mathbb{R} : 1a = a \quad \forall a \in \mathbb{R}_{p,q} \quad (4.30)$$

#### 4. The Isotropic 2D Analytic Signal

7. Distributivity:

$$\alpha(a + b) = \alpha a + \alpha b \quad \forall \alpha \in \mathbb{R} \quad \forall a, b \in \mathbb{R}_{p,q} \quad (4.31)$$

8. Distributivity:

$$(\alpha + \beta)a = \alpha a + \beta a \quad \forall \alpha, \beta \in \mathbb{B} \quad \forall a \in \mathbb{R}_{p,q} \quad (4.32)$$

From these axioms it follows that

$$\forall a \in \mathbb{R}_{p,q} \quad \exists -a = (-1)a : a + (-a) = 0 \quad (4.33)$$

The axioms related to the algebraic product, i.e. the geometric product  $\circ$ , are as follows.

Let  $a, b, c \in \mathbb{R}_{p,q}$  and  $\alpha, \beta \in \mathbb{R}$

1. The geometric algebra is closed:

$$\forall a, b \in \mathbb{R}_{p,q} : a \circ b \in \mathbb{R}_{p,q} \quad (4.34)$$

2. Associativity:

$$\forall a, b, c \in \mathbb{R}_{p,q} : (a \circ b) \circ c = a \circ (b \circ c) \quad (4.35)$$

3. Distributivity:

$$\forall a, b, c \in \mathbb{R}_{p,q} : a \circ (b + c) = a \circ b + a \circ c \quad (4.36)$$

and

$$\forall a, b, c \in \mathbb{R}_{p,q} : (b + c) \circ a = b \circ a + c \circ a \quad (4.37)$$

4. Scalar multiplication:

$$\forall \alpha \in \mathbb{R} \quad \forall a \in \mathbb{R}_{p,q} : \alpha \circ a = a \circ \alpha = \alpha a \quad (4.38)$$

All axioms above define an associative but non-commutative algebra. What actually separates Clifford algebras from other algebras is the defining equation:

$$\forall a \in \mathbb{R}^{p,q} \subset \mathbb{R}_{p,q} : a \circ a = a * a \in \mathbb{R} , \quad (4.39)$$

i.e. the geometric product  $\circ$  of a vector (not a multi-vector in general) with itself maps to an element of the field  $\mathbb{R}$ .

### Basic Properties

All properties of the geometric algebra  $\mathbb{R}_{p,q}$  can be derived from the axioms given in this section. In the geometric algebra, the geometric product of two vectors  $a, b \in \mathbb{R}^{p,0}$  embedded in  $\mathbb{R}_{p,0}$  is given by:

$$a \circ b = a \cdot b + a \wedge b \in \mathbb{R}_{p,0} \quad (4.40)$$

	1	$\mathbf{e}_1$	$\mathbf{e}_2$	$\mathbf{e}_{12}$
1	1	$\mathbf{e}_1$	$\mathbf{e}_2$	$\mathbf{e}_{12}$
$\mathbf{e}_1$	$\mathbf{e}_1$	1	$\mathbf{e}_{12}$	$\mathbf{e}_2$
$\mathbf{e}_2$	$\mathbf{e}_2$	$-\mathbf{e}_{12}$	1	$-\mathbf{e}_1$
$\mathbf{e}_{12}$	$\mathbf{e}_{12}$	$-\mathbf{e}_2$	$\mathbf{e}_1$	-1

Table 4.1.: Multiplication table of the basis multi-vectors  $\{1, \mathbf{e}_1, \mathbf{e}_2, \mathbf{e}_{12}\}$ . The left factors of the geometric product are indicated by the first row and the right factors by the first column. It is important to note that the substructure  $\mathbb{R}_2^+ \subset \mathbb{R}_2$  is isomorphic to the complex numbers  $\mathbb{C}$ , i.e.  $\mathbb{R}_2^+ \cong \mathbb{C}$ , with  $\mathbf{i} \cong \mathbf{e}_{12}$ .

	1	$\mathbf{e}_1$	$\mathbf{e}_2$	$\mathbf{e}_3$	$\mathbf{e}_{23}$	$\mathbf{e}_{31}$	$\mathbf{e}_{12}$	$\mathbf{e}_{123}$
1	1	$\mathbf{e}_1$	$\mathbf{e}_2$	$\mathbf{e}_3$	$\mathbf{e}_{23}$	$\mathbf{e}_{31}$	$\mathbf{e}_{12}$	$\mathbf{e}_{123}$
$\mathbf{e}_1$	$\mathbf{e}_1$	1	$\mathbf{e}_{12}$	$-\mathbf{e}_{31}$	$\mathbf{e}_{123}$	$-\mathbf{e}_3$	$\mathbf{e}_2$	$\mathbf{e}_{23}$
$\mathbf{e}_2$	$\mathbf{e}_2$	$-\mathbf{e}_{12}$	1	$\mathbf{e}_{23}$	$\mathbf{e}_3$	$\mathbf{e}_{123}$	$-\mathbf{e}_1$	$\mathbf{e}_{31}$
$\mathbf{e}_3$	$\mathbf{e}_3$	$\mathbf{e}_{31}$	$-\mathbf{e}_{23}$	1	$-\mathbf{e}_2$	$\mathbf{e}_1$	$\mathbf{e}_{123}$	$\mathbf{e}_{12}$
$\mathbf{e}_{23}$	$\mathbf{e}_{23}$	$\mathbf{e}_{123}$	$-\mathbf{e}_3$	$\mathbf{e}_2$	-1	$-\mathbf{e}_{12}$	$\mathbf{e}_{31}$	$-\mathbf{e}_1$
$\mathbf{e}_{31}$	$\mathbf{e}_{31}$	$\mathbf{e}_3$	$\mathbf{e}_{123}$	$-\mathbf{e}_1$	$\mathbf{e}_{12}$	-1	$-\mathbf{e}_{23}$	$-\mathbf{e}_2$
$\mathbf{e}_{12}$	$\mathbf{e}_{12}$	$-\mathbf{e}_2$	$\mathbf{e}_1$	$\mathbf{e}_{123}$	$-\mathbf{e}_{31}$	$\mathbf{e}_{23}$	-1	$-\mathbf{e}_3$
$\mathbf{e}_{123}$	$\mathbf{e}_{123}$	$\mathbf{e}_{23}$	$\mathbf{e}_{31}$	$\mathbf{e}_{12}$	$-\mathbf{e}_1$	$-\mathbf{e}_2$	$-\mathbf{e}_3$	-1

Table 4.2.: Multiplication table of the basis multi-vectors  $\{1, \mathbf{e}_1, \mathbf{e}_2, \mathbf{e}_3, \mathbf{e}_{23}, \mathbf{e}_{31}, \mathbf{e}_{12}, \mathbf{e}_{123}\}$ . The left factors of the geometric product are indicated by the first row and the right factors by the first column. Note that the substructure  $\mathbb{R}_3^+ \subset \mathbb{R}_3$  is isomorphic to the quaternions  $\mathbb{H}$ .

#### 4. The Isotropic 2D Analytic Signal

where  $a \cdot b$  is the inner product, and  $a \wedge b$  is the wedge or outer product of the vectors  $a$  and  $b$ . It follows that the inner product  $\cdot$  of two vectors  $a$  and  $b$  can be written as

$$a \cdot b = \frac{1}{2}(ab + ba) \quad (4.41)$$

and their wedge product can be written as

$$a \wedge b = \frac{1}{2}(ab - ba) . \quad (4.42)$$

Given two vectors  $u = \sum_{\nu=1}^3 u_{\nu} \mathbf{e}_{\nu}$  and  $v = \sum_{\nu=1}^3 v_{\nu} \mathbf{e}_{\nu}$  the geometric product is given by

$$uv = \underbrace{\sum_{\nu=1}^3 u_{\nu} v_{\nu}}_{\text{scalar part}} + \underbrace{(u_1 v_2 - u_2 v_1) \mathbf{e}_{12} + (u_1 v_3 - u_3 v_1) \mathbf{e}_{13} + (u_2 v_3 - u_3 v_2) \mathbf{e}_{32}}_{\text{bivector part}} . \quad (4.43)$$

One can immediately recognize the combination of the ordinary dot product and the cross product known from  $\mathbb{R}^3$ .

The associative geometric algebra

$$\mathbb{R}_3 = \text{gen}\{\mathbf{e}_1, \mathbf{e}_2, \mathbf{e}_3\} \quad (4.44)$$

is generated by taking the sums of geometric products of three orthonormal real basis vectors  $\mathbf{e}_{\nu}$  with  $\nu \in \{1, 2, 3\}$ , subject to the rules that

$$\mathbf{e}_{\nu}^2 = 1 \quad \forall \nu \in \{1, 2, 3\} . \quad (4.45)$$

Products of the basis vectors are denoted by

$$\mathbf{e}_{\nu \dots \mu} = \mathbf{e}_{\nu} \dots \mathbf{e}_{\mu} . \quad (4.46)$$

As a linear space, the geometric algebra  $\mathbb{R}_3$  is spanned by the basis  $B$ , where

$$B = \{1, \mathbf{e}_1, \mathbf{e}_2, \mathbf{e}_3, \mathbf{e}_{23}, \mathbf{e}_{31}, \mathbf{e}_{12}, \mathbf{e}_{123}\} . \quad (4.47)$$

Consequently, we can express a general element  $a \in \mathbb{R}_3$  in the form

$$a = a_0 + \mathbf{a} \quad (4.48)$$

where

$$\mathbf{a} = \sum_{\nu=1}^3 a_{\nu} \mathbf{e}_{\nu} \in \mathbb{R}_3^{1,2} \quad (4.49)$$

is a hypercomplex vector, i.e. vector + bivector, and  $a_{\nu} \in \mathbb{R}_3^{0,3}$  for  $\nu \in \{0, 1, 2, 3\}$  are complex scalars, i.e. scalars + pseudoscalars or trivectors. Note that the complex scalars

make up the center of the algebra  $\mathbb{R}_3$  in that they commute with all of the elements of  $\mathbb{R}_3$ . The center of the geometric algebra  $\mathbb{R}_3$  is defined by

$$Z(\mathbb{R}_3) = \{c \in \mathbb{R}_3 : ca = ac \forall a \in \mathbb{R}_3\} \quad (4.50)$$

which is closed under the geometric product. The structure of the geometric algebra  $\mathbb{R}_3$  is closely related to the Gibbs-Heaviside vector algebra. Let  $a = a_0 + \mathbf{a}$  and  $b = b_0 + \mathbf{b}$  be elements of  $\mathbb{R}_3$ . The geometric product reads

$$ab = (a_0 + \mathbf{a})(b_0 + \mathbf{b}) = (a_0b_0 + \mathbf{a} \odot \mathbf{b}) + (b_0\mathbf{a} + a_0\mathbf{b} + \mathbf{a} \otimes \mathbf{b}) \quad (4.51)$$

where the complex inner product reads

$$\mathbf{a} \odot \mathbf{b} = \sum_{\nu=1}^3 a_\nu b_\nu \quad (4.52)$$

and the complex vector product reads

$$\mathbf{a} \otimes \mathbf{b} = \text{idet} \begin{bmatrix} \mathbf{e}_1 & \mathbf{e}_2 & \mathbf{e}_3 \\ a_1 & a_2 & a_3 \\ b_1 & b_2 & b_3 \end{bmatrix} = (\mathbf{ia}) \times \mathbf{b} \quad (4.53)$$

where  $\mathbf{a} \times \mathbf{b}$  is the ordinary Gibbs-Heaviside cross product when the vectors  $\mathbf{a}$  and  $\mathbf{b}$  are real. For real vectors  $\mathbf{a}$  and  $\mathbf{b}$ ,

$$(\mathbf{ia}) \times \mathbf{b} = \mathbf{i}(\mathbf{a} \times \mathbf{b}) \quad (4.54)$$

has the geometric interpretation of the bivector normal to the vector  $\mathbf{a} \times \mathbf{b}$ . Note also that we have the complex triple product

$$\mathbf{a} \odot \mathbf{b} \otimes \mathbf{c} = \text{idet} \begin{bmatrix} a_1 & a_2 & a_3 \\ b_1 & b_2 & b_3 \\ c_1 & c_2 & c_3 \end{bmatrix}. \quad (4.55)$$

The geometric product  $\mathbf{ab}$  of complex vectors  $\mathbf{a}, \mathbf{b} \in \mathbb{R}_3^{1,2}$  can be expressed in the form

$$\mathbf{ab} = \frac{1}{2}(\mathbf{ab} + \mathbf{ba}) + \frac{1}{2}(\mathbf{ab} - \mathbf{ba}) = \mathbf{a} \odot \mathbf{b} + \mathbf{a} \otimes \mathbf{b} \quad (4.56)$$

where

$$\mathbf{a} \odot \mathbf{b} = \frac{1}{2}(\mathbf{ab} + \mathbf{ba}) \quad (4.57)$$

and

$$\mathbf{a} \otimes \mathbf{b} = \frac{1}{2}(\mathbf{ab} - \mathbf{ba}) \quad (4.58)$$

and has no analogy in the Gibbs-Heaviside vector algebra. To understand the complex vector products on  $\mathbb{R}_3$  in more detail, we calculate  $\mathbf{abc}$  for the three complex vectors  $\mathbf{a}, \mathbf{b}, \mathbf{c} \in \mathbb{R}_3^{1,2}$ ,

$$\mathbf{a}(\mathbf{bc}) = \mathbf{a}(\mathbf{b} \odot \mathbf{c} + \mathbf{b} \otimes \mathbf{c}) = (\mathbf{b} \odot \mathbf{c})\mathbf{a} + \mathbf{a} \odot (\mathbf{b} \otimes \mathbf{c}) + \mathbf{a} \otimes (\mathbf{b} \otimes \mathbf{c}). \quad (4.59)$$

#### 4. The Isotropic 2D Analytic Signal

The last triple product can be expanded as

$$\mathbf{a} \otimes (\mathbf{b} \otimes \mathbf{c}) = (\mathbf{a} \odot \mathbf{b})\mathbf{c} - (\mathbf{a} \odot \mathbf{c})\mathbf{b} . \quad (4.60)$$

Let  $a \in \mathbb{R}_3$ . By  $a^*$  the inversion from  $a$  can be obtained by replacing  $v$  by  $-v$  for all real vectors  $v$  which are contained in  $a$ . For example, if

$$a = s + \mathbf{v} + \mathbf{b} + t \quad (4.61)$$

with  $s$  as the real scalar,  $v$  as the real vector,  $b$  as the real bivector and  $t$  as the real trivector, then the inversion of  $a$  results in

$$a^* = s - \mathbf{v} + \mathbf{b} - t . \quad (4.62)$$

The reversion  $a^\dagger$  of  $a$  is defined by reversing the order of the geometric product of all real vectors in  $a$ . For  $a \in \mathbb{R}_3$  given above,

$$a^\dagger = s + \mathbf{v} - \mathbf{b} - t . \quad (4.63)$$

Finally, the conjugation  $\bar{a}$  is defined by  $\bar{a} = (a^*)^\dagger$ . For the given  $a$ ,

$$\bar{a} = s - \mathbf{v} - \mathbf{b} + t . \quad (4.64)$$

We see that, unlike the usual complex conjugation, for

$$b = b_0 + \mathbf{b} \in \mathbb{R}_3 \quad (4.65)$$

$$\bar{b} = b_0 - \mathbf{b} . \quad (4.66)$$

Clearly, the various multi-vector parts of  $a$  are all expressible in terms of  $a$ ,  $a^*$ ,  $a^\dagger$ ,  $\bar{a}$ . A general complex element

$$a = a_0 + \mathbf{a} \in \mathbb{R}_3 \quad (4.67)$$

will have an inverse if and only if

$$\det(a) \neq 0 \quad (4.68)$$

with

$$\det(a) = a\bar{a} = a_0^2 - \mathbf{a}^2 \quad (4.69)$$

and it is natural to define the determinant function  $\det(a)$  of  $a \in \mathbb{R}_3$  in terms of this quantity.

### 4.3.2. Matrix Geometric Algebra

The matrix geometric algebra  $M(2, \mathbb{R}_3)$  consists of all matrices of the form

$$G = \varphi^{-1}(g) = \begin{bmatrix} G_{11} & G_{12} \\ G_{21} & G_{22} \end{bmatrix} \quad (4.70)$$



where  $G_{\nu\mu} \in \mathbb{R}_3$ . The matrix addition and multiplication in  $M(2, \mathbb{R}_3)$  equal the conventional matrix addition and multiplication, but attention should be paid to the order of the elements in the product, since in general  $ab \neq ba$  in  $\mathbb{R}_3$ .  $M(2, \mathbb{R}_3)$  is called the hybrid matrix geometric algebra (HMGA) over the geometric algebra  $\mathbb{R}_3$ . Matrices have been already studied in [44, 58], and in many other works. Let us now evaluate how a general element  $G = \varphi^{-1}(g) \in M(2, \mathbb{R}_3)$  represents an element  $g$  in the geometric algebra  $\mathbb{R}_{4,1}$ . We consider the geometric algebra  $\mathbb{R}_{4,1}$  to be the geometric algebra  $\mathbb{R}_3$  being extended by two additional orthonormal basis multi-vectors  $\mathbf{e}_+ \in \mathbb{R}_{4,1}$  and  $\mathbf{e}_- \in \mathbb{R}_{4,1}$  satisfying  $\mathbf{e}_+^2 = 1$  and  $\mathbf{e}_-^2 = -1$ . The geometric algebra  $\mathbb{R}_3$  is thus a subalgebra of the larger geometric algebra  $\mathbb{R}_{4,1}$ ,

$$\mathbb{R}_3 \subset \mathbb{R}_{4,1} = \text{gen} \{ \mathbf{e}_1, \mathbf{e}_2, \mathbf{e}_3, \mathbf{e}_+, \mathbf{e}_- \} . \quad (4.71)$$

In order to represent an element  $g \in \mathbb{R}_{4,1}$  as a matrix  $G = \varphi^{-1}(g) \in M(2, \mathbb{R}_3)$ , the following special elements are introduced

$$u = \mathbf{e}_+ \mathbf{e}_- \quad (4.72)$$

$$u_{\pm} = \frac{1}{2} (1 \pm u) \quad (4.73)$$

with the properties

$$\mathbf{e}_+ u = -u \mathbf{e}_+ \quad (4.74)$$

and

$$\mathbf{e}_+ u_{\pm} = u_{\mp} \mathbf{e}_+ . \quad (4.75)$$

Since  $u^2 = 1$ , it follows that  $u_+$  and  $u_-$  are mutually annihilating idempotents with partition 1, i.e.:

$$[1, \mathbf{e}_+] u_+ \begin{bmatrix} 1 \\ \mathbf{e}_+ \end{bmatrix} = u_+ + u_- = 1 . \quad (4.76)$$

Noting that  $ua = au$  and  $\mathbf{e}_+ a = a^* \mathbf{e}_+$  for any element  $a \in \mathbb{R}_3$ , any  $g \in \mathbb{R}_{4,1}$  can be expressed in the form

$$g = \varphi(G) = G_{11} u_+ + G_{12} u_+ \mathbf{e}_+ + G_{21}^* u_- \mathbf{e}_+ + G_{22}^* u_- \quad (4.77)$$

for  $G_{\nu\mu} \in \mathbb{R}_3$ . Now using Equations (4.77), (4.72), (4.73), and (4.76), the matrix form  $G = \varphi^{-1}(g) \in M(2, \mathbb{R}_3)$  follows from

$$\begin{aligned} g &= \underbrace{[1, \mathbf{e}_+] u_+}_{1} \begin{bmatrix} 1 \\ \mathbf{e}_+ \end{bmatrix} \underbrace{g [1, \mathbf{e}_+] u_+}_{1} \begin{bmatrix} 1 \\ \mathbf{e}_+ \end{bmatrix} \\ &= [1, \mathbf{e}_+] u_+ \left[ \begin{bmatrix} g & g \mathbf{e}_+ \\ \mathbf{e}_+ g & \mathbf{e}_+ g \mathbf{e}_+ \end{bmatrix} u_+ \right] \begin{bmatrix} 1 \\ \mathbf{e}_+ \end{bmatrix} \\ &= [1, \mathbf{e}_+] u_+ \varphi^{-1}(g) \begin{bmatrix} 1 \\ \mathbf{e}_+ \end{bmatrix} \end{aligned} \quad (4.78)$$

#### 4. The Isotropic 2D Analytic Signal

with

$$\varphi^{-1}(g) = G = \begin{bmatrix} G_{11} & G_{12} \\ G_{21} & G_{22} \end{bmatrix}. \quad (4.79)$$

Extending the operations of inversion  $g^*$ , reversion  $g^\dagger$ , and conjugation  $\bar{g}$  to the larger geometric algebra  $\mathbb{R}_{4,1}$ , it follows

$$g^* = G_{11}^* u_+ - G_{12}^* u_+ \mathbf{e}_+ - G_{21} u_- \mathbf{e}_+ + G_{22} u_-, \quad (4.80)$$

$$g^\dagger = \bar{G}_{22} u_+ + \bar{G}_{12} u_+ \mathbf{e}_+ + G_{21}^\dagger u_- \mathbf{e}_+ + G_{11}^\dagger u_-, \quad (4.81)$$

$$\bar{g} = G_{22}^\dagger u_+ - G_{12}^\dagger u_+ \mathbf{e}_+ - \bar{G}_{21} u_- \mathbf{e}_+ + \bar{G}_{11} u_- \quad (4.82)$$

from which follows the corresponding operations in the Hybrid matrix algebra

$$G^\dagger = \varphi^{-1}(g^\dagger) = \begin{bmatrix} \bar{G}_{22} & \bar{G}_{12} \\ \bar{G}_{21} & \bar{G}_{11} \end{bmatrix}, \quad (4.83)$$

$$G^* = \varphi^{-1}(g^*) = \begin{bmatrix} G_{11}^* & -G_{12}^* \\ -G_{21}^* & G_{22}^* \end{bmatrix}, \quad (4.84)$$

$$\bar{G} = \varphi^{-1}(\bar{g}) = \begin{bmatrix} G_{22}^\dagger & -G_{12}^\dagger \\ -G_{21}^\dagger & G_{11}^\dagger \end{bmatrix}. \quad (4.85)$$

### 4.3.3. Inverse Element

The objective now is to determine the condition on the elements in  $\mathbb{R}_3$  which will guarantee that a given hybrid matrix geometric algebra element  $G = \varphi^{-1}(g)$  will have an inverse element  $G^{-1}$ . First, the determinant function has to be extended to a function defined on the hybrid geometric algebra by requiring that it satisfies the following important properties: for  $G_{\nu\mu}, e \in \mathbb{R}_3$ ,

$$\det \begin{bmatrix} G_{11} & G_{12} \\ 0 & G_{22} \end{bmatrix} = G_{11} \bar{G}_{11} G_{22} \bar{G}_{22}, \quad (4.86)$$

$$\det \begin{bmatrix} eG_{11} & eG_{12} \\ G_{21} & G_{22} \end{bmatrix} = e \bar{e} \det(G), \quad (4.87)$$

$$\det \begin{bmatrix} G_{11} & G_{12} \\ eG_{11} + G_{21} & eG_{12} + G_{22} \end{bmatrix} = \det(G). \quad (4.88)$$

These properties agree with the conventional definition of the determinant function, a consequence of what is known as the generalized algorithm of Gauss. Now the following theorem about hybrid determinants can be proved

**Theorem 4.3.1.**

$$\begin{aligned} \det \begin{bmatrix} G_{11} & G_{12} \\ G_{21} & G_{22} \end{bmatrix} &= G_{11} \bar{G}_{11} G_{22} \bar{G}_{22} + G_{12} \bar{G}_{12} G_{21} \bar{G}_{21} \\ &\quad - (\bar{G}_{11} G_{12} \bar{G}_{22} G_{21} + \bar{G}_{21} G_{22} \bar{G}_{12} G_{11}) \end{aligned} \quad (4.89)$$

with  $\bar{G}_{\nu\mu} = s - v - b + t$ .

*Proof:* The determinant of  $G$  reads

$$\begin{aligned}
 \det(G) &= (G_{11}\bar{G}_{11})^{-1} \det \begin{bmatrix} \bar{G}_{11}G_{11} & \bar{G}_{11}G_{12} \\ G_{21} & G_{22} \end{bmatrix} \\
 &= (G_{11}\bar{G}_{11})^{-3} \det \begin{bmatrix} \bar{G}_{11}G_{11} & \bar{G}_{11}G_{12} \\ \bar{G}_{11}G_{11}G_{21} & \bar{G}_{11}G_{11}G_{22} \end{bmatrix} \\
 &= (G_{11}\bar{G}_{11})^{-3} \det \begin{bmatrix} \bar{G}_{11}G_{11} & \bar{G}_{11}G_{12} \\ 0 & \bar{G}_{11}G_{11}G_{22} - G_{21}\bar{G}_{11}G_{12} \end{bmatrix} \\
 &= (G_{11}\bar{G}_{11})^{-1} ((G_{11}\bar{G}_{11}G_{22} - G_{21}\bar{G}_{11}G_{12})(G_{11}\bar{G}_{11}\bar{G}_{22} - \bar{G}_{12}G_{11}\bar{G}_{21})) \\
 &= G_{11}\bar{G}_{11}G_{22}\bar{G}_{22} + G_{12}\bar{G}_{12}G_{21}\bar{G}_{21} - (\bar{G}_{11}G_{12}\bar{G}_{22}G_{21} + \bar{G}_{21}G_{22}\bar{G}_{12}G_{11})
 \end{aligned}$$

□

In the proof of the above theorem, it is assumed that the element  $G_{11} \in \mathbb{R}_3$  is invertible, which is not the case in general. Nevertheless, the theorem remains valid in these cases, as can be argued by standing continuity requirements. The non-vanishing of the determinant function  $\det(G) \neq 0$  is the condition for the invertibility of a general element  $g \in \mathbb{R}_{4,1}$ . An expression for the inverse of the hybrid matrix  $G$  can be derived by the common trick of applying the generalized Gauss algorithm to the augmented matrix

$$\begin{bmatrix} G_{11} & G_{12} & 1 & 0 \\ G_{21} & G_{22} & 0 & 1 \end{bmatrix} \quad (4.90)$$

to get the result

$$IG^{-1} = \begin{bmatrix} 1 & 0 \\ 0 & 1 \end{bmatrix} \begin{bmatrix} G_{11} & G_{12} \\ G_{21} & G_{22} \end{bmatrix}^{-1}. \quad (4.91)$$

The final result reads

$$G^{-1} = \frac{1}{\det(G)} \begin{bmatrix} M_{11} & M_{12} \\ M_{21} & M_{22} \end{bmatrix} \quad (4.92)$$

with the entries

$$M_{11} = \bar{G}_{11}G_{22}\bar{G}_{22} - \bar{G}_{21}G_{22}\bar{G}_{12}, \quad (4.93)$$

$$M_{12} = G_{12}\bar{G}_{12}\bar{G}_{21} - \bar{G}_{11}G_{12}\bar{G}_{22}, \quad (4.94)$$

$$M_{21} = \bar{G}_{12}G_{21}\bar{G}_{21} - \bar{G}_{22}G_{21}\bar{G}_{11}, \quad (4.95)$$

$$M_{22} = G_{11}\bar{G}_{11}\bar{G}_{22} - \bar{G}_{12}G_{11}\bar{G}_{21}. \quad (4.96)$$

#### 4.3.4. The Homogeneous Conformal Geometric Algebra

The Euclidean space can be embedded in a higher dimensional conformal space, where the extra dimensions have particular properties such that linear subspaces in conformal space represent geometric entities in Euclidean space [54, 42]. In projective space, the additional dimension allows the representation of null-dimensional spaces, i.e. points, in Euclidean space by one-dimensional subspaces in projective space. This allows points to be distinguished from directions. The homogeneous conformal space will be introduced

#### 4. The Isotropic 2D Analytic Signal

in two steps where, each time, the dimensionality of the space will be extended by one. In the first step, Euclidean space is embedded in a non-linear way in a higher-dimensional space. The actual conformal space that is used later on is a special homogenization of the initial non-linear embedding of Euclidean space. What is meant by conformal space is therefore the projective space of a conformal embedding of Euclidean space. The geometric algebra over this conformal space is called homogeneous conformal geometric algebra (CGA), even though this terminology is not completely exact.

Before the conformal embedding of Euclidean space can be introduced, it is helpful to first know what "conformal" actually means. A conformal mapping is one that preserves angles locally. For example, a conformal mapping of two intersecting straight lines in Euclidean space may result in two intersecting circles on the sphere. However, the angle at which the circles intersect on the sphere is the same as the intersection angle of the lines in the flat Euclidean space. Furthermore, it turns out that all conformal mappings can be expressed by means of combinations of inversions. In a 1D Euclidean space  $\mathbb{R}$ , the inversion of a vector  $x \in \mathbb{R}$  in the unit one-dimensional sphere centered on the origin is simply  $x^{-1}$ . In  $\mathbb{R}^3$ , the inversion of a plane in the unit sphere centered on the origin is a sphere. Note that inversions are closely related to reflections, in that a reflection is a special case of an inversion. In fact, an inversion in a sphere with an infinite radius, i.e. a plane, is a reflection. All Euclidean mappings can be represented by combinations of two reflections. A translation may be represented by the reflections in two parallel reflection planes. Since all Euclidean mappings can be represented by combinations of reflections and all conformal mappings by combinations of inversions, it follows that the Euclidean mappings form a subset of the conformal mappings. The reason why the embedding of Euclidean space in conformal space is particularly useful is that a reflection in the conformal embedding space represents an inversion in the corresponding Euclidean space. The reflection of a blade in any other blade is, however, the fundamental transformation operation of geometric algebra. A blade is defined to be the outer product of an arbitrary number of 1-vectors.

Using Equation (4.77), the matrix representation of the basis multi-vectors of the geometric algebra  $\mathbb{R}_{4,1}$  result in

$$\varphi^{-1}(\mathbf{e}_\nu) = \begin{bmatrix} \mathbf{e}_\nu & 0 \\ 0 & -\mathbf{e}_\nu \end{bmatrix}, \quad (4.97)$$

$$\varphi^{-1}(\mathbf{e}_+) = \begin{bmatrix} 0 & 1 \\ 1 & 0 \end{bmatrix}, \quad (4.98)$$

$$\varphi^{-1}(\mathbf{e}_-) = \begin{bmatrix} 0 & -1 \\ 1 & 0 \end{bmatrix}, \quad (4.99)$$

furthermore

$$\varphi^{-1}(u) = \varphi^{-1}(\mathbf{e}_+ \mathbf{e}_-) = \begin{bmatrix} 1 & 0 \\ 0 & -1 \end{bmatrix}, \quad (4.100)$$

$$\varphi^{-1}(u_+) = \begin{bmatrix} 1 & 0 \\ 0 & 0 \end{bmatrix}, \quad (4.101)$$

$$\varphi^{-1}(u_-) = \begin{bmatrix} 0 & 0 \\ 0 & 1 \end{bmatrix}. \quad (4.102)$$

The matrix representation of any other element can be calculated by taking sums of products of the matrix representations of the multi-vector basis elements. For example, defining the null vectors

$$\mathbf{e} = \frac{1}{2}(\mathbf{e}_+ + \mathbf{e}_-) \quad (4.103)$$

and

$$\bar{\mathbf{e}} = \mathbf{e}_+ - \mathbf{e}_-, \quad (4.104)$$

with  $\mathbf{e}^2 = \bar{\mathbf{e}}^2 = 0$ , it follows that

$$\varphi^{-1}(\mathbf{e}) = \begin{bmatrix} 0 & 0 \\ 1 & 0 \end{bmatrix} \quad (4.105)$$

and

$$\varphi^{-1}(\bar{\mathbf{e}}) = \begin{bmatrix} 0 & 2 \\ 0 & 0 \end{bmatrix}. \quad (4.106)$$

Calculating the various conjugation operations on a general multi-vector

$$g = s + v + b + t + f + p \in \mathbb{R}_{4,1} \quad (4.107)$$

with the grade- $\nu$  projection  $\langle \cdot \rangle_\nu$  [49]

$$s = \langle g \rangle_0, \quad (4.108)$$

$$v = \langle g \rangle_1, \quad (4.109)$$

$$b = \langle g \rangle_2, \quad (4.110)$$

$$t = \langle g \rangle_3, \quad (4.111)$$

$$f = \langle g \rangle_4, \quad (4.112)$$

$$p = \langle g \rangle_5. \quad (4.113)$$

delivers

$$g^* = s - v + b - t + f - p, \quad (4.114)$$

$$g^\dagger = s + v - b - t + f + p, \quad (4.115)$$

$$\bar{g} = s - v - b + t + f - p \quad (4.116)$$

#### 4. The Isotropic 2D Analytic Signal

and finally

$$\frac{1}{4} (g + g^* + g^\dagger + \bar{g}) = s + f, \quad (4.117)$$

$$\frac{1}{4} (g - g^* + g^\dagger - \bar{g}) = v + p, \quad (4.118)$$

$$\frac{1}{4} (g + g^* - g^\dagger - \bar{g}) = b, \quad (4.119)$$

$$\frac{1}{4} (g - g^* - g^\dagger + \bar{g}) = t. \quad (4.120)$$

#### 4.3.5. The Projective Space

We now want to introduce a unified framework for geometric entities such as points, lines, circles, planes and spheres as well as for any Möbius transforms. Special representations of the points  $\mathbf{x} \in \mathbb{R}^3$  in the larger pseudo-Euclidean space  $\mathbb{R}^{4,1}$  will now be investigated. Each real vector  $x \in \mathbb{R}^{4,1}$  has the form

$$x = \mathbf{x} + \alpha \mathbf{e} + \frac{1}{2} \beta \bar{\mathbf{e}}, \quad (4.121)$$

with  $\alpha, \beta \in \mathbb{R}$ . If  $\alpha = 1$  and  $\beta = 0$ ,

$$x_h = \mathbf{x} + \mathbf{e} \in \mathbb{R}^{4,1} \quad (4.122)$$

represents  $\mathbf{x} \in \mathbb{R}^3$  in the affine plane

$$A_{\mathbf{e}}(\mathbb{R}^3) = \{x = \mathbf{x} + \mathbf{e} : \mathbf{x} \in \mathbb{R}^3\}. \quad (4.123)$$

Properties of the affine plane have been studied by [49].

#### 4.3.6. The Homogeneous Conformal Space

The affine plane will be extended by the horosphere  $H(\mathbb{R}^3)$ , which is a nonlinear representation of the points in Euclidean space  $\mathbb{R}^3$ , defined by the condition that

$$x_c = x_h + \beta \bar{\mathbf{e}} = \mathbf{x} + \mathbf{e} + \beta \bar{\mathbf{e}} \quad (4.124)$$

is a null vector for all  $\mathbf{x} \in \mathbb{R}^3$ . It follows that

$$x_c^2 = x_h^2 + 2\beta \bar{\mathbf{e}} \cdot x_h = \mathbf{x}^2 + 2\beta = 0 \quad (4.125)$$

or  $\beta = -\frac{1}{2} \mathbf{x}^2$ . Thus,

$$H(\mathbb{R}^3) = \left\{ x_c = \mathbf{x} - \frac{1}{2} \mathbf{x}^2 \bar{\mathbf{e}} + \mathbf{e} : \mathbf{x} \in \mathbb{R}^3 \right\}, \quad (4.126)$$

and compare this result with the conformal mapping

$$\mathcal{C}(\mathbf{x}) = \mathbf{x} + \frac{1}{2} \mathbf{x}^2 \mathbf{e}_\infty + \mathbf{e}_0 \quad (4.127)$$

for  $\mathbf{x} \in \mathbb{R}^3$  in [49], where  $\mathbf{e}_\infty = \mathbf{e}_- + \mathbf{e}_+$  and  $\mathbf{e}_0 = \frac{1}{2}(\mathbf{e}_- - \mathbf{e}_+)$  with the properties  $\mathbf{e}_\infty^2 = \mathbf{e}_0^2 = 0$  and  $\mathbf{e}_\infty \cdot \mathbf{e}_0 = -1$ . Even though such a basis is rather uncommon, using  $\mathbf{e}_\infty$  and  $\mathbf{e}_0$  instead of  $\mathbf{e}_-$  and  $\mathbf{e}_+$  is simply a basis transformation.

### 4.3.7. Reflection

Reflections are the basic element of geometric transformations since rotations and translations consist of reflections. Reflections in  $\mathbb{R}^3$  represented on the horosphere have the homogeneous form

$$S_{\mathbf{a}}(x_c) = \mathbf{a}x_c\mathbf{a} = \mathbf{a}x\mathbf{a} - \mathbf{a}^2 \left( \mathbf{e} - \frac{1}{2}\mathbf{x}^2\bar{\mathbf{e}} \right). \quad (4.128)$$

### 4.3.8. Rotation

Rotations are the composition of two reflections. It follows that

$$S_{\mathbf{b}}(S_{\mathbf{a}}(x_c)) = \mathbf{b}x_c(\mathbf{b}\mathbf{a})^\dagger = \mathbf{b}x_c\mathbf{a}\mathbf{b}. \quad (4.129)$$

### 4.3.9. Translation

Translations can also be represented in the horosphere. For  $a \in \mathbb{R}^3$ , the translation is defined by

$$T_a(x_c) = \left( 1 + \frac{1}{2}\mathbf{a}\bar{\mathbf{e}} \right) x_c \left( 1 - \frac{1}{2}\mathbf{a}\bar{\mathbf{e}} \right). \quad (4.130)$$

### 4.3.10. Hybrid Matrix Valued Signal Representation

Now we introduce a fully isomorphic and alternative algebraic representation to tensor and matrix structures, called multi-vector representation, which will be shown to be suitable for signal interpretation. It has been shown that the monogenic signal can be analyzed as a vector in Euclidean space. Now a generalized concept of the monogenic signal representation will be presented by analyzing not a vector but a so called multi-vector in conformal space. According to [53] each Clifford number valued matrix  $T \in M(2, \mathbb{R}_3)$ , with the signal position  $z \in \mathbb{R}^2$  and the scale space parameter  $s > 0$ , can be mapped to a multi-vector  $m \in \mathbb{R}_{4,1}$  of the Clifford algebra  $\mathbb{R}_{4,1}$  [12] with the set of generating basis vectors

$$B = \{\mathbf{e}_1, \mathbf{e}_2, \mathbf{e}_3, \mathbf{e}_+\} \cup \{\mathbf{e}_-\} \quad (4.131)$$

which results in the total number of  $\|2^B\| = 32$  basis multi-vectors with  $2^B$  as the powerset of the set  $B$ . The basis vectors have the properties

$$\mathbf{e}_1^2 = \mathbf{e}_2^2 = \mathbf{e}_3^2 = \mathbf{e}_+^2 = 1, \quad \mathbf{e}_-^2 = -1 \quad (4.132)$$

and

$$\mathbf{e}_i\mathbf{e}_j = -\mathbf{e}_j\mathbf{e}_i, \quad i, j \in \{1, 2, 3, +, -\}, \quad i \neq j. \quad (4.133)$$

We will use the abbreviation

$$\mathbf{e}_{ij} = \mathbf{e}_i\mathbf{e}_j \quad (4.134)$$

and in general for the totally ordered set  $I$

$$\mathbf{e}_I = \mathbf{e}_{i_1 i_2 \dots i_n} \quad \text{for} \quad I = \{i_1, i_2, \dots, i_n\} \in 2^B. \quad (4.135)$$

#### 4. The Isotropic 2D Analytic Signal

The scalar numbers  $\mathbb{R}$  will be represented by the empty set  $I = \emptyset$  with the basis multi-vector  $\mathbf{e}_\emptyset = 1$ . Note that the basis vector  $\mathbf{e}_+$  extends the three dimensional Euclidean space spanned by  $\{\mathbf{e}_1, \mathbf{e}_2, \mathbf{e}_3\}$  to the conformal space and  $\mathbf{e}_-$  extends the conformal space to the homogeneous conformal space. In literature the homogenous conformal space will be often abbreviated by conformal space. Since we use the Clifford algebra for geometric interpretation, Clifford algebra can be called geometric algebra [33]. As a direct result of [53] each Clifford valued  $2 \times 2$ -matrix of the form

$$T = \begin{bmatrix} T_{11} & T_{12} \\ T_{21} & T_{22} \end{bmatrix} \in M(2, \mathbb{R}_3) \quad (4.136)$$

can be mapped to its corresponding multi-vector  $m = \varphi(T) \in \mathbb{R}_{4,1}$  in (homogeneous) conformal space [49, 67, 64] by the following isomorphism

$$\varphi(T) = T_{11}u_+ + T_{12}u_+\mathbf{e}_+ + T_{21}^*u_-\mathbf{e}_+ + T_{22}^*u_- \quad (4.137)$$

with

$$T_{ij}^* = \langle T_{ij} \rangle_0 - \langle T_{ij} \rangle_1 + \langle T_{ij} \rangle_2 - \langle T_{ij} \rangle_3 \quad (4.138)$$

as the inversion of the multi-vector

$$T_{ij} = \sum_{\nu=0}^3 \langle T_{ij} \rangle_\nu \in \mathbb{R}_3 \quad (4.139)$$

for  $i, j \in \{1, 2\}$  with the grade- $n$  projection  $\langle \cdot \rangle_n$  [49]

$$\langle m \rangle_n = \sum_{\substack{I \in 2^B \\ \|I\|=n}} m_I \mathbf{e}_I \quad (4.140)$$

of the multi-vector

$$m = \sum_{I \in 2^B} m_I \mathbf{e}_I \in \mathbb{R}_{4,1}, m_I \in \mathbb{R} \quad (4.141)$$

and

$$u_+ = \frac{1}{2} + \frac{1}{2}\mathbf{e}_{+-}, \quad (4.142)$$

$$u_- = \frac{1}{2} - \frac{1}{2}\mathbf{e}_{+-}, \quad (4.143)$$

$$u_+\mathbf{e}_+ = \frac{1}{2}[\mathbf{e}_+ - \mathbf{e}_-] = -\mathbf{e}_0, \quad (4.144)$$

$$u_-\mathbf{e}_+ = \frac{1}{2}[\mathbf{e}_+ + \mathbf{e}_-] = \frac{1}{2}\mathbf{e}. \quad (4.145)$$



$$T^e = \begin{bmatrix} \text{img1} & \text{img2} \\ \text{img3} & \text{img4} \end{bmatrix} * f$$

Figure 4.2.: Illustration of the even tensor  $T^e$  which consists of the second order generalized Hilbert transformed signal.

This results in the general isomorphism

$$\begin{aligned} \varphi(T) &= \frac{1}{2} [T_{11} + T_{22}^*] \\ &+ \frac{1}{2} [T_{21}^* + T_{12}] \mathbf{e}_+ \\ &+ \frac{1}{2} [T_{21}^* - T_{12}] \mathbf{e}_- \\ &+ \frac{1}{2} [T_{11} - T_{22}^*] \mathbf{e}_{+-} \end{aligned} \quad (4.146)$$

Since the matrix  $T$  is isomorphic to the multi-vector  $m$ , the algebra is called a hybrid matrix geometric algebra (HMGA).

The second order partial derivatives of the well known Hessian matrix will be substituted by the second order generalized Hilbert transforms in their corresponding directions

$$T^e = \begin{bmatrix} f_{xx} & f_{xy} \\ f_{xy} & f_{yy} \end{bmatrix} \in M(2, \mathbb{R}) \quad (4.147)$$

which will be called the even tensor  $T^e$ , see Figure (4.2). The even tensor can be expressed in Fourier space as

$$T^e = \mathcal{F}_2^{-1} \left\{ (\alpha, \rho) \mapsto e^{-2\pi\rho s} \hat{f}(\alpha, \rho) \begin{bmatrix} \cos^2 \alpha & \sin \alpha \cos \alpha \\ \sin \alpha \cos \alpha & \sin^2 \alpha \end{bmatrix} \right\} \quad (4.148)$$

with  $\hat{f}(\alpha, \rho) = \mathcal{F}_2\{f\}(\alpha, \rho) \in \mathbb{C}$  as the 2D Fourier transform of the original signal  $f$  in polar coordinates with  $\alpha$  as the angular component and  $\rho$  as the radial component and  $\mathcal{F}_2^{-1}\{\cdot\}$  as the componentwise inverse 2D Fourier transform of the tensor.

The isomorphic multi-vector in conformal space reads

$$\varphi(T^e) = f_0 + f_+ \mathbf{e}_+ + f_{+-} \mathbf{e}_{+-} \quad (4.149)$$

#### 4. The Isotropic 2D Analytic Signal

$$\varphi(T^e) = \left( \begin{array}{c} \text{[Kernel 1]} + \text{[Kernel 2]} \mathbf{e}_+ + \text{[Kernel 3]} \mathbf{e}_{+-} \end{array} \right) * f$$

Figure 4.3.: Illustration of the isomorphism from the even tensor  $T^e$  structure to the multi-vector expression.

with

$$f_0 = \frac{1}{2} [f_{xx} + f_{yy}] = \frac{1}{2} f_p, \quad (4.150)$$

$$f_+ = f_{xy}, \quad (4.151)$$

$$f_{+-} = \frac{1}{2} [f_{xx} - f_{yy}] \quad (4.152)$$

with  $f_0$  as the scalar part,  $f_+$  as the vector part and  $f_{+-}$  as the so called bivector part. This multi-vector valued signal representation is delivered by a set of three convolution kernels, see Figure (4.3). Note the relation of the multi-vector valued signal representation to the 2-tensor decomposition in irreducible components by

$$\begin{aligned} \begin{bmatrix} f_{xx} & f_{xy} \\ f_{xy} & f_{yy} \end{bmatrix} &= \frac{f_{xx} + f_{yy}}{2} \begin{bmatrix} 1 & 0 \\ 0 & 1 \end{bmatrix} \\ &+ \frac{f_{xx} - f_{yy} - 2\mathbf{i}f_{xy}}{4} \begin{bmatrix} -1 & -\mathbf{i} \\ -\mathbf{i} & 1 \end{bmatrix} \\ &+ \frac{f_{xx} - f_{yy} - 2\mathbf{i}f_{xy}}{2} \begin{bmatrix} -1 & \mathbf{i} \\ \mathbf{i} & 1 \end{bmatrix}. \end{aligned} \quad (4.153)$$

## 4.4. Interpretation of the 2D Analytic Signal

The main advantage of the representation in the HMGA is the geometrical interpretation of the resulting multi-vector valued signal  $m$ .

### 4.4.1. Geometrical Signal Features

The local features which determine the signal in scale space will be separated in geometrical features and structural features. The geometrical features are the main orientation and the rotationally invariant [3] apex angle.

### Main Orientation

The main orientation [51] reads

$$\theta_m = \frac{\theta_1 + \theta_2}{2} = \frac{1}{2} \arctan \frac{f_+}{f_{+-}} . \quad (4.154)$$

In contrast to the monogenic signal the main orientation in conformal space can be evaluated also at phase positions  $\phi = k\pi$  for all  $k \in \mathbb{Z}$  where the orientation of the monogenic signal

$$\frac{\theta_1 + \theta_2}{2} = \arctan \frac{f_y}{f_x} \quad (4.155)$$

is not defined.

### Apex Angle

The apex angle  $\alpha$  (also deviation angle, opening angle or intersection angle) reads

$$\begin{aligned} \alpha &= \|\theta_1 - \theta_2\| \\ &= \arccos \frac{\sqrt{f_+^2 + f_{+-}^2}}{\|f_0\|} \\ &= \arctan \frac{\sqrt{f_0^2 - [f_+^2 + f_{+-}^2]}}{\sqrt{f_+^2 + f_{+-}^2}} \\ &= \arctan \frac{\sqrt{\det(T^e)}}{\sqrt{f_+^2 + f_{+-}^2}} \end{aligned} \quad (4.156)$$

with the determinant

$$\det(T^e) = f_{xx}f_{yy} - f_{xy}^2 \quad (4.157)$$

of the real valued matrix  $T^e$ . The apex angle<sup>1</sup> is a very important rotationally invariant local feature since it is zero for example iff the underlying structure is of intrinsic dimension one.

### 4.4.2. Homogeneous Signal

The geometric interpretation of the main orientation and the apex angle results from the signal  $f_0$  which is embedded in 3D space as a vector  $[0, 0, f_0]^T \in \mathbb{R}^3$ . This 3D vector will be rotated by the Euler angles

$$(\alpha, 2\theta_m) \in \left[0, \frac{\pi}{2}\right] \times [0, 2\pi] , \quad (4.158)$$

---

<sup>1</sup>Note that the apex angle of phase based image analysis corresponds to the shape feature of the orthogonal version of the second order derivatives [11] although they are not equal.

#### 4. The Isotropic 2D Analytic Signal

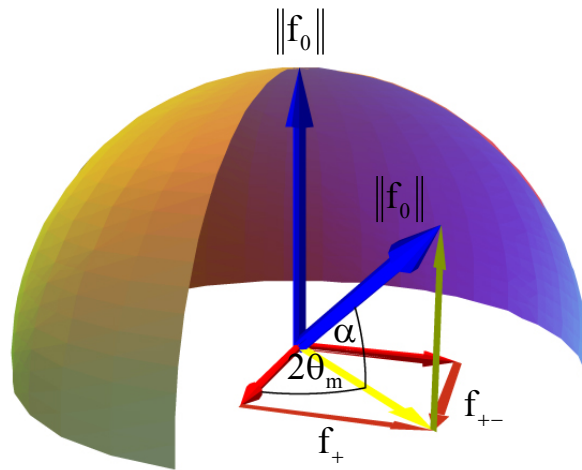


Figure 4.4.: Geometric interpretation of the main orientation  $\theta_m$  and the apex angle  $\alpha$ .

see Figure (4.4).

By means of the apex angle  $\alpha$ , a so called homogeneous signal component  $f_h$  of the signal  $f_p$  in 3D projective subspace of the conformal space will be introduced by

$$f_h = \sqrt{\frac{1 + \cos \alpha}{2}} \in [0, 1] . \quad (4.159)$$

In the following a relation of the signal representation in CGA to the projective space known from computer graphics and computer vision will be shown.

#### Main Orientation

The local main orientation of the signal can be determined by

$$\theta_m = \arctan \frac{f_h^{-1} f_y}{f_h^{-1} f_x} \quad (4.160)$$

in projective space, proof: Section (4.4.4).

#### 4.4.3. Structural Signal Features

The structural signal features are the local phase and the local amplitude.

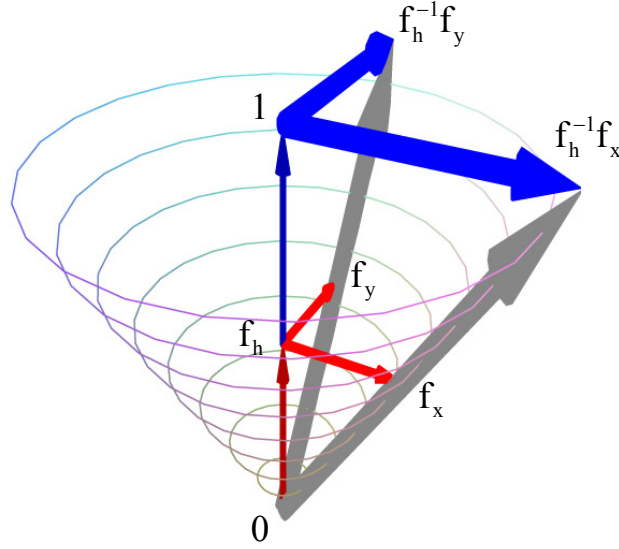


Figure 4.5.: Geometric interpretation of the projective space. The underlying 2D space is spanned by the conjugate signal components  $f_x$  and  $f_y$  and the additional coordinate of the 3D projective space is given by the homogeneous signal component  $f_h$ . All i1D and i2D signals can be normalized to a homogenous coordinate 1 by multiplying the components  $f_x$  and  $f_y$  with  $f_h^{-1}$ .

### Phase

The phase of i1D and i2D signals can be evaluated by

$$\phi = \arctan \frac{\sqrt{[f_h^{-1}f_x]^2 + [f_h^{-1}f_y]^2}}{f_p} \quad (4.161)$$

in one unified framework, proof: Section (4.4.4). The phase can be determined by the first order Hilbert transform and the geometric information given by the apex angle which will be delivered by the second order Hilbert transform.

### Amplitude

Also the local amplitude for i1D and i2D signals can be determined by

$$a = \frac{1}{2} \sqrt{f_p^2 + [f_h^{-1}f_x]^2 + [f_h^{-1}f_y]^2} \quad (4.162)$$

in one unified framework, proof: Section (4.4.4). In the case of pure i1D signals the apex angle is zero, i.e.  $f_h = 1$ . In this case the formulas of the phase and amplitude reduce to those known from the monogenic signal. The advantage of this approach is that it can automatically distinguish between i1D and i2D signals.

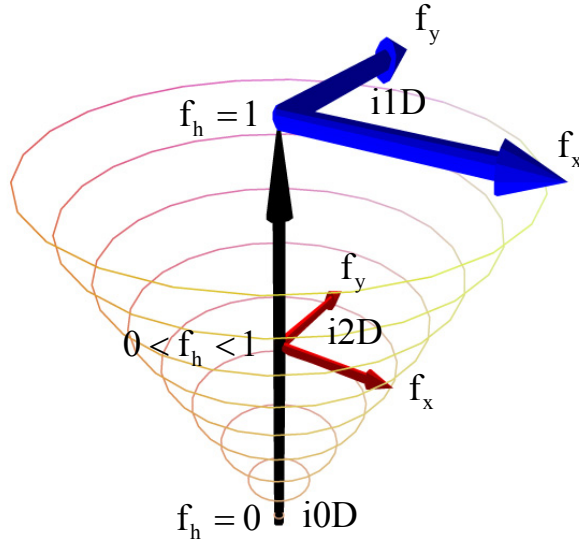


Figure 4.6.: This figure illustrates the relation of all intrinsic dimensions to the homogeneous signal component  $f_h$  in one continuous space. All i0D signals are located at the focal point  $[0, 0, 0]^T$  of the cone with  $f_h = 0$ . All i1D signals are located at the 2D subspace with the homogeneous coordinate  $f_h = 1$ . Any i2D signal is characterized by a homogeneous coordinate  $0 < f_h < 1$ . Therefore, the i0D signals are on a point of singularity, the i1D signals can be represented by a 2D plane and the i2D signals exist in a 3D volume.

In the case of 2D image signals, this approach is designed for an isotropic analysis of lines, edges, corners and junctions in one framework.

The important generalization from i1D signal analysis to 2D signal analysis is, that in contrast to the 2D monogenic signal, here the 2D conjugate Poisson components  $[f_x, f_y]^T$  are in a natural way located in the higher dimensional 3D projective space  $[f_x, f_y, f_h]^T$  with  $f_h$  as the additional homogeneous component, see Figure (4.5). Signal analysis naturally reduces now to the normalization of the homogeneous component to one, see Figure (4.6). This can easily be done by multiplying the conjugate Poisson signal components  $f_x$  and  $f_y$  by  $f_h^{-1}$ . In other words: The 2D space spanned by the components  $f_x$  and  $f_y$  is extended by the homogeneous component  $f_h$  which is determined by the geometric information delivered by the apex angle.

### Generalized Phase Vector

Analogously, the 2D phase vector  $\Phi_{2D}$  of the 2D monogenic signal can now be generalized to the 3D phase vector  $\Phi_{3D} \in \mathbb{R}^3$  of the 2D analytic signal, which is defined as

$$\Phi_{3D} = \begin{bmatrix} \Phi_x \\ \Phi_y \\ \Phi_z \end{bmatrix} = \phi \begin{bmatrix} \cos \theta \\ \sin \theta \cos \alpha \\ \sin \theta \sin \alpha \end{bmatrix} \quad (4.163)$$

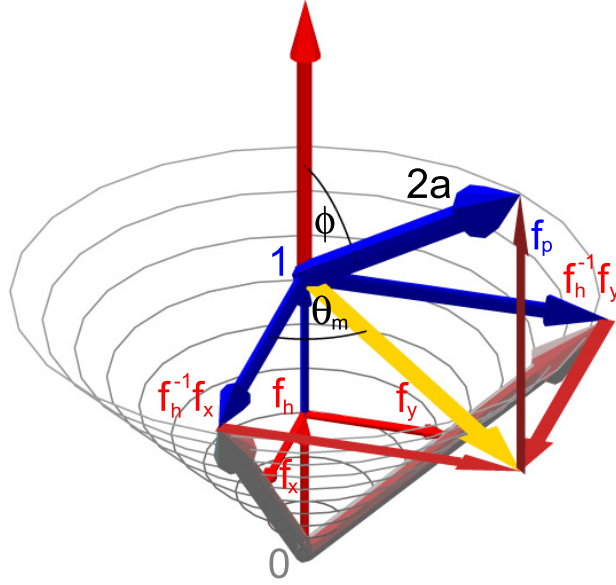


Figure 4.7.: Geometric interpretation of phase  $\phi$ , amplitude  $a$  and main orientation  $\theta_m$  in projective space of i1D and i2D signals in one unified framework.

consisting of the rotationally invariant local apex angle  $\alpha$ , the local main orientation  $\theta$  and the local i1D/i2D phase  $\phi$ . In the case of an i1D signal where the apex angle is zero, the 3D phase vector naturally degrades to the phase vector of the 2D monogenic signal.

#### 4.4.4. Proof Outline

Due to the previous results of the first and second order generalized Hilbert transform expressed in Radon space the proofs can now be done by trigonometric calculations using the known local signal components (see also Figure (4.7))

$$\begin{bmatrix} f_x \\ f_y \\ f_0 \\ f_+ \\ f_{+-} \end{bmatrix} = a \begin{bmatrix} [\cos \theta_1 + \cos \theta_2] \sin \phi \\ [\sin \theta_1 + \sin \theta_2] \sin \phi \\ \cos \phi \sin \phi \\ \frac{1}{2} [\sin(2\theta_1) + \sin(2\theta_2)] \cos \phi \\ \frac{1}{2} [\cos(2\theta_1) + \cos(2\theta_2)] \cos \phi \end{bmatrix} \quad (4.164)$$

#### 4. The Isotropic 2D Analytic Signal

consisting of five linear independent components which result from the signal intelligence in Radon space. From which follows that

$$\begin{aligned} f_+ &= a \cos \phi \cos(\theta_1 - \theta_2) \sin(\theta_1 + \theta_2) , \\ f_{+-} &= a \cos \phi \cos(\theta_1 - \theta_2) \cos(\theta_1 + \theta_2) , \\ f_x &= 2a \sin \phi \cos \frac{\theta_1 - \theta_2}{2} \cos \frac{\theta_1 + \theta_2}{2} , \\ f_y &= 2a \sin \phi \cos \frac{\theta_1 - \theta_2}{2} \sin \frac{\theta_1 + \theta_2}{2} \end{aligned}$$

and

$$q = \sqrt{f_x^2 + f_y^2} = 2a \sin \phi \cos \frac{\theta_1 - \theta_2}{2} \quad (4.165)$$

from which follows for the main orientation  $\theta = \frac{\theta_1 + \theta_2}{2}$  that

$$\cos \theta = \frac{f_x}{\sqrt{f_x^2 + f_y^2}} , \quad (4.166)$$

$$\sin \theta = \frac{f_y}{\sqrt{f_x^2 + f_y^2}} . \quad (4.167)$$

Furthermore,

$$a \cos \phi \cos(\theta_1 - \theta_2) = \sqrt{f_+^2 + f_{+-}^2} \quad (4.168)$$

from which follows for the apex angle  $\alpha$  that

$$\cos \alpha = \sqrt{\left[\frac{f_+}{f_0}\right]^2 + \left[\frac{f_{+-}}{f_0}\right]^2} \quad (4.169)$$

and

$$\sin \alpha = \sqrt{1 - \left[\frac{f_+}{f_0}\right]^2 - \left[\frac{f_{+-}}{f_0}\right]^2} . \quad (4.170)$$

Note that the relation to the Radon transform is required solely for interpretation and theoretical results. Neither the Radon transform nor its inverse are ever applied to the signal in practice. Instead, the generalized Hilbert transformed signal components will be determined by 2D convolutions with the generalized Hilbert transform kernels in the spatial domain.

### 4.5. Experimental Results and Comparisons

The 2D monogenic signal and the isotropic 2D analytic signal will be applied to the synthetic signals shown in Figure (4.8). The synthetic 1D signals are modeled by

$$f = a \cos(x \cos \theta + y \sin \theta + \phi) \quad (4.171)$$



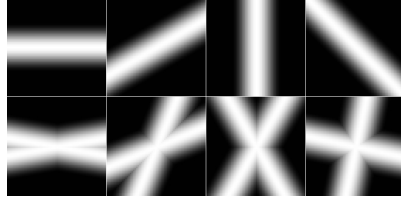


Figure 4.8.: Test signals consisting of lines/edges and x-junctions. The experimental results are shown in Figure (4.9).

with constant amplitude  $a$ , with constant phase  $\phi$  and with constant orientation  $\theta$ . The resulting local orientation is constant up to  $\theta + k\pi$  with  $k \in \mathbb{Z}$  since orientation is not uniquely defined in 2D signal domains. The apex angle of the pure i1D signal is zero. The synthetic i2D signal is modeled by

$$f = \sum_{i=1}^2 a \cos(x \cos \theta_i + y \sin \theta_i + \phi) \quad (4.172)$$

with constant amplitude  $a$ , with constant phase  $\phi$  and with constant orientations  $\theta_1$  and  $\theta_2$ . The resulting local main orientation is constant up to  $\theta + k\pi$  with  $k \in \mathbb{Z}$  since orientation is not uniquely defined in 2D signal domains. The apex angle of the pure i2D signal is constant. The results of the local phase depend on the position in the spatial domain and the amplitude should be constant.

In the following the 2D analytic signal and the 2D monogenic signal [16] will be applied to synthetic signals for comparison and qualitative results. Figure (4.9) illustrates the experimental results with known ground truth data (amplitude, phase, and orientation) of the 2D monogenic signal. The estimated features are plotted with fixed orientation and fixed amplitude against varying phase  $0 \leq \phi \leq 180^\circ$  and varying apex angle  $0 \leq \alpha \leq 90^\circ$ .

In the following the experimental results of the 2D monogenic signal are being discussed from left to right. The orientation can be determined exactly except for the phases  $\phi = 0^\circ$  and  $\phi = 180^\circ$ . The amplitude is disturbed even in case of i1D signals, i.e. at zero apex angle, and should be globally constant like the results of the isotropic 2D analytic signal below. The phase errors increase with increasing apex angle. In the ideal case the result should look like the plane delivered by the isotropic 2D analytic signal. These results show that in contrast to the isotropic 2D analytic signal, the amplitude and phase of the 2D monogenic signal produce significant errors. It is very important to mention that the isotropic 2D analytic signal performs also in case of finite i1D signals better than the 2D monogenic signal although in theory for zero apex angle both signals are the same. But for finite signals the local apex angle is never totally zero since the i1D signal slice in 2D Radon space is always broadened, see Figure (2.1). This broadness will be detected by the 2D analytic signal automatically resulting in an apex angle greater than zero in contrast to the 2D monogenic signal which ignores this feature by assuming a zero apex angle.

Analogously to the results of the 2D monogenic signal the experimental results of the

#### 4. The Isotropic 2D Analytic Signal

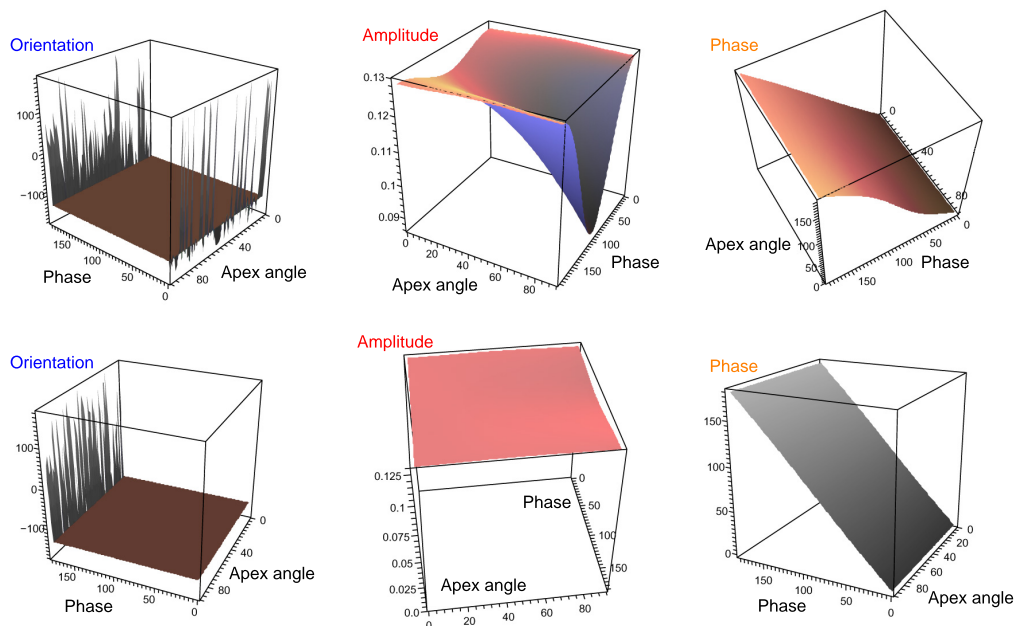


Figure 4.9.: Comparison of the results delivered by the 2D monogenic signal (top row) and the results delivered by the isotropic 2D analytic signal (bottom row) applied to the test signals shown in Figure (4.8). From left to right: local orientation, local amplitude and local phase results. Convolution mask size in spatial domain:  $7 \times 7$  pixels. Coarse scale space parameter:  $s_c = 0.2$ , and fine scale space parameter:  $s_f = 0.1$ .

isotropic 2D analytic signal are illustrated in the bottom row of Figure (4.9) with same experimental settings. The estimated apex angle for varying phase and varying apex angle is shown in Figure (4.10). The apex angle can be determined exactly by the isotropic 2D analytic signal. From left to right in the bottom row of Figure (4.9): estimated orientation for varying phase and varying apex angle but fixed signal orientation and fixed signal amplitude. The orientation can be determined exactly except for the phase singularity  $\phi = 180^\circ$ . Second plot from left to right: estimated amplitude for varying phase and varying apex angle but fixed signal amplitude. The amplitude can be determined exactly as a constant value. Third plot: estimated phase for varying phase and varying apex angle. The phase can be determined exactly by the isotropic 2D analytic signal.

### 4.6. Application: Dense Optical Flow Estimation

The isotropic 2D analytic signal is an ideal substitute for the partial Hilbert transform [31], the 2D monogenic signal [16] and for all applications which make use of derivatives (e.g. the Laplacian) in detection of local features, e.g. texture analysis, layer decomposition and vessel detection in medical image processing. In optical flow applications the intensity or the mostly used gradient constancy constraint can easily be replaced by the

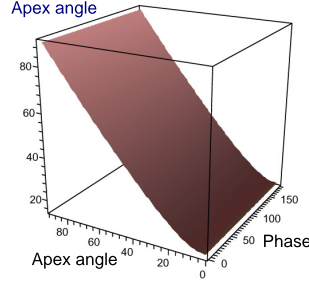


Figure 4.10.: Experimental results of the estimated apex angle by the isotropic 2D analytic signal approach. Convolution mask size in spatial domain:  $7 \times 7$  pixels. Coarse scale space parameter:  $s_c = 0.2$ , and fine scale space parameter:  $s_f = 0.1$ .

2D analytic signal phase vector  $\Phi_{3D} \in \mathbb{R}^3$

$$\Phi_{3D} = \begin{bmatrix} \Phi_x \\ \Phi_y \\ \Phi_z \end{bmatrix} = \phi \begin{bmatrix} \cos \theta \\ \sin \theta \cos \alpha \\ \sin \theta \sin \alpha \end{bmatrix} \quad (4.173)$$

consisting of the rotationally invariant local apex angle  $\alpha$ , the local main orientation  $\theta$  and the local i1D/i2D phase  $\phi$  with scale space parameter  $s$  to minimize the resulting nonlinear energy functional [8]

$$E(w) = \int_{z \in \Omega} \underbrace{\lambda \Psi(\|\nabla u(z)\|^2 + \|\nabla v(z)\|^2)}_{\text{Smoothness term}} + \underbrace{\sum_{\iota \in \{x,y,z\}} \Psi(\|\Phi_\iota(z + w(z), s) - \Phi_\iota\|^2)}_{\text{Data term}} dz \quad (4.174)$$

with  $z = (x, y)$ , the unknown optical flow

$$w(z) = [u(z), v(z)]^T, \quad (4.175)$$

$\lambda > 0$  as a weighting factor of the smoothness term and

$$\Psi(s^2) = \sqrt{s^2 + \epsilon^2} \quad (4.176)$$

as a penalizing function for a small constant  $\epsilon$ . Results of the gradient [48] versus the phase vector are presented in Table (4.3). The advantage of the phase vector is the invariance against global and local illumination change and the robustness against noise, see Figures (5.13) and (5.12).

#### 4. The Isotropic 2D Analytic Signal

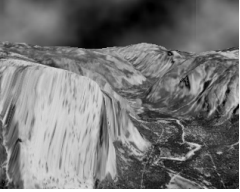
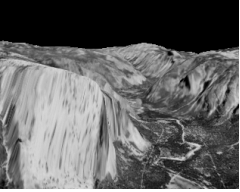


Picture	Scenario	[48]	$\Phi_{3D}$	$\Phi_{2D}$	$\nabla$
	Cloudy Yosemite	2.44°	1.77°	2.11°	2.39°
	Yosemite	1.64°	0.91°	1.33°	1.60°
	Street	4.93°	4.10°	4.55°	4.87°
	Marble	4.74°	3.98°	4.47°	4.81°

Table 4.3.: Comparison of the average angular error (AAE) [48] of the classical gradient  $\nabla$ , the phase vector  $\Phi_{2D}$  of the 2D monogenic signal and the phase vector  $\Phi_{3D}$  of the 2D analytic signal used as the constancy constraint for dense optical flow estimation.

# 5. The Multi-Vector Signal

We will now introduce a generalization of the isotropic 2D analytic signal shown in the previous chapter by the so called multi-vector signal for two-dimensional signals [65, 70]. The first step of low level signal analysis is the designation of a reasonable signal model. Based on the fact that signals  $f \in L^2(\Omega, \mathbb{R}) \cap L^1(\Omega, \mathbb{R})$  with  $\Omega \subseteq \mathbb{R}^2$  can be decomposed into their corresponding Fourier series, we assume that each frequency component of the original image signal consists locally of a superposition of intrinsically 1D (i1D) [78] signals  $f_\nu$  with  $z = (x, y) \in \mathbb{R}^2$ , see Equation (5.1). Each of them is determined by its individual amplitude  $a_\nu \in \mathbb{R}$ , phase  $\phi_\nu \in [0, \pi)$ , and orientation  $\theta_\nu \in [0, \pi)$ . The Poisson scale space is naturally related to the generalized Hilbert transform by the Cauchy kernel [13].

## 5.1. Local Signal Modeling in Scale Space

Applying the Poisson filter kernel  $p_s$  to the original signal  $f$  results in the smoothed local signal model

$$\mathcal{P}_s\{f\}(z) = \sum_{\nu=1}^n a_\nu \cos(\langle z, \bar{o}_\nu \rangle + \phi_\nu) \quad (5.1)$$

with  $\bar{o}_\nu = [\cos \theta_\nu, \sin \theta_\nu]^T$  as the oriented normal,  $\langle \cdot, \cdot \rangle$  as the inner product. This local signal model allows modeling any texture or structure such as lines, edges, corners, and junctions in scale space, see Figure (5.2). After having specified the signal model, the mathematical task is the exact retrieval of the signal parameters  $(\theta_\nu, \phi_\nu, a_\nu)$  for every position  $z \in \Omega$  and for every scale space parameter  $s > 0$ . In the following

$$f_\nu^e = a_\nu \cos \phi_\nu \quad (5.2)$$

will be called the even signal part. Furthermore and without loss of generality, at the origin  $z = (x, y)$  of the applied local coordinate system, the assumed signal model in Equation (5.1) results in

$$f_p = \mathcal{P}_s\{f\}(z) = (p_s * f)(z) = \sum_{\nu=1}^n a_\nu \cos \phi_\nu, \quad (5.3)$$

with  $*$  as the convolution operator. Since the geometrical information  $\theta_\nu$  is not coded in the signal value  $f_p$ , an appropriate signal extension is necessary.

## 5.2. Signal Extension by Hilbert Transforms

The problem, which has to be solved now, is the search for all unknown structural parameters  $a_\nu \in \mathbb{R}$  and  $\phi_\nu \in [0, \pi)$  and the unknown geometric parameters  $\theta_\nu \in [0, \pi)$ . Although the most general formulas will be provided in this thesis, we will restrict the signal model in Equation (5.1) to  $n \leq 2$ , since by this restriction most signal structures can be modeled [15]. As the signal parameters are unknown, we have to solve a nontrivial inverse problem [68]. This can only be done by extending the original signal to result in a system of equations, which includes all unknown signal parameters. This will be done by the generalized Hilbert transforms of higher orders. Our restriction of the signal model to two superimposed 1D signals results in six degrees of freedom, which require generalized Hilbert transforms up to order three. The first order generalized Hilbert transform convolution kernels for any dimension read [12]

$$h^{(1)}(z) = \begin{bmatrix} h_{z_1}^{(1)} \\ \vdots \\ h_{z_m}^{(1)} \end{bmatrix} (z) = \frac{2}{A_{m+1} \|z\|^{m+1}} \begin{bmatrix} z_1 \\ \vdots \\ z_m \end{bmatrix}, \quad z \in \mathbb{R}^m \quad (5.4)$$

with the area of the unit sphere  $\mathbb{S}^m$  in  $\mathbb{R}^{m+1}$

$$A_{m+1} = \frac{2 \pi^{\frac{m+1}{2}}}{\Gamma\left(\frac{m+1}{2}\right)} \quad (5.5)$$

with  $\Gamma$  as the Gamma function<sup>1</sup>. For two-dimensional signals ( $m = 2$ ) the generalized Hilbert transform kernels read

$$\begin{bmatrix} h_x^{(1)} \\ h_y^{(1)} \end{bmatrix} (z) = \frac{1}{2\pi \|z\|^3} \begin{bmatrix} x \\ y \end{bmatrix} \quad (5.6)$$

which are the analogues to the first order partial derivatives. Since we have to analyze the original signal in scale space, it will be of advantage to provide one unified convolution kernel, which consists of the Poisson kernel and the generalized Hilbert transform kernel of order  $n$ . The generalized Hilbert transform of order  $(i + j)$  in Poisson scale space reads

$$q_{x^i y^j}^{(i+j)} = \underbrace{(h_x^{(1)} * \dots * h_x^{(1)})}_i * \underbrace{(h_y^{(1)} * \dots * h_y^{(1)})}_j * p_s(z) \quad (5.7)$$

which are shown for  $i, j \leq 3$  in Figure (5.1). The value of the  $(i + j)$ th order Hilbert transformed signal in Poisson scale space will be derived by convolution in the spatial domain

$$f_{x^i y^j} = \left( q_{x^i y^j}^{(i+j)}(\cdot, s) * f \right) (z) \quad (5.8)$$

for  $i, j \in \mathbb{N}$ . Note that for all equations and without loss of generality  $z$  always denotes the test point.

<sup>1</sup>The Gamma function is defined by  $\Gamma(x) = \int_{t \in \mathbb{R}} t^{x-1} e^{-t} dt$  for  $x > 0$  and satisfies the functional equation  $\Gamma(x) = (x-1)\Gamma(x-1)$  with the condition  $\Gamma(1) = 1$ .

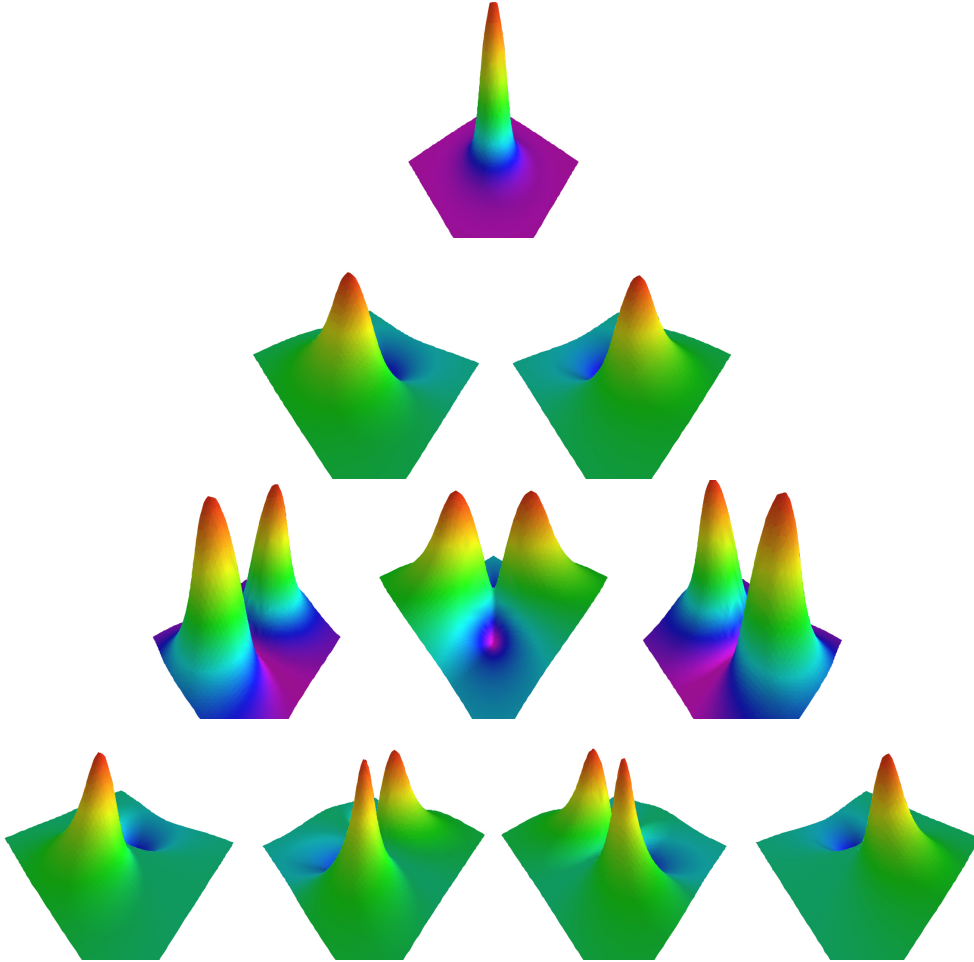


Figure 5.1.: Illustration from left to right of the 2D convolution kernels of the generalized higher order Hilbert transforms in Poisson scale space for a certain scale space parameter  $s > 0$ . Top row: Poisson kernel  $p_s$ . Second row: first order kernels  $q_x^{(1)}$  and  $q_y^{(1)}$ . Third row: second order kernels  $q_{xx}^{(2)}$ ,  $q_{xy}^{(2)}$  and  $q_{yy}^{(2)}$ . Bottom row: third order kernels  $q_{xxx}^{(3)}$ ,  $q_{xxy}^{(3)}$ ,  $q_{xyy}^{(3)}$  and  $q_{yyy}^{(3)}$ .

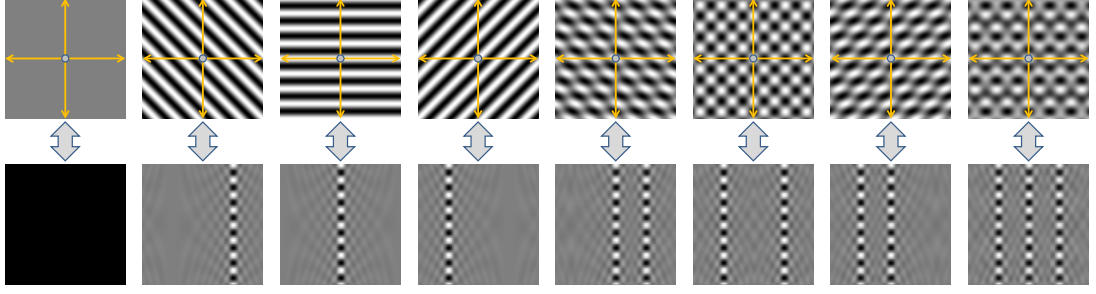


Figure 5.2.: Top row: illustration of all elements of the powerset of three superimposed intrinsically 1D signals in the spatial domain. From left to right: one constant signal (i0D), three i1D signals with orientation  $45^\circ$ ,  $90^\circ$  and  $135^\circ$  followed by four i2D signals which consist of superimposed i1D signals. In case of i2D signals the single orientations can hardly be separated in the spatial domain. This can be done much easier in their corresponding Radon domain which is shown in the bottom row.

### 5.3. Signal Intelligence in Radon Space

After extending the original signal the generalized Hilbert transformed signal must be interpreted. This can be done in Radon space [66]. The original signal  $f$  transformed into Radon space  $f_r = \mathcal{R}\{f\}$  reads

$$f_r(t, \theta, s) = \int_{z \in \mathbb{R}^2} \mathcal{P}_s\{f\}(z) \delta(\langle z, \bar{o} \rangle - t) dz \quad (5.9)$$

with  $\bar{o} = [\cos \theta, \sin \theta]^T$  as the orientated normal vector,  $\theta \in [0, \pi)$  as the orientation,  $t \in \mathbb{R}$  as the minimal distance of the parameterized line to the origin of the local coordinate system of the test point, and  $\delta$  as the Dirac distribution, see Figures (5.4), and (5.2). The corresponding inverse Radon transform  $\mathcal{R}^{-1}\{(t, \theta) \mapsto f_r\}$  exists and can be simplified to the following relation for a finite number  $n$  of superimposed i1D signals

$$\begin{aligned} \mathcal{R}^{-1}\{(t, \theta) \mapsto f_r\}(z) &= \frac{1}{2\pi^2} \int_{\theta \in [0, \pi)} \text{P.V.} \int_{t \in \mathbb{R}} \frac{\frac{\partial}{\partial t} f_r(t, \theta, s)}{\langle z, \bar{o} \rangle - t} dt d\theta \\ &= \frac{1}{2\pi^2} \int_{\theta \in [0, \pi)} \text{P.V.} \int_{t \in \mathbb{R}} \frac{\frac{\partial}{\partial t} f_r(t, \theta, s)}{-t} dt d\theta \\ &= -\frac{1}{2\pi} \sum_{\nu=1}^n \text{P.V.} \int_{t \in \mathbb{R}} \frac{1}{\pi t} \frac{\partial}{\partial t} f_r(t, \theta_\nu, s) dt \\ &= -\frac{1}{2\pi} \sum_{\nu=1}^n \frac{\partial}{\partial t} [(h * f_r(\cdot, \theta_\nu, s))(t)] \end{aligned} \quad (5.10)$$



at position  $z = (x, y)$  for the origin of the applied local coordinate system, see Figure (2.4). The  $(i + j)$ th order generalized Hilbert transformed signal can be expressed in Radon space, which delivers a system of equations including all unknown signal parameters. This thesis shows, that this system of equations can be solved, which was up to now only possible for  $n = 1$  in Equation (5.1) and for  $n = 2$  for the special case of orthogonal superimposed 1D signals [15]. The Hilbert transformed signal can be expressed by

$$f_{x^i y^j} = \mathcal{R}^{-1} \left\{ (t, \theta) \mapsto [\cos^i \theta \sin^j \theta] (h^{(i+j)} * f_r(\cdot, \theta, s))(t) \right\} (z), \quad (5.11)$$

Proof: Fourier slice theorem [66]. The classical one dimensional Hilbert transform kernel  $h^{(m)} : \mathbb{R} \mapsto \mathbb{R}$  of order  $m$  [31] reads

$$h^{(m)}(t) = \begin{cases} \delta(t), & m \bmod 4 = 0 \\ \frac{1}{\pi t}, & m \bmod 4 = 1 \\ -\delta(t), & m \bmod 4 = 2 \\ -\frac{1}{\pi t}, & m \bmod 4 = 3 \end{cases} \quad (5.12)$$

with  $\delta$  as the Dirac distribution, which is the algebraically neutral element of the convolution. Finally, the  $(i + j)$ th Hilbert transformed signal results in

$$f_{x^i y^j} = \sum_{\nu=1}^n [\cos^i \theta_\nu \sin^j \theta_\nu] f_\nu^{(i+j)} \quad (5.13)$$

because of the very important property

$$\frac{\partial}{\partial t} [(h * f_r(\cdot, \theta, s))(t)] = (h * \frac{\partial}{\partial t} f_r(\cdot, \theta, s))(t) \quad (5.14)$$

and the linearity of the inverse Radon transform [66]. The odd signal part

$$f_\nu^o = (h^{(1)} * f_\nu^e)(\phi_\nu) = a_\nu \sin \phi_\nu \quad (5.15)$$

results of the even signal part  $f_\nu^e = a_\nu \cos \phi_\nu$  by the classical 1D Hilbert transform and

$$f_\nu^{(m)} = \begin{cases} f_\nu^e, & m \bmod 4 = 0 \\ f_\nu^o, & m \bmod 4 = 1 \\ -f_\nu^e, & m \bmod 4 = 2 \\ -f_\nu^o, & m \bmod 4 = 3 \end{cases}. \quad (5.16)$$

In case of the zeroth order Hilbert transform, i.e.  $i + j = 0$ , this results in the local signal value  $f_p$ . According to Equation (5.13), the first and second order Hilbert transformed signals determine the following systems of linear equations

$$\begin{bmatrix} f_x \\ f_y \end{bmatrix} = \sum_{\nu=1}^n \begin{bmatrix} \cos \theta_\nu \\ \sin \theta_\nu \end{bmatrix} f_\nu^o \quad (5.17)$$

## 5. The Multi-Vector Signal

$$T = \left( \begin{bmatrix} \text{img1} & \text{img2} \\ \text{img3} & \text{img4} \end{bmatrix} + \begin{bmatrix} \text{img5} & \text{img6} \\ \text{img7} & \text{img8} \end{bmatrix} \mathbf{i} + \begin{bmatrix} \text{img9} & \text{img10} \\ \text{img11} & \text{img12} \end{bmatrix} \mathbf{j} \right) * f$$

Figure 5.3.: Illustration of the convolution kernels in the spatial domain of the quaternion-valued matrix signal representation  $T$ .

and

$$\begin{bmatrix} f_{xx} \\ f_{xy} \\ f_{yy} \end{bmatrix} = \sum_{\nu=1}^n \begin{bmatrix} \cos^2 \theta_{\nu} \\ \cos \theta_{\nu} \sin \theta_{\nu} \\ \sin^2 \theta_{\nu} \end{bmatrix} f_{\nu}^e \quad (5.18)$$

from which the signal value can be reconstructed by

$$f_p = \sum_{\nu=1}^n f_{\nu}^e = f_{xx} + f_{yy} . \quad (5.19)$$

Note, that from Equation (5.80) for the second order derivative operator follows for the second order Hilbert transforms

$$\sin \theta_1 \sin \theta_2 f_{xx} - \sin (\theta_1 + \theta_2) f_{xy} + \cos \theta_1 \cos \theta_2 f_{yy} = 0 . \quad (5.20)$$

With Equation (5.13), the third order generalized Hilbert transformed signal determines the following system of linear equations

$$\begin{bmatrix} f_{xxx} \\ f_{xxy} \\ f_{xyy} \\ f_{yyy} \end{bmatrix} = \sum_{\nu=1}^n \begin{bmatrix} \cos^3 \theta_{\nu} \\ \cos^2 \theta_{\nu} \sin \theta_{\nu} \\ \cos \theta_{\nu} \sin^2 \theta_{\nu} \\ \sin^3 \theta_{\nu} \end{bmatrix} f_{\nu}^o \quad (5.21)$$

from which the first order generalized Hilbert transform can be reconstructed by

$$\begin{bmatrix} f_x \\ f_y \end{bmatrix} = \begin{bmatrix} f_{xxx} + f_{xyy} \\ f_{xxy} + f_{yyy} \end{bmatrix} . \quad (5.22)$$

Due to the important relation of the Radon transform to the generalized Hilbert transform of any order, it is possible to result in a system of equations which can be solved for the unknown signal parameters. Please note, that neither the Radon transform nor its inverse are ever applied to the signal in practise.

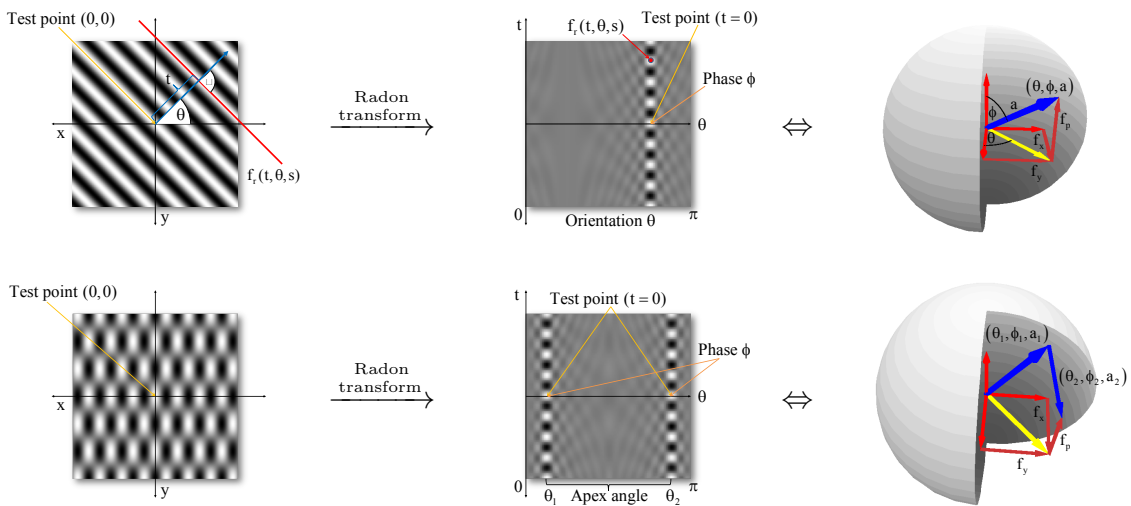


Figure 5.4.: Top row from left to right: illustration of an intrinsically 1D signal in the spatial domain, in its corresponding Radon domain, and its geometric feature interpretation by spherical coordinates  $(\theta, \phi, a)$ . Bottom row from left to right: two superimposed intrinsically 1D signals in the spatial domain modeling locally a junction. In their corresponding Radon space the two signals are separated from each other into two individual 1D signal slices. The corresponding geometric feature interpretation corresponds to the sum of two vectors with spherical coordinates  $(\theta_\nu, \phi_\nu, a_\nu)$  for  $\nu \in \{1, 2\}$ .

## 5.4. Algebraic Signal Representation

Derivative based signal extensions are normally structured in matrix form or in tensor form. We now introduce a signal representation in the so called multi-vector form, which comes from the field of geometric algebra [49]. Recent results of the hybrid matrix geometric algebra [53] offer geometric interpretation, which in our case enables the complete signal analysis by mapping tensor structures to multi-vectors. For the sake of simplicity, we will restrict the representative algebra to the well known algebra of the quaternions  $\mathbb{H} \cong \mathbb{R}_3^+$ , which is solely needed for constructing the signal tensor. Loosely spoken, simply consider the tensor-valued signal extension as a real-valued  $2 \times 2 \times 3$  array. According to [53], a mapping from the quaternion-valued tensor with elements in  $\mathbb{R}_3$

$$T = T^e + T_x^o \mathbf{i} + T_y^o \mathbf{j} \in M(2, \mathbb{R}_3) \quad (5.23)$$

to the quaternion-valued vector with elements in  $\mathbb{R}_{4,1}$

$$\varphi(T) = \varphi(T^e) + \varphi(T_x^o) \mathbf{i} + \varphi(T_y^o) \mathbf{j} \in \mathbb{R}_{4,1} \quad (5.24)$$

is possible. With the set of basis vectors

$$\{1, \mathbf{i}, \mathbf{j}, \mathbf{k}\} \quad (5.25)$$

of the quaternions  $(\mathbb{H}, +, \circ)$  with

$$\mathbb{H} = \{q_s + q_i \mathbf{i} + q_j \mathbf{j} + q_k \mathbf{k} : q_s, q_i, q_j, q_k \in \mathbb{R}\} \quad (5.26)$$

and the isomorphisms

$$\mathbf{i} \cong \mathbf{e}_{13}, \mathbf{j} \cong \mathbf{e}_{23}, \mathbf{k} \cong \mathbf{e}_{21} \quad (5.27)$$

with  $\mathbf{i} \circ \mathbf{j} = \mathbf{k}$ , the signal tensor for  $n < 3$  in Equation (5.1) can be defined by the generalized Hilbert transforms of second order ( $T^e$ ) and third order ( $T_x^o$  and  $T_y^o$ )

$$T = \underbrace{\begin{bmatrix} f_{xx} & f_{xy} \\ f_{xy} & f_{yy} \end{bmatrix}}_{T^e} + \underbrace{\begin{bmatrix} f_{xxx} & f_{xxy} \\ f_{xxy} & f_{xyy} \end{bmatrix}}_{T_x^o} \mathbf{i} + \underbrace{\begin{bmatrix} f_{xxy} & f_{xyy} \\ f_{xyy} & f_{yyy} \end{bmatrix}}_{T_y^o} \mathbf{j}, \quad (5.28)$$

see Figure (5.3). By introducing the abbreviations

$$f^- = f_{xx} - f_{yy}, \quad (5.29)$$

$$f_x^- = f_{xxx} - f_{xyy}, \quad (5.30)$$

$$f_y^- = f_{xxy} - f_{yyy} \quad (5.31)$$

with

$$f^- = \sum_{\nu=1}^n \cos(2\theta_\nu) f_\nu^e \quad (5.32)$$

$$\begin{aligned}
 \varphi(T) = & \left( \begin{array}{ccc} \text{img1} & + & \text{img2} \mathbf{e}_+ + \text{img3} \mathbf{e}_{+-} \\ \text{img4} & + & \text{img5} \mathbf{e}_+ + \text{img6} \mathbf{e}_{+-} \end{array} \right) * f \\
 + & \left( \begin{array}{ccc} \text{img7} & + & \text{img8} \mathbf{e}_+ + \text{img9} \mathbf{e}_{+-} \\ \text{img10} & + & \text{img11} \mathbf{e}_+ + \text{img12} \mathbf{e}_{+-} \end{array} \right) \mathbf{i} * f \\
 + & \left( \begin{array}{ccc} \text{img13} & + & \text{img14} \mathbf{e}_+ + \text{img15} \mathbf{e}_{+-} \\ \text{img16} & + & \text{img17} \mathbf{e}_+ + \text{img18} \mathbf{e}_{+-} \end{array} \right) \mathbf{j} * f
 \end{aligned}$$

Figure 5.5.: Illustration of the convolution kernels in the spatial domain of the multi-vector signal  $\varphi(T)$  which is defined in Equation (5.33).

the quaternion-valued matrix  $T$  can be mapped by the isomorphism  $\varphi$  to a quaternion-valued multi-vector representation [66] in conformal space  $\mathbb{R}_{4,1}$  [49]

$$\varphi(T) = \varphi(T^e) + \varphi(T_x^o)\mathbf{i} + \varphi(T_y^o)\mathbf{j} \quad (5.33)$$

with

$$\varphi(T^e) = \frac{f_p}{2} + f_{xy}\mathbf{e}_+ + \frac{f^-}{2}\mathbf{e}_{+-}, \quad (5.34)$$

$$\varphi(T_x^o) = \frac{f_x}{2} + f_{xxy}\mathbf{e}_+ + \frac{f_x^-}{2}\mathbf{e}_{+-}, \quad (5.35)$$

$$\varphi(T_y^o) = \frac{f_y}{2} + f_{xyy}\mathbf{e}_+ + \frac{f_y^-}{2}\mathbf{e}_{+-} \quad (5.36)$$

which will be called multi-vector signal<sup>2</sup>, see Figure (5.5). The multi-vector signal delivers the complete geometrical and structural information of the assumed signal model in Equation (5.1). In [11] the geometrical signal features have been retrieved by higher order derivatives in the traditional matrix expression. This will be generalized by  $\varphi(T)$  in a more natural embedding.

<sup>2</sup>Compare the multi-vector signal with the structure multi-vector [15], and the more common Weyl-projection operator [62] induced by  $(\mathcal{H}^{(1)}\{(p_s * f)\}, \mathcal{H}^{(2)}\{(p_s * f)\}, \mathcal{H}^{(3)}\{(p_s * f)\})$ . Compared to the structure multi-vector the multi-vector signal has less restrictions concerning the signal model. And compared to the Weyl-projection the multi-vector signal is an alternative.

## 5.5. Geometry from the Multi-Vector Signal

The first step of this signal analysis problem is to obtain the exact geometrical signal features such as the orientations  $\theta_\nu$  from the analysis of the multi-vector signal. We will show that this information can be retrieved from the odd part of the signal tensor by using basic operations of the geometric algebra. Therefore, we define the tensor parts in multi-vector form as

$$t^e = \mathbf{e}_-\varphi(T^e) \in \mathbb{R}_{4,1}, \quad (5.37)$$

$$t_x^o = \mathbf{e}_-\varphi(T_x^o) \in \mathbb{R}_{4,1}, \quad (5.38)$$

$$t_y^o = \mathbf{e}_-\varphi(T_y^o) \in \mathbb{R}_{4,1}. \quad (5.39)$$

By the application of the geometric product  $\circ$  and the grade-0 projection  $\langle \cdot \rangle_0$  [49] we define four real numbers by the Minkowski inner product

$$\varepsilon = -\langle t^e \circ t^e \rangle_0 \in \mathbb{R}, \quad (5.40)$$

$$\delta = -\langle t_x^o \circ t_x^o \rangle_0 \in \mathbb{R}, \quad (5.41)$$

$$\beta = -\langle t_y^o \circ t_y^o \rangle_0 \in \mathbb{R}, \quad (5.42)$$

$$\alpha = -\langle t_x^o \circ t_y^o \rangle_0 \in \mathbb{R}, \quad (5.43)$$

which read

$$\varepsilon = \left[ \frac{f_p}{2} \right]^2 - f_{xy}^2 - \left[ \frac{f^-}{2} \right]^2, \quad (5.44)$$

$$\delta = \left[ \frac{f_x}{2} \right]^2 - f_{xxy}^2 - \left[ \frac{f_x^-}{2} \right]^2, \quad (5.45)$$

$$\beta = \left[ \frac{f_y}{2} \right]^2 - f_{xyy}^2 - \left[ \frac{f_y^-}{2} \right]^2, \quad (5.46)$$

$$\alpha = \frac{f_x f_y}{2} - f_{xxy} f_{xyy} - \frac{f_x^- f_y^-}{2}. \quad (5.47)$$

Please note the relation to the determinants of the even and two odd tensors:

$$\det(T^e) = \varepsilon \quad (5.48)$$

$$\det(T_x^o) = \delta \quad (5.49)$$

$$\det(T_y^o) = \beta, \quad (5.50)$$

proof: Appendix (C). Note, that  $\alpha$  cannot be expressed in terms of the determinants.

Furthermore, we will use the following abbreviations

$$\gamma^+ = \frac{1}{2}(\delta + \beta) , \quad (5.51)$$

$$\gamma^- = \frac{1}{2}(\delta - \beta) \quad (5.52)$$

from which follows

$$\beta = \gamma^+ - \gamma^- , \quad (5.53)$$

$$\delta = \gamma^+ + \gamma^- . \quad (5.54)$$

Now, we will give the multi-vector signal a geometric sense in terms of its orientation interpretation. Please note, that it is not obvious but it turns out that the geometric interpretation is related to a 3D ellipsoid. Therefore, we define the eccentricity

$$\epsilon_1 = \sqrt{(\gamma^+)^2 - (\gamma^-)^2} , \quad (5.55)$$

$$\epsilon_2 = \sqrt{\alpha^2 - \epsilon_1^2} = \sqrt{\alpha^2 - \beta\delta} = \sqrt{\alpha^2 + (\gamma^-)^2 - (\gamma^+)^2} \quad (5.56)$$

with the relation

$$\epsilon_1 = \sqrt{\beta\delta} \quad (5.57)$$

where  $\epsilon_1, \epsilon_2$  denote the linear eccentricity of a 3D ellipsoid, which is the geometric interpretation model of the multi-vector signal, see Figure (5.6). Note, that in case of i1D signals the ellipsoid degrades to an ordinary sphere with  $\alpha = \epsilon_1$  and  $\epsilon_2 = 0$  which results in an apex angle of zero and therefore in the special case of the i1D analysis of the monogenic signal. Now, the geometric orientation parameters will be determined by this 3D ellipsoid. Due to the basic operations of the geometric algebra, the main orientation can easily be derived by

$$\theta_1 + \theta_2 = \arctan \frac{\alpha}{\gamma^-} , \quad (5.58)$$

proof: see Appendix (A), as well as the apex angle

$$\|\theta_1 - \theta_2\| = \arctan \frac{\epsilon_2}{\gamma^+} , \quad (5.59)$$

proof: see Appendix (A). This result shows that the geometric product solves the calculation of the orientations in two steps. Firstly, calculate the geometric product and afterwards use the real valued entries of the resulting multi-vector to retrieve the orientations. Please note, that this is the most general solution for two superimposed i1D signals with arbitrary amplitudes, phases and orientations. Also note, that the orientations cannot be obtained for phase values equal to zero which is analogously to the analysis of the monogenic signal.

The single orientations  $\theta_\nu$  can be determined by the following formula

$$\theta_{1/2} = \arctan \frac{(\alpha \pm \epsilon_2)^2 + \beta^2}{\delta(\alpha \pm \epsilon_2) + \beta(\alpha \mp \epsilon_2)} \quad (5.60)$$

for phase values  $\phi_\nu \neq 0$ , see Appendix (A).

5. The Multi-Vector Signal

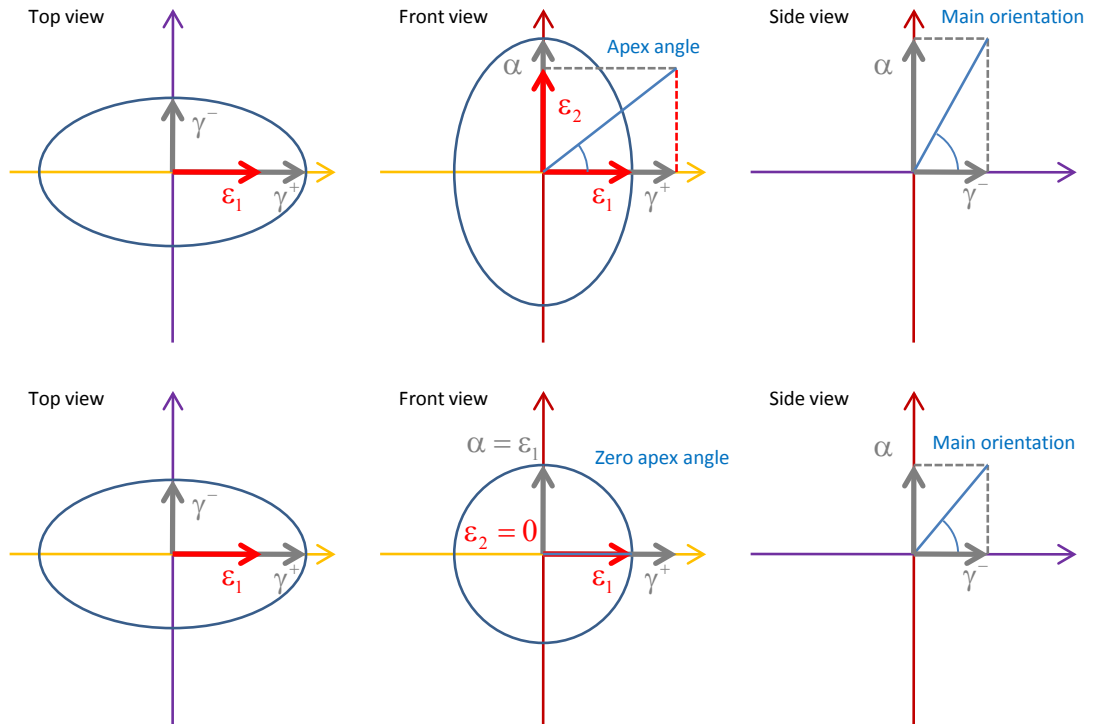


Figure 5.6.: Illustration of the 3D ellipsoid, which will be used to analyze the geometry of the multi-vector signal. Top row shows the general i2D case and the bottom row shows the special i1D case. From left to right: top, front and side view of the 3D ellipsoid, which is spanned by the orthogonal components  $\gamma^+$ ,  $\gamma^-$  and  $\alpha$ .



## 5.6. Structure from the Multi-Vector Signal

The following aim is to obtain the two local phases  $\phi_\nu \in [0, \pi]$  and the two local amplitudes  $a_\nu \geq 0$  of the assumed local signal model. In the following we will use the abbreviation

$$s_\pm = \sin(\theta_1 \pm \theta_2) \quad (5.61)$$

for

$$\frac{1}{s_-^2} = \left(\frac{\gamma^+}{\epsilon_2}\right)^2 + 1. \quad (5.62)$$

From the definition of the even signal part  $f_p = f^e = f_1^e + f_2^e$  and  $\epsilon$  follows the solution for

$$f_\nu^e \in \left\{ \frac{f_p}{2} \pm \sqrt{\left(\frac{f_p}{2}\right)^2 - \frac{\epsilon}{s_-^2}} \right\}, \quad (5.63)$$

proof: see Appendix (B). Furthermore, we will introduce the abbreviation

$$\sigma = \sqrt{\alpha^2 + (\gamma^-)^2} = \sqrt{\epsilon_2^2 + (\gamma^+)^2} \quad (5.64)$$

to solve for the odd part  $f^o = f_1^o + f_2^o \geq 0$  of the signal

$$f^o = \sqrt{f_x^2 + f_y^2 + \frac{4}{s_-^2}(\sigma - \gamma^+)} \quad (5.65)$$

and its odd components

$$f_\nu^o \in \left\{ \frac{f^o}{2} \pm \sqrt{\left(\frac{f^o}{2}\right)^2 - \frac{2\sigma}{s_-^2}} \right\}. \quad (5.66)$$

The correct choice of the even and odd signal components can now be used to determine the single phases

$$\phi_\nu = \arctan \frac{f_\nu^o}{f_\nu^e} \quad (5.67)$$

and the single amplitudes

$$a_\nu = \sqrt{(f_\nu^e)^2 + (f_\nu^o)^2}, \quad (5.68)$$

proof: see Appendix (B).

### 5.6.1. The Multi-Vector Signal Generalizes the 2D Monogenic Signal

In this subsection we want to propose a definition of a main phase  $\phi$  and a main amplitude  $a$  of the superposition of two signals, independently of the signal orientations.

## 5. The Multi-Vector Signal

The sum of the squared amplitudes can be determined by

$$a_1^2 + a_2^2 = f_p^2 + f_x^2 + f_y^2 - \frac{2(\varepsilon + 2\gamma^+)}{s_-^2}, \quad (5.69)$$

proof: see Appendix (B), as well as

$$a_1 a_2 \cos(\phi_1 \pm \phi_2) = \frac{1}{s_-^2} (\varepsilon \mp 2\sigma), \quad (5.70)$$

proof: see Appendix (B). Since the signal  $f_p = f^e$  consists of a superposition of two individual signals, the resulting signal reads

$$f^e = f_1^e + f_2^e = a \cos \phi, \quad (5.71)$$

and its corresponding odd part

$$f^o = f_1^o + f_2^o = a \sin \phi. \quad (5.72)$$

The main phase  $\phi \in [0, \pi]$  can be calculated by

$$\phi = \arctan \frac{f^o}{f^e} = \arctan \frac{\sqrt{f_x^2 + f_y^2 + \frac{4(\sigma - \gamma^+)}{s_-^2}}}{f_p}, \quad (5.73)$$

proof: see Appendix (B), and the main amplitude  $a \geq 0$  can be calculated by

$$a = \sqrt{(f^e)^2 + (f^o)^2} \quad (5.74)$$

$$= \sqrt{a_1^2 + a_2^2 + 2a_1 a_2 \cos(\phi_1 - \phi_2)} \quad (5.75)$$

$$= \sqrt{f_p^2 + f_x^2 + f_y^2 + \frac{4(\sigma - \gamma^+)}{s_-^2}}, \quad (5.76)$$

proof: see Appendix (B). The advantage of this definition of a main phase and main amplitude enables a low dimensional feature space of local points of interest, and defines the generalization of the monogenic signal for i1D and i2D in one unified framework, i.e. in terms of pure i1D signals the derived more general formulas degrade to the formulas of the monogenic signal, since:

$$\lim_{\substack{a_1 \rightarrow a_2 \\ \phi_1 \rightarrow \phi_2 \\ \theta_1 \rightarrow \theta_2}} \frac{4(\sigma - \gamma^+)}{s_-^2} = 0, \quad (5.77)$$

which implies that the general formulas given here degrade to the formulas of the monogenic signal for i1D signal structures.

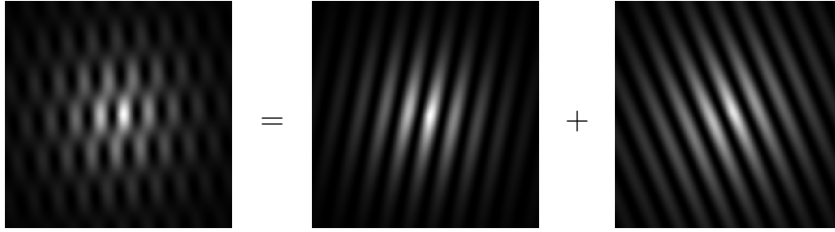


Figure 5.7.: Image layer decomposition. From left to right: original signal which consists of two layers with individual orientation and the resulting decomposition by the multi-vector signal. The superposition will be analyzed at each pixel position and decomposed into its local signal parameters. Using those parameters the two layers can be reconstructed except for their DC-component (mean value).

## 5.7. Applications

The multi-vector signal is isotropic and therefore needs a small set of only seven convolution filters. The multi-vector signal can be implemented either in Fourier space or in the spatial domain. But the advantage of the spatial domain is the local adaption on the individual scale space parameter which carries the important signal information for each test point. Because of that we favor the convolution in the spatial domain. The implementation of the multi-vector signal is very easy and can be calculated in  $O(m)$  with  $m$  as the total convolution mask size. In practice the convolution mask size involves  $7 \times 7$  pixels. Due to the latest developments in graphic controllers, the multi-vector signal can also be implemented directly using the OpenGL<sup>®</sup> Shading Language (GLSL). This enables realtime computation of the multi-vector signal and detecting its optimal scale space parameter by maximizing the local amplitude for each test point individually [15]. Since the multi-vector signal is an isotropic, local, low-level, phase based approach for i1D and i2D signals, many applications can be found. In the following we will present the parameter-free decomposition of multi-layer textures [63] shown in Figure (5.7), and the application in state of the art optical flow approaches.

### 5.7.1. Multi-Layer Decomposition

As an application of the multi-vector signal we will analyze superimposed oriented patterns and compare our results with the derivative based approach presented in [57]. In comparison to [57] our approach does not need any parameter tuning and unifies the case of i1D and i2D signals in one framework.

### Derivative Based Approach

In [57] an i1D signal is assumed at first. An evidence check decides between computation of one single orientation or the double orientation case. The derivative operator for one orientation  $\theta$  reads

$$\mathcal{D}_\theta = \cos \theta \frac{\partial}{\partial x} + \sin \theta \frac{\partial}{\partial y} . \quad (5.78)$$

In the i1D case, the orientation computation is in essence an eigenspace analysis of the tensor  $T = \nabla f \nabla f^T$  computed over a neighborhood  $\Omega$ . The confidence measure for an i1D structure is determined as  $\det(T) \leq \lambda \text{trace}^2(T)$  with the tuning parameter  $\lambda > 0$  which has to be chosen manually. In the i2D case, the comparison in this thesis is restricted to considering superimposed oriented patterns resulting in the model

$$f(z) = \sum_{\nu=1}^2 f_\nu(z) \quad \text{with } z = (x, y) \in \Omega . \quad (5.79)$$

Using the derivative operator from Equation (5.78) and applying it to the double orientation case, the image signal in Gaussian scale space  $\mathcal{G}\{\cdot\}(z; s)$  satisfies the equation

$$\mathcal{D}_{\theta_1} \mathcal{D}_{\theta_2} \mathcal{G}\{f\}(z; s) = c^T \mathcal{D}f = 0 \quad (5.80)$$

with the so called mixed-orientation vector

$$c = [\cos \theta_1 \cos \theta_2, \sin(\theta_1 + \theta_2), \sin \theta_1 \sin \theta_2]^T \quad (5.81)$$

and

$$\mathcal{D}f = \left[ \frac{\partial^2}{\partial x^2}, \frac{\partial^2}{\partial xy}, \frac{\partial^2}{\partial y^2} \right]^T \mathcal{G}\{f\}(z; s) . \quad (5.82)$$

Taking into account that real image signals do not satisfy Equation (5.80) exactly the residual error is defined by

$$\varepsilon(c) = c^T \underbrace{\left[ \int_{z \in \Omega} (\mathcal{D}f)(\mathcal{D}f)^T dz \right]}_J c \quad (5.83)$$

which has to be minimized with respect to the vector  $c$  under the constraint  $c^T c = 1$ . The eigenvector analysis of the  $3 \times 3$  tensor  $J$  allows the computation of the mixed-orientation vector  $c$  up to an unknown scaling factor  $r \in \mathbb{R}$  by using the minors of  $J$ . In a second test based on the properties of  $J$ , the i2D case is confirmed, otherwise, the i0D case is assumed. In the i2D case, the vector  $rc$  has to be solved for the unknown orientations  $\theta_1$  and  $\theta_2$ .

Note, that from Equation (5.80) for the second order derivative operator, it follows for the second order Hilbert transform the following equation

$$\sin \theta_1 \sin \theta_2 f_{xx} - \sin(\theta_1 + \theta_2) f_{xy} + \cos \theta_1 \cos \theta_2 f_{yy} = 0 , \quad (5.84)$$

which can be used to solve for the unknown orientations.

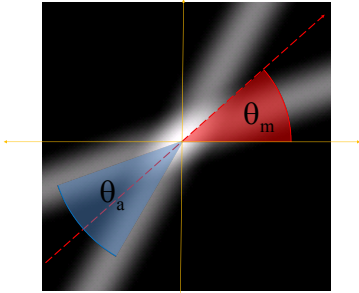
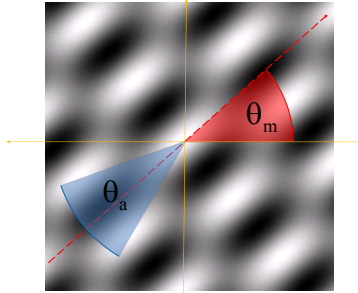
				
	[57]	Multi-Vector Signal	[57]	Multi-Vector Signal
AAE $\theta_a$	1.57°	0.15°	1.75°	0.09°
AAE $\theta_m$	1.11°	0°	1.43°	0.02°

Table 5.1.: Experimental results of the average angular error (AAE) of the apex angle  $\theta_a$  and the main orientation  $\theta_m$  of junctions and multi-layer signals.

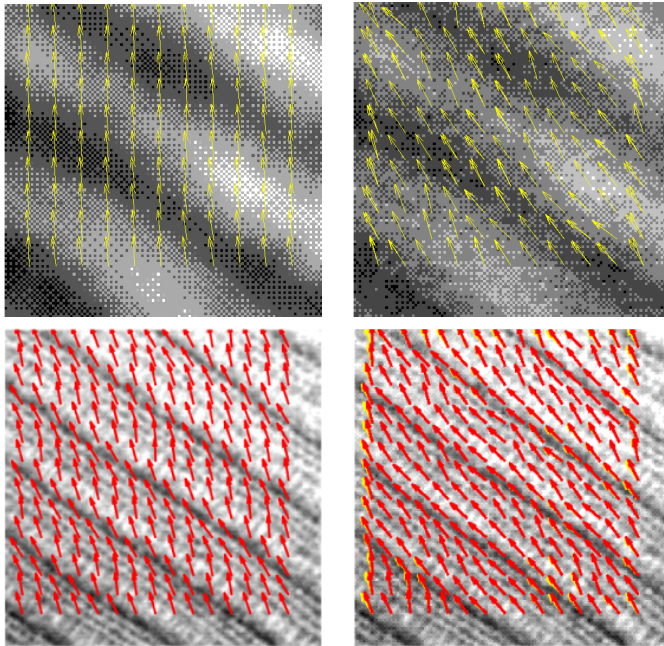


Figure 5.8.: Experimental results of a fabric texture. From left to right: orientations derived by [57] and results of the multi-vector signal.

## 5. The Multi-Vector Signal

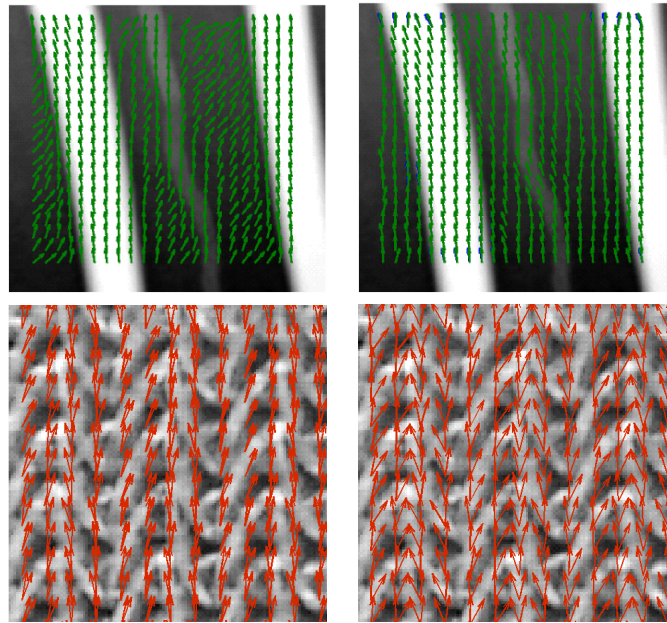


Figure 5.9.: From left to right: experimental results of [57] and the multi-vector signal on images showing a pattern on a paper box and a close up of a fabric.

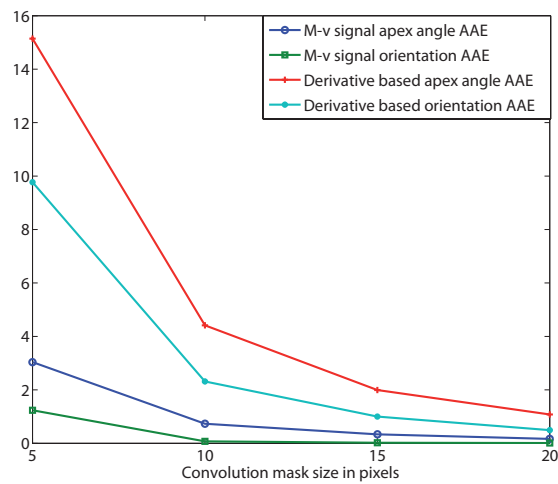


Figure 5.10.: Average angular error (AAE) of [57] and the multi-vector signal against varying convolution mask size. The multi-vector signal performs better with small size which is very important for local feature detection.

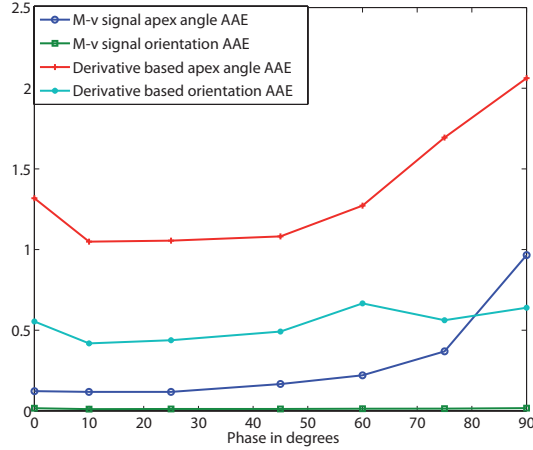


Figure 5.11.: Average angular error (AAE) of [57] and the multi-vector signal against varying signal phase.

### Comparison: Multi-Vector Signal Versus Derivatives

Both methods have been tested on a set of synthetic and real images. The experiments on synthetic data have been conducted on patchlets with same size as the convolution kernels. Two superimposed structures have been tested in all possible combinations of angles, see Table (5.1). As can be seen in the Table (5.1), the multi-vector signal method performs better than [57] in both: main orientation  $\theta_m = (\theta_1 + \theta_2) / 2$  and apex angle (opening angle)  $\theta_a = \|\theta_1 - \theta_2\|$ . In addition, the performance of both methods in case of changing convolution kernel size and changing phase has been determined. As can be seen in Figures (5.10) and (5.11) the multi-vector signal method is more robust in both cases. Figure (5.8) shows the superiority of the multi-vector signal on noisy images. The single orientation of the fabric has not been detected by the derivative based approach at all, whereas the multi-vector signal detected the orientation accurately. The upper example in Figure (5.9) shows an i1D pattern on a paper box, which has been detected better by the multi-vector signal method. The close up of the fabric in the bottom row of Figure (5.9) shows an i2D pattern, on which the derivative based method could not detect the junctions properly. In case of the method [57] applied to real images, it was sometimes difficult to adjust the parameter  $\lambda$  deciding between i1D and i2D signals, whereas the multi-vector signal based method only needs the scale space parameters, which can be adjusted automatically by phase congruency [3, 25, 32, 37, 52, 40, 50, 39].

### 5.7.2. Dense Optical Flow Estimation

The optical flow of a sequence of image signals is defined by the vector field

$$w(z) = [u(z), v(z)]^T \quad (5.85)$$

## 5. The Multi-Vector Signal

which determines the displacement for each pixel position  $z = (x, y) \in \mathbb{R}^2$ . In optical flow applications the traditional constancy constraints can easily be replaced by the phase vector of the multi-vector signal

$$\Phi^\nu = \begin{bmatrix} \Phi_x^\nu \\ \Phi_y^\nu \end{bmatrix} = \phi_\nu \begin{bmatrix} \cos \theta_\nu \\ \sin \theta_\nu \end{bmatrix} \quad (5.86)$$

consisting of the local orientation  $\theta_\nu$  and the local phase  $\phi_\nu$  for each  $\nu$  to minimize the resulting nonlinear energy functional [8]

$$E(w) = \int_{z \in \Omega} \lambda E_{\text{Smooth}}(w, z) + E_{\text{Data}}(w, z) dz \quad (5.87)$$

with  $\lambda > 0$  as a weighting factor of the smoothness term

$$E_{\text{Smooth}}(w, z) = \Psi(\|\nabla u(z)\|^2 + \|\nabla v(z)\|^2) \quad (5.88)$$

and the data term

$$E_{\text{Data}}(w, z) = \sum_{\substack{\iota \in \{x, y\} \\ \nu \in \{1, 2\}}} \Psi(\|\Phi_\iota^\nu(z + w(z), s) - \Phi_\iota^\nu\|^2) \quad (5.89)$$

with  $\Psi(s^2) = \sqrt{s^2 + \epsilon^2}$  as the penalizing function for a small constant  $\epsilon$ . Note that the naturally involved scale space embedding of the multi-vector signal automatically provides a multi-resolution or coarse-to-fine warping [48, 8] strategy. The main advantage of the phase vector is the invariance against global and local illumination changes and the robustness against noise, see Figures (5.13) and (5.12). The reason here is, that the feature space of the multi-vector signal is spanned orthogonally by the local amplitude and the remaining signal information. Therefore, changes of the local amplitude are always independent of the residual signal features.



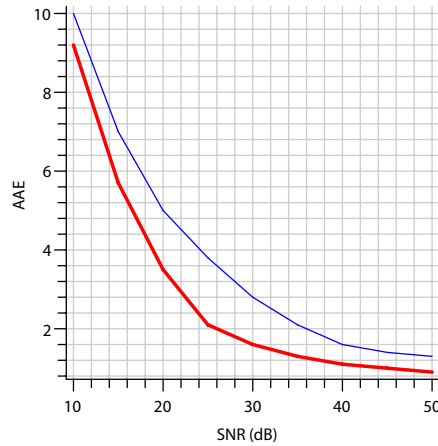


Figure 5.12.: Experimental results of the average angular error (AAE) [48] in optical flow estimation applications. Comparison of the SIFT feature based (thin blue line) constancy constraints and the phase vector (thick red line) delivered by the multi-vector signal. The figure shows that the phase vector is much more robust against additive Gaussian noise.

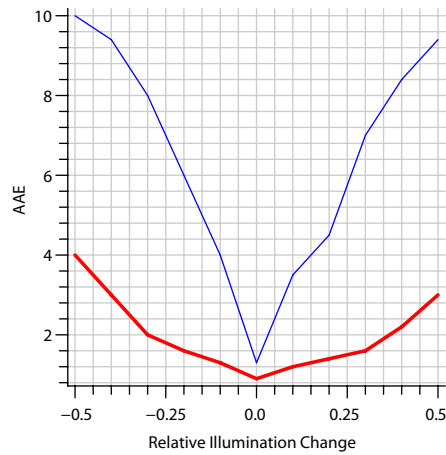


Figure 5.13.: Experimental results of the average angular error (AAE) [48] in optical flow estimation applications. Comparison of the SIFT feature based (thin blue line) constancy constraints and the phase vector (thick red line) delivered by the multi-vector signal. Since the multi-vector signal delivers a split of identity where the amplitude information is orthogonal to the phase information, the phase vector is invariant against global and local illumination changes.



## 6. Conclusion and Outlook

The main goals of this thesis are to define local simple signal models, which can be used for local rotationally invariant analysis of signals by generalized Hilbert transforms. We focused this work mainly on two-dimensional signals, although the presented conformal monogenic signal can be applied to signals of any dimension  $\geq 2$ . This work is mainly based on the results and open questions of [15] and [76]. Felsberg showed that intrinsic one dimensional signals (i1D) can be analyzed locally by the first order generalized Hilbert transform for any signal dimension  $\geq 2$ . Furthermore, also signals of intrinsic dimension two (i2D) had been analyzed with certain restrictions. In this thesis we showed an analytic model of i1D and i2D signals with less restrictions. Zang introduced an algebraic framework of tensors to embed higher order generalized Hilbert transforms for signal analysis without giving a certain signal model of i2D signals. The analysis of the so called monogenic curvature tensor [76] cannot distinguish between signals of different intrinsic dimension. In this thesis we could analyze the Clifford number valued monogenic curvature tensor by an isomorphism (hybrid matrix geometric algebra [53]) of the tensor structure to a conformal space which can be regarded as being more natural for the signal analysis tasks which should be solved by this work. We could show that with a small set of only seven filters the class of i1D signals and the class of two superimposed i1D signals can be identified and analyzed in a rotationally invariant way. We proposed the Clifford number valued conformal space as one interesting algebraic embedding for signal analysis in higher dimensions in which the monogenic signal [15] is a special case for i1D signals. For signal intelligence we focused on the relation between the higher order generalized Hilbert transforms and the Radon transform in spatial domain in contrast to signal analysis on Fourier domain. Although both spaces are equivalent to each other, sometimes it depends on the point of view from where the specific problems are regarded. Same with the embedding of real signals into Clifford number valued algebraic spaces. Often the question came up if the embedding into Clifford algebra is necessary or not, since all calculations can be done also with real numbers.

We also focus on integral transforms such as the generalized Hilbert transform, also known as Riesz transform. The Hilbert transform has already been generalized to any dimension and to any order. Low level signal analysis by generalized Hilbert transforms has been done only in Euclidean spaces. The Euclidean space has been extended to homogeneous and conformal spaces in this work. We could show that the local signal feature space which is spanned by orientation, amplitude and phase can be extended by the curvature feature after transforming signals in conformal spaces by the conformal monogenic signal. The transformation to other spaces than the Euclidean space motivated the introduction of the 2D isotropic analytic signal where the original signal is being analyzed in the projective space. The 2D isotropic analytic signal generalizes the

## 6. Conclusion and Outlook

monogenic signal to i1D and a special class of i2D signals which is restricted to two superimposed i1D signals with same phase and amplitude but with arbitrary orientations. Since the local phase is independent of the local amplitude, the local phase based approaches have been applied to computer vision tasks where the problem of different local illumination and contrast play a role in the performance results of point correspondences.

Since the 2D isotropic analytic signal is still restricted to the class of i1D signals and the subclass of i2D signals the multi-vector signal has been defined by taking advantage of all Clifford valued entries of the monogenic curvature tensor [76]. The difference between the 2D isotropic analytic signal and the multi-vector signal lies in the different geometric interpretation of all entries given by the hybrid matrix geometric algebra. The multi-vector signal presented in this work extends the restricted signal model of the structure multi-vector [15] by using the same set of seven filters consisting of the generalized Hilbert transforms of order one to three. We also tried to give a geometric interpretation of the multi-vector signal as well as a more natural algebraic embedding motivated by the results of the previous approaches of this work and the fundamental work e.g. by M. Felsberg and G. Sommer.

Although in practical local signal analysis task most people make use of the well known derivative operators, there are still advantages in using the Hilbert integral transforms since the local phase can be split from the local signal amplitude or energy. Furthermore, the computational effort using the Hilbert transform kernel filter set in scale space instead of using the blurred derivative operators stays the same. Normally, the global performance of a computer vision system does not depend on the performance of the low level local signal analysis approaches. But if you compare the derivative operator and the Hilbert transform there are differences which could be shown in this thesis. Also, the quality of a low level signal analysis depends on a good design of the local signal model which has to match the points of interest within the given input signals.

Since steerable filters and quadrature filters are still in use in many practical applications it is worth to take a look at the results of this thesis. The steerable filters are not isotropic and require more computational time in comparison to the multi-vector signal for instance. The disadvantage of the multi-vector is the restriction to only two superimposed i1D signals. Whereas the steerable filters can detect as many superimposed i1D signals as steered tests are done on the test signal in different directions. But from the statistical point of view most points are of i0D, followed by i1D and only a few points are of i2D. If the local signal model of two superimposed i1D signals fits the reality of natural pictures or videos, the multi-vector signal can speed up existing computer vision algorithms significantly.

Also, the presented local signal model of a cosine wave with arbitrary amplitude, phase, and orientation can be used in 3D camera applications in which a sinusoidal fringe pattern is projected onto the surface of a three-dimensional object to reconstruct the depth information. These 3D approaches use sinusoidal patterns with different phases in at

least four different subsequent projections to reconstruct the point cloud. Here also the local phase is needed and can be extended to further approaches where two or more 1D signals are superimposed.

The currently most successful signal analysis approaches seem to be the statistical approaches. Please also note that the multi-vector signal has a strong relationship to statistics since the apex angle corresponds to the variance and the main orientation is nothing else but the mean value of a certain number of superimposed 1D signals. The analysis of the multi-vector signal should also correspond to the analysis of mixed statistics. So, the future work based on the results and open questions of this thesis could generalize the local signal model to more superimposed 1D signals in higher dimensions. Also, the idea of the monogenic curvature tensor and the algebraic embedding of the multi-vector signal could be summarized into one unified framework.



# A. Proof: Geometric Information by the Multi-Vector Signal

We evaluate the Hilbert transformed signals based on the signal model of two arbitrary superimposed i1D signals with arbitrary orientations, arbitrary phases, and arbitrary amplitudes:

$$f_p = f_1^e + f_2^e = a_1 \cos \phi_1 + a_2 \cos \phi_2 \quad (\text{A.1})$$

and

$$\begin{bmatrix} f_x \\ f_y \end{bmatrix} = \sum_{\nu=1}^2 \begin{bmatrix} \cos \theta_\nu \\ \sin \theta_\nu \end{bmatrix} f_\nu^o \quad (\text{A.2})$$

and

$$\begin{bmatrix} f_{xx} \\ f_{yy} \end{bmatrix} = \sum_{\nu=1}^2 \begin{bmatrix} \cos^2 \theta_\nu \\ \sin^2 \theta_\nu \end{bmatrix} f_\nu^e \quad (\text{A.3})$$

and

$$f^- = f_{xx} - f_{yy} = \cos(2\theta_1)f_1^e + \cos(2\theta_2)f_2^e \quad (\text{A.4})$$

and

$$f_{xy} = \frac{1}{2} \sin(2\theta_1)f_1^e + \frac{1}{2} \sin(2\theta_2)f_2^e \quad (\text{A.5})$$

and

$$\begin{bmatrix} f_{xxx} \\ f_{xxy} \\ f_{xyy} \\ f_{yyy} \end{bmatrix} = \sum_{\nu=1}^2 \begin{bmatrix} \cos^3 \theta_\nu \\ \cos^2 \theta_\nu \sin \theta_\nu \\ \cos \theta_\nu \sin^2 \theta_\nu \\ \sin^3 \theta_\nu \end{bmatrix} f_\nu^o \quad (\text{A.6})$$

and

$$f_x^- = f_{xxx} - f_{xyy} = \cos \theta_1(2 \cos^2 \theta_1 - 1)f_1^o + \cos \theta_2(2 \cos^2 \theta_2 - 1)f_2^o, \quad (\text{A.7})$$

$$f_y^- = f_{xxy} - f_{yyy} = \sin \theta_1(2 \cos^2 \theta_1 - 1)f_1^o + \sin \theta_2(2 \cos^2 \theta_2 - 1)f_2^o \quad (\text{A.8})$$

A. Proof: Geometric Information by the Multi-Vector Signal

we define

$$\varepsilon = \left[ \frac{f_p}{2} \right]^2 - f_{xy}^2 - \left[ \frac{f^-}{2} \right]^2, \quad (\text{A.9})$$

$$\delta = \left[ \frac{f_x}{2} \right]^2 - f_{xxy}^2 - \left[ \frac{f_x^-}{2} \right]^2, \quad (\text{A.10})$$

$$\beta = \left[ \frac{f_y}{2} \right]^2 - f_{xyy}^2 - \left[ \frac{f_y^-}{2} \right]^2, \quad (\text{A.11})$$

$$\alpha = \frac{f_x f_y}{2} - f_{xxy} f_{xyy} - \frac{f_x^- f_y^-}{2}, \quad (\text{A.12})$$

and we use the following abbreviations

$$\gamma^+ = \frac{1}{2} (\delta + \beta), \quad (\text{A.13})$$

$$\gamma^- = \frac{1}{2} (\delta - \beta). \quad (\text{A.14})$$

The evaluation reads

$$\varepsilon = f_1^e f_2^e \quad (\text{A.15})$$

$$\begin{aligned} & (-2 \cos^2 \theta_2 \cos^2 \theta_1 - 2 \cos \theta_1 \sin \theta_2 \sin \theta_1 \cos \theta_2 - \cos^2 \theta_2 - \cos^2 \theta_1) \\ & = f_1^e f_2^e \sin^2(\theta_1 - \theta_2) \end{aligned} \quad (\text{A.16})$$

and

$$\delta = f_1^o f_2^o \cos \theta_1 \cos \theta_2 \quad (\text{A.17})$$

$$\begin{aligned} & (-2 \cos^2 \theta_1 \cos^2 \theta_2 - 2 \cos \theta_1 \sin \theta_1 \cos \theta_2 \sin \theta_2 - \cos^2 \theta_1 - \cos^2 \theta_2) \\ & = f_1^o f_2^o \sin^2(\theta_1 - \theta_2) \frac{1}{2} (\cos(\theta_1 - \theta_2) + \cos(\theta_1 + \theta_2)) \end{aligned} \quad (\text{A.18})$$

and

$$\beta = f_1^o f_2^o \quad (\text{A.19})$$

$$\begin{aligned} & (-2 \sin \theta_1 \sin \theta_2 \cos^2 \theta_1 \cos^2 \theta_2 - 2 \cos \theta_1 \cos \theta_2 + \sin \theta_1 \sin \theta_2 \cos^2 \theta_1 + \\ & \sin \theta_1 \sin \theta_2 \cos^2 \theta_2 - 2 \cos^3 \theta_1 \cos^3 \theta_2 + 2 \cos^3 \theta_1 \cos \theta_2 + 2 \cos^3 \theta_2 \cos \theta_1) \\ & = f_1^o f_2^o \sin^2(\theta_1 - \theta_2) \frac{1}{2} (\cos(\theta_1 - \theta_2) - \cos(\theta_1 + \theta_2)) \end{aligned} \quad (\text{A.20})$$

and

$$\alpha = f_1^o f_2^o \frac{1}{2} \quad (\text{A.21})$$

$$\begin{aligned} & (\cos^3 \theta_2 \sin \theta_1 + \cos^3 \theta_1 \sin \theta_2 - \cos^2 \theta_2 \sin \theta_2 \cos \theta_1 - \cos^2 \theta_1 \sin \theta_1 \cos \theta_2) \\ & = f_1^o f_2^o \sin^2(\theta_1 - \theta_2) \frac{1}{2} \sin(\theta_1 + \theta_2) \end{aligned} \quad (\text{A.22})$$



and

$$\gamma^+ = f_1^o f_2^o \sin^2(\theta_1 - \theta_2) \frac{1}{2} \cos(\theta_1 - \theta_2), \quad (\text{A.23})$$

$$\gamma^- = f_1^o f_2^o \sin^2(\theta_1 - \theta_2) \frac{1}{2} \cos(\theta_1 + \theta_2). \quad (\text{A.24})$$

With the abbreviations

$$s_{\pm} = \sin(\theta_1 \pm \theta_2) \quad (\text{A.25})$$

$$c_{\pm} = \cos(\theta_1 \pm \theta_2). \quad (\text{A.26})$$

we evaluate

$$\epsilon_2 = \sqrt{\alpha^2 - \beta\delta} \quad (\text{A.27})$$

$$= f_1^o f_2^o s_-^2 \frac{1}{2} \sqrt{s_+^2 - (c_- - c_+)(c_- + c_+)} \quad (\text{A.28})$$

$$= f_1^o f_2^o s_-^2 \frac{1}{2} \sqrt{\underbrace{(s_+^2 + c_+^2)}_1 - c_-^2} \quad (\text{A.29})$$

$$= f_1^o f_2^o \sin^2(\theta_1 - \theta_2) \frac{1}{2} \sin(\theta_1 - \theta_2) \quad (\text{A.30})$$

from which follows

$$\sigma = \sqrt{\alpha^2 + (\gamma^-)^2} = \sqrt{\epsilon_2^2 + (\gamma^+)^2} = f_1^o f_2^o s_-^2 \frac{1}{2}. \quad (\text{A.31})$$

It follows

$$\sin(\theta_1 + \theta_2) = \frac{\alpha}{\sigma}. \quad (\text{A.32})$$

Now, the main orientation can be determined by

$$\frac{\alpha}{\gamma^-} = \frac{\sin \theta_1 \cos \theta_1 + \sin \theta_2 \cos \theta_2}{\cos^2 \theta_1 + \cos^2 \theta_2 - 1} = \frac{\sin(\theta_1 + \theta_2)}{\cos(\theta_1 + \theta_2)} \quad (\text{A.33})$$

$$\Rightarrow \theta_1 + \theta_2 = \arctan \frac{\alpha}{\gamma^-} \quad (\text{A.34})$$

and the apex angle by

$$\frac{\epsilon_2}{\gamma^+} = \frac{\sin^3(\theta_1 - \theta_2)}{\sin^2(\theta_1 - \theta_2) \cos(\theta_1 - \theta_2)} \quad (\text{A.35})$$

$$\Rightarrow \|\theta_1 - \theta_2\| = \arctan \frac{\epsilon_2}{\gamma^+}. \quad (\text{A.36})$$

In the following we want to derive the single orientations  $\theta_\nu$  directly. Furthermore, with the following abbreviations

A. Proof: Geometric Information by the Multi-Vector Signal

$$\lambda_{1/2} = (\alpha \pm \epsilon_2)^2 + \beta^2 = (\alpha \pm \epsilon_2)^2 + (\gamma^+ - \gamma^-)^2 \quad (\text{A.37})$$

$$\kappa_{1/2} = \delta(\alpha \pm \epsilon_2) + \beta(\alpha \mp \epsilon_2) = 2(\alpha\gamma^+ \pm \gamma^-\epsilon_2) \quad (\text{A.38})$$

and

$$\tau_\nu = \sqrt{\kappa_\nu^2 + \lambda_\nu^2} \quad (\text{A.39})$$

we result in

$$\lambda_{1/2} = 2 \left[ f_1^o f_2^o s_-^2 \frac{1}{2} \right]^2 \underbrace{(1 \pm s_- s_+ - c_- c_+)}_{2s_{1/2}^2} \quad (\text{A.40})$$

$$\kappa_{1/2} = 2 \left[ f_1^o f_2^o s_-^2 \frac{1}{2} \right]^2 \underbrace{(s_+ c_- \pm s_- c_+)}_{2s_{1/2} c_{1/2}} \quad (\text{A.41})$$

$$\tau_{1/2}^2 = 4 \left[ f_1^o f_2^o s_-^2 \frac{1}{2} \right]^4 2 \underbrace{(1 \pm s_- s_+ - c_- c_+)}_{2s_{1/2}^2} \quad (\text{A.42})$$

$$\tau_{1/2} = 2 \left[ f_1^o f_2^o s_-^2 \frac{1}{2} \right]^2 \underbrace{\sqrt{2} \sqrt{1 \pm s_- s_+ - c_- c_+}}_{2s_{1/2}} \quad (\text{A.43})$$

which delivers the single orientations

$$s_\nu = \sin \theta_\nu = \frac{\lambda_\nu}{\tau_\nu} \quad (\text{A.44})$$

$$c_\nu = \cos \theta_\nu = \frac{\kappa_\nu}{\tau_\nu} \quad (\text{A.45})$$

$$t_\nu = \tan \theta_\nu = \frac{\lambda_\nu}{\kappa_\nu}. \quad (\text{A.46})$$

## A.1. Alternative

In the following we will use the inverse of the determinant

$$d_{1/2} = \det^{-1} \begin{bmatrix} \frac{f_x}{2} & \cos \theta_{1/2} \\ \frac{f_y}{2} & \sin \theta_{1/2} \end{bmatrix}. \quad (\text{A.47})$$

From Equation (5.21) of the third order generalized Hilbert transform and Equation (5.17) of the first order generalized Hilbert transform for two superimposed i1D signals ( $n = 2$ ) the most important relations of the orientations follow:

$$\sin(2\theta_{2/1}) = d_{1/2} \det \begin{bmatrix} f_{xxy} & \cos \theta_{1/2} \\ f_{xyy} & \sin \theta_{1/2} \end{bmatrix} \quad (\text{A.48})$$

and

$$\cos(2\theta_{2/1}) = d_{1/2} \det \begin{bmatrix} \frac{f_x^-}{2} & \cos \theta_{1/2} \\ \frac{f_y^-}{2} & \sin \theta_{1/2} \end{bmatrix} \quad (\text{A.49})$$

which will be solved in the following. From the fact that

$$\sin^2(2\theta_{2/1}) + \cos^2(2\theta_{2/1}) = 1, \quad (\text{A.50})$$

the nonlinear part of the inverse problem follows in form of an equation which is similar to a quadratic equation

$$-2\gamma^- \sin^2 \theta_\nu + \alpha \sin(2\theta_\nu) = \beta, \quad (\text{A.51})$$

since two unknown orientations have to hold the equation. With

$$\lambda_{1/2} = (\alpha \pm \epsilon_2)^2 + \beta^2 = (\alpha \pm \epsilon_2)^2 + (\gamma^+ - \gamma^-)^2 \quad (\text{A.52})$$

$$\kappa_{1/2} = \delta (\alpha \pm \epsilon_2) + \beta (\alpha \mp \epsilon_2) = 2 (\alpha \gamma^+ \pm \gamma^- \epsilon_2) \quad (\text{A.53})$$

and

$$\tau_\nu = \sqrt{\kappa_\nu^2 + \lambda_\nu^2} \quad (\text{A.54})$$

the orientations can be determined by

$$\theta_\nu = \text{atan2}(\lambda_\nu, \kappa_\nu) \quad (\text{A.55})$$

and

$$s_\nu = \sin \theta_\nu = \frac{\lambda_\nu}{\tau_\nu} \quad (\text{A.56})$$

$$c_\nu = \cos \theta_\nu = \frac{\kappa_\nu}{\tau_\nu} \quad (\text{A.57})$$

$$t_\nu = \tan \theta_\nu = \frac{\lambda_\nu}{\kappa_\nu} \quad (\text{A.58})$$

for phase values  $\phi_\nu \neq 0$ .



## B. Proof: Structural Information by the Multi-Vector Signal

For the assumed i2D signal model  $f_p = f_1^e + f_2^e$  the phases can be split from the amplitudes and orientations, e.g. by the following relation

$$\sigma = \sqrt{\alpha^2 + (\gamma^-)^2} = \sqrt{\epsilon_2^2 + (\gamma^+)^2} = f_1^o f_2^o s_-^2 \frac{1}{2} \quad (\text{B.1})$$

from which follows

$$\frac{2\sqrt{\alpha^2 + (\gamma^-)^2}}{\epsilon} = 2\frac{\sigma}{\epsilon} = \tan \phi_1 \tan \phi_2 . \quad (\text{B.2})$$

In the following we will use the abbreviation

$$\frac{1}{s_-^2} = \left(\frac{\gamma^+}{\epsilon_2}\right)^2 + 1 \quad (\text{B.3})$$

and

$$\frac{1}{c_+} = \sqrt{\left(\frac{\alpha}{\gamma^-}\right)^2 + 1} . \quad (\text{B.4})$$

From the definition of  $f_p = f_1^e + f_2^e$  and  $\epsilon$  follows

$$f_\nu^e \in \left\{ \frac{f_p}{2} \pm \sqrt{\left(\frac{f_p}{2}\right)^2 - \frac{\epsilon}{s_-^2}} \right\} \quad (\text{B.5})$$

and

$$(f_{1/2}^e)^2 = \frac{1}{2}f_p^2 - \frac{\epsilon}{s_-^2} \pm f_p \sqrt{\left(\frac{f_p}{2}\right)^2 - \frac{\epsilon}{s_-^2}} \quad (\text{B.6})$$

which delivers

$$f_+^e = (f_1^e)^2 + (f_2^e)^2 = f_p^2 - \frac{2\epsilon}{s_-^2} . \quad (\text{B.7})$$

Furthermore, from  $f_x^2 + f_y^2$  follows

$$f_+^o = (f_1^o)^2 + (f_2^o)^2 = f_x^2 + f_y^2 - \frac{4\gamma^+}{s_-^2} \quad (\text{B.8})$$

B. Proof: Structural Information by the Multi-Vector Signal

and

$$(f_{1/2}^o)^2 = \frac{1}{2}f_+^o \pm \frac{1}{2}\sqrt{[f_+^o]^2 - \left(\frac{4\epsilon_2}{s_-^3}\right)^2}. \quad (\text{B.9})$$

Now, the sum of the squared amplitudes can be determined by

$$a_1^2 + a_2^2 = f_+^e + f_+^o = f_p^2 + f_x^2 + f_y^2 - \frac{2(\epsilon + 2\gamma^+)}{s_-^2}. \quad (\text{B.10})$$

From

$$f_1^e f_2^e \pm f_1^o f_2^o = \frac{1}{s_-^2} (\epsilon \pm 2\sigma) \quad (\text{B.11})$$

follows

$$a_1 a_2 \cos(\phi_1 \pm \phi_2) = \frac{1}{s_-^2} (\epsilon \mp 2\sigma). \quad (\text{B.12})$$

Furthermore, we result in

$$a_1 a_2 \sin(\phi_1 \pm \phi_2) = f_1^o f_2^e \pm f_2^o f_1^e. \quad (\text{B.13})$$

Now, the phases can be calculated by

$$\phi_1 \pm \phi_2 = \arctan \frac{f_1^o f_2^e \pm f_2^o f_1^e}{\frac{1}{s_-^2} (\epsilon \mp 2\sigma)}. \quad (\text{B.14})$$

In the following we want to analyze the resulting amplitude and phase of two arbitrary superimposed 1D signals<sup>1</sup>. The resulting amplitude of two superimposed 1D signals is defined by

$$a = \sqrt{a_1^2 + a_2^2 + 2a_1 a_2 \cos(\phi_1 - \phi_2)} \quad (\text{B.15})$$

$$= \sqrt{f_p^2 + f_x^2 + f_y^2 + \frac{4}{s_-^2} (\sigma - \gamma^+)} \quad (\text{B.16})$$

with the even part of the signal

$$f_p = f_1^e + f_2^e = a \cos \phi \quad (\text{B.17})$$

and the resulting phase

$$\tan \phi = \frac{a_1 \sin \phi_1 + a_2 \sin \phi_2}{f_p} \quad (\text{B.18})$$

from which follows for the odd part of the signal

<sup>1</sup>The superposition of two 1D signals reads  $a_1 \sin(\omega t + \phi_1) + a_2 \sin(\omega t + \phi_2) = a \sin(\omega t + \phi)$ , from which follows for the resulting amplitude  $a = \sqrt{a_1^2 + a_2^2 + 2a_1 a_2 \cos(\phi_1 - \phi_2)}$ , and for the resulting phase  $\tan \phi = \frac{a_1 \sin \phi_1 + a_2 \sin \phi_2}{a_1 \cos \phi_1 + a_2 \cos \phi_2}$ .

$$f^o = f_1^o + f_2^o \quad (\text{B.19})$$

$$= a \sin \phi \quad (\text{B.20})$$

$$= a_1 \sin \phi_1 + a_2 \sin \phi_2 \quad (\text{B.21})$$

$$= \sqrt{a^2 - f_p^2} \quad (\text{B.22})$$

$$= \sqrt{f_x^2 + f_y^2 + \frac{4}{s_-^2} (\sigma - \gamma^+)} \geq 0 \quad (\text{B.23})$$

and the resulting phase

$$\phi = \arctan \frac{\sqrt{f_x^2 + f_y^2 + \frac{4}{s_-^2} (\sigma - \gamma^+)}}{f_p} \quad (\text{B.24})$$

and the single odd parts of the signal

$$f_\nu^o \in \left\{ \frac{f^o}{2} \pm \sqrt{\left(\frac{f^o}{2}\right)^2 - \frac{2\sigma}{s_-^2}} \right\} \quad (\text{B.25})$$

which can be used to determine the single phases

$$\phi_\nu = \arctan \frac{f_\nu^o}{f_\nu^e} \quad (\text{B.26})$$

and the single amplitudes

$$a_\nu = \sqrt{(f_\nu^e)^2 + (f_\nu^o)^2}. \quad (\text{B.27})$$

## B.1. Alternative

The phase and amplitude represent the structural signal features, which can be calculated by solving a linear system of equations by the Cramer's rule of  $2 \times 2$  matrices. The even and odd signal parts can be derived by

$$\begin{bmatrix} f_1^e \\ f_2^e \end{bmatrix} = \frac{1}{c^e} \begin{bmatrix} \frac{f_p}{2} \sin(2\theta_2) - f_{xy} \\ -\frac{f_p}{2} \sin(2\theta_1) + f_{xy} \end{bmatrix} \quad (\text{B.28})$$

with

$$\sin(2\theta_{1/2}) = \frac{\alpha\gamma^+ \pm \epsilon_2\gamma^-}{\sqrt{(\gamma^+)^2 + \epsilon_2^2} \sqrt{(\gamma^-)^2 + \alpha^2}} \quad (\text{B.29})$$

and

B. Proof: Structural Information by the Multi-Vector Signal

$$c^e = \sin(\theta_1 - \theta_2) \cos(\theta_1 + \theta_2) \quad (\text{B.30})$$

where

$$\frac{1}{c^e} = \frac{\sqrt{(\gamma^+)^2 + \epsilon_2^2} \sqrt{(\gamma^-)^2 + \alpha^2}}{\epsilon_2 \gamma^-} \quad (\text{B.31})$$

and

$$\frac{1}{c^e} = \sqrt{\left(\frac{\gamma^+}{\epsilon_2}\right)^2 + 1} \sqrt{\left(\frac{\alpha}{\gamma^-}\right)^2 + 1} \quad (\text{B.32})$$

which has been derived by the second order generalized Hilbert transform, and

$$\begin{bmatrix} f_1^o \\ f_2^o \end{bmatrix} = \frac{1}{c^o} \begin{bmatrix} f_y \cos \theta_2 - f_x \sin \theta_2 \\ -f_y \cos \theta_1 + f_x \sin \theta_1 \end{bmatrix} \quad (\text{B.33})$$

with

$$c^o = \sin(\theta_1 - \theta_2) \quad (\text{B.34})$$

where

$$\frac{1}{c^o} = \frac{\sqrt{(\gamma^+)^2 + \epsilon_2^2}}{\epsilon_2} \quad (\text{B.35})$$

which has been derived by the first order generalized Hilbert transform respectively. By means of the even and odd signal parts, finally the structural signal features such as the phases and the amplitudes can be derived by

$$\phi_\nu = \text{atan2}(f_\nu^o, f_\nu^e) \quad (\text{B.36})$$

and

$$a_\nu = \sqrt{(f_\nu^e)^2 + (f_\nu^o)^2} \quad (\text{B.37})$$

for  $\nu \in \{1, 2\}$ .

An alternative for the solution for the even and odd signal parts is given by

$$f_{1/2}^o = \frac{\tau_{1/2}}{\kappa_1 \lambda_2 - \kappa_2 \lambda_1} (f_x \lambda_{2/1} - f_y \kappa_{2/1}) \quad (\text{B.38})$$

$$f_{1/2}^e = \frac{\tau_{1/2}^2}{\kappa_2 \lambda_2 \tau_1^2 - \kappa_1 \lambda_1 \tau_2^2} (f_p \kappa_{2/1} \lambda_{2/1} - f_{xy} \tau_{2/1}^2) \quad (\text{B.39})$$

which can be used to determine the single phase values

$$\phi_{1/2} = \arctan \left( \frac{\tau_{2/1}}{\sqrt{\left(\frac{\alpha}{\gamma^-}\right)^2 + 1}} \frac{f_x \lambda_{2/1} - f_y \kappa_{2/1}}{\kappa_{2/1} \lambda_{2/1} f_p - \tau_{2/1}^2 f_{xy}} \right). \quad (\text{B.40})$$



## C. Comparison: The Monogenic Curvature Tensor

In the following we will use the abbreviations

$$s_\nu = \sin \theta_\nu \quad (\text{C.1})$$

$$c_\nu = \cos \theta_\nu \quad (\text{C.2})$$

$$s_\pm = \sin(\theta_1 \pm \theta_2) \quad (\text{C.3})$$

$$c_\pm = \cos(\theta_1 \pm \theta_2) \quad (\text{C.4})$$

and

$$c_1 c_2 = \frac{1}{2}(c_- + c_+) \quad (\text{C.5})$$

$$s_1 s_2 = \frac{1}{2}(c_- - c_+) . \quad (\text{C.6})$$

For the assumed i2D signal model  $f_p = f_1^e + f_2^e$  the monogenic curvature tensor introduced in [76] can be evaluated as

$$\det(T^e) = f_1^e f_2^e s_-^2 = \varepsilon \quad (\text{C.7})$$

$$\det(T_x^o) = f_1^o f_2^o s_-^2 c_1 c_2 = \delta \quad (\text{C.8})$$

$$\det(T_y^o) = f_1^o f_2^o s_-^2 s_1 s_2 = \beta \quad (\text{C.9})$$

and

$$\text{trace } T^e = f_p \quad (\text{C.10})$$

$$\text{trace } T_x^o = f_x \quad (\text{C.11})$$

$$\text{trace } T_y^o = f_y \quad (\text{C.12})$$

which results in

$$\frac{\det(T_y^o)}{\det(T_x^o)} = \tan \theta_1 \tan \theta_2 \quad (\text{C.13})$$

for the orientation parameters claimed in [76]. The rest of the evaluation is up to the reader, e.g. the phase claimed in [76]:

$$\frac{\sqrt{(\det(T_x^o))^2 + (\det(T_y^o))^2}}{\det(T^e)} = \tan \phi_1 \tan \phi_2 \sqrt{c_1^2 c_2^2 + s_1^2 s_2^2} . \quad (\text{C.14})$$



## D. Comparison: The Structure Multi-Vector

The structure multi-vector [15]  $M_S$  is a low level phase based signal analysis approach, which assumes that two arbitrary but perpendicular 1D signals are superimposed. The appropriated signal model reads

$$\begin{aligned} \mathcal{P}_s \{f\} (z) = & a_1 \cos (x \cos(\theta_e - 45^\circ) + y \sin(\theta_e - 45^\circ) + \phi_1) \\ & + a_2 \cos (x \cos(\theta_e + 45^\circ) + y \sin(\theta_e + 45^\circ) + \phi_2) . \end{aligned} \quad (\text{D.1})$$

The original signal extension has been defined as a Clifford number. For the sake of simplicity, the structure multi-vector will now be written in vector notation and by using the higher order generalized Hilbert transforms of the original signal at the origin of the associated local coordinate system

$$M_S = \begin{bmatrix} f_p \\ f_x \\ f_y \\ f^- \\ f_{xy} \\ f_x^- \\ f_y^- \end{bmatrix} \quad (\text{D.2})$$

which consists of seven components and the first three entries define the monogenic signal. The so-called semi-orientation can now be calculated by

$$\theta_e = \frac{1}{4} \arctan \frac{2f_p f_y^- + f_x^- f_y - f_{xy} f_x}{f_x^- f_x + f_{xy} f_y + f_p^2 - [f_y^-]^2} \quad (\text{D.3})$$

By precalculating the semi-orientation and introducing the following abbreviations

$$f_1^e = \frac{1}{2} [f^- + f_p \cos(2\theta_e) + f_y^- \sin(2\theta_e)] , \quad (\text{D.4})$$

$$f_2^e = \frac{1}{2} [f^- - f_p \cos(2\theta_e) - f_y^- \sin(2\theta_e)] , \quad (\text{D.5})$$

$$f_1^o = \frac{1}{4} [3(f_x \cos \theta_e + f_y \sin \theta_e) + f_x^- \cos(3\theta_e) - f_{xy} \sin(3\theta_e)] , \quad (\text{D.6})$$

$$f_2^o = \frac{1}{4} [3(f_y \cos \theta_e - f_x \sin \theta_e) + f_x^- \sin(3\theta_e) + f_{xy} \cos(3\theta_e)] \quad (\text{D.7})$$

#### D. Comparison: The Structure Multi-Vector

the two unknown local amplitudes can be calculated by

$$a_\nu = \sqrt{[f_\nu^e]^2 + [f_\nu^o]^2}, \quad (\text{D.8})$$

as well as the two unknown local phases

$$\phi_\nu = \arctan \frac{f_\nu^o}{f_\nu^e}. \quad (\text{D.9})$$

The evaluation can now be calculated by the signal intelligence in Radon space. In comparison to the multi-vector signal, the structure multi-vector has the disadvantage that it assumes two superimposed perpendicular 1D signals with a subsequent steering of the semi-orientation.

## E. Implementation: The 2D Conformal Monogenic Signal

Although in theory the conformal monogenic signal performs a 3D generalized Hilbert transform in conformal space, this can be accelerated by simplifying to a faster 2D convolution directly on the sphere. Therefore the following implementation can be done in  $O(n^2)$  with  $n$  as the convolution mask size in one dimension. Any 2D image can now be analyzed locally at every test point by the following algorithm

```
//Input: double Image(double x, double y)
//Input: double x, y
//        (local pixel position)
//Input: double Coarse > Fine > 0
//        (Bandpass filter parameters)
//Input: double Size > 0 (Convolution mask size)
//Output: Direction, Phase, Curvature, Energy

double Coarse=0.2, Fine=0.1, Size=5; //e.g.
double rp=0, rx=0, ry=0, rz=0;

for(double cx = -Size; cx <= Size; cx++)
for(double cy = -Size; cy <= Size; cy++)
{
    //Map points (cx, cy) to conformal space (u, v, w)
    double d = pow(cx, 2) + pow(cy, 2) + 1;
    double u = cx / d, v = cy / d, w = (d - 1) / d;

    //Generalized Hilbert transform in conformal space
    double uvw = pow(u, 2) + pow(v, 2) + pow(w, 2);
    double pf = pow(pow(Fine, 2) + uvw, -2);
    double pc = pow(pow(Coarse, 2) + uvw, -2);
    double f = Image(x + cx, y + cy);
    double c = f * (pf - pc);

    rp += f * (Fine * pf - Coarse * pc);
    rx += u * c;
    ry += v * c;
    rz += w * c;
}
```

*E. Implementation: The 2D Conformal Monogenic Signal*

```
}
```

```
double R = pow(rx,2)+pow(ry,2)+pow(rz,2);
```

```
Curvature = sqrt(pow(rx,2)+pow(ry,2)) / rz;
```

```
Direction = atan2(ry,rx);
```

```
Phase      = atan2(sqrt(R),rp);
```

```
Energy     = pow(rp,2)+R;
```

## F. Implementation: The 3D Conformal Monogenic Signal

The computational time complexity is in  $O(n^3)$  with  $n$  as the convolution mask size in one dimension.

```
//Input: double Image3D(double x, double y, double z)
//Input: double x, y, z
//      (Local pixel test point for analysis)
//Input: double Coarse > Fine > 0
//      (Bandpass filter parameters)
//Input: double Size > 0
//      (Convolution mask size)
//Output: Direction1, Direction2,
//        Phase, Curvature, Amplitude

double Coarse=2, Fine=0.1; int Size=5; //e.g.
double rp=0, r1=0, r2=0, r3=0, r4=0;

for(double cx = -Size; cx <= Size; cx += 1)
for(double cy = -Size; cy <= Size; cy += 1)
for(double cz = -Size; cz <= Size; cz += 1)
{
    //Map points (cx, cy, cz) to conformal space
    //(x1, x2, x3, x4)
    double d = pow(cx,2)+pow(cy,2)+pow(cz,2)+1;
    double x1 = cx / d;
    double x2 = cy / d;
    double x3 = cz / d;
    double x4 = (d-1) / d;

    //Generalized Hilbert transform in conformal space
    double a = pow(x1,2)+pow(x2,2)+pow(x3,2)+pow(x4,2);
    double pf = pow(pow(Fine,2) + a, -2.5);
    double pc = pow(pow(Coarse,2) + a, -2.5);
    double f = Image3D(x + cx, y + cy, z + cz);
    double c = f * (pf - pc);
}
```

### *F. Implementation: The 3D Conformal Monogenic Signal*

```
rp += f * (Fine*pf - Coarse*pc);  
r1 += x1 * c;  
r2 += x2 * c;  
r3 += x3 * c;  
r4 += x4 * c;  
}
```

```
double R2 = pow(r1,2)+pow(r2,2);  
double R3 = R2+pow(r3,2);  
double R4 = R3+pow(r4,2);
```

```
Curvature = atan(r2/r1);  
Direction1 = asin(sqrt(R2)/r4);  
Direction2 = atan2(sqrt(R3),r4);  
Phase = atan2(sqrt(R4),rp);  
Amplitude = sqrt(pow(rp,2)+R4);
```

In practical applications such as medical image analysis [29] the convolution mask sizes must be DC-free. This can be achieved by removing their mean value after precalculating them.



## G. Implementation: The Isotropic 2D Analytic Signal

The 2D analytic signal can easily be integrated into any computer vision software package by using the following C++ implementation. Each DC-free signal

```
double f(double x,double y)
```

can be locally analyzed in scale space at every position  $(c_x, c_y) \in \mathbb{R}^2$  by applying a difference of Poisson (DoP) [18] bandpass filter to the original signal with the fine scale space parameter  $s_f$  and the coarse scale space parameter  $s_c$ .

```
void AnalyticSignal2D(  
    double cx,double cy,  
    double& Orientation,double& ApexAngle,  
    double& Amplitude,double& Phase,  
    double s_c=2,double s_f=1.9,double m=3)  
{  
    double f_p =0,f_x =0,f_y =0;  
    double f_xx=0,f_xy=0,f_yy=0;  
  
    for (double x = -m;x <= m;x++)  
    for (double y = -m;y <= m;y++)  
    {  
        double t = f(x+cx,y+cy);  
        double pf = t* Kernel1(x,y,s_f);  
        double pc = t* Kernel1(x,y,s_c);  
        double k = t*(Kernel2(x,y,s_f)-Kernel2(x,y,s_c));  
  
        f_p += s_f*pf - s_c*pc;  
        f_x += x * (pf-pc);  
        f_y += y * (pf-pc);  
        f_xx += x*x * k;  
        f_yy += y*y * k;  
        f_xy += x*y * k;  
    }  
  
    double f_pm = 0.5*(f_xx-f_yy);  
    double f_0 = 0.5* f_p;  
    double e = sqrt(pow(f_pm,2)+pow(f_xy,2))/fabs(f_0);
```

### G. Implementation: The Isotropic 2D Analytic Signal

```

double l      = pow(f_x ,2)+pow(f_y ,2);
double q      = l*2/(1+e);

Phase         =atan2(sqrt(q),f_p);
Orientation   =0.5*atan2(f_xy ,f_pm);
Amplitude     =0.5*sqrt(pow(f_p ,2)+q);
ApexAngle     =atan2(sqrt(pow(f_0 ,2)-pow(f_xy ,2)-pow(f_pm ,2)),
                    sqrt(pow(f_xy ,2)+pow(f_pm ,2)));
}

```

The first order generalized 2D Hilbert convolution kernels will be calculated by

```

double Kernel1(double x,double y,double s)
{
  double S=pow(s ,2),K=pow(x,2)+pow(y ,2);
  return 1/(2*M_PI*pow(S + K,1.5));
}

```

and the second order generalized 2D Hilbert convolution kernels in the spatial domain with scale space parameter  $s$  will be determined by

```

double Kernel2(double x,double y,double s)
{
  double S=pow(s ,2),K=pow(x,2)+pow(y ,2);
  double d=pow(K,2)*pow(S+K,1.5)*2*M_PI;
  return -(s*(2*S+3*K)-2*pow(S+K,1.5))/d;
}

```

The orientation, apex angle, amplitude and phase are being calculated as distinctive local features of the signal for a given convolution mask size  $m$ . The time complexity of this algorithm is in  $O(m)$  with  $m$  as the total convolution mask size. This time complexity can be reduced by calculation in Fourier domain. The disadvantage of the calculation in Fourier domain is the restriction to a global signal analysis with one fixed scale space parameter for the entire image. By convolution in the spatial domain for each position  $(x, y; s) \in \mathbb{R}^2 \times \mathbb{R}_+$  an individual scale space parameter can be chosen to enable adaption to the local structural and geometrical signal information. Note that in case of arbitrary signals only DC-free convolution kernels can be used. This can be achieved by removing the mean value of the convolution kernels after precalculating them and before applying them to signal analysis.

## H. Implementation: The Multi-Vector Signal

The Multi-Vector Signal can easily be integrated into any computer vision software package by using the following C++ implementation. Each DC-free signal

```
double f(double x,double y)
```

can be locally analyzed in scale space at every position  $(c_x, c_y) \in \mathbb{R}^2$  by applying a difference of Poisson (DoP) [18] bandpass filter to the original signal with the fine scale space parameter  $s_f$  and the coarse scale space parameter  $s_c$ .

```
void MultiVectorSignal(  
    double cx,double cy,  
    double& Orientation,double& ApexAngle,  
    double& Amplitude,double& Phase,  
    double& Amplitude1,double& Amplitude2,  
    double& Phase1,double& Phase2,  
    double s_c=2,double s_f=1.9,double m=3)  
{  
    double f_xx=0,f_xy=0,f_yy=0;  
    double f_xxx=0,f_xxy=0,f_xyy=0,f_yyy=0;  
  
    for (double x = -m;x <= m;x++)  
    for (double y = -m;y <= m;y++)  
    {  
        double t = f(x+cx,y+cy);  
  
        double k2 = t*(Kernel2(x,y,s_f)-Kernel2(x,y,s_c));  
        double k3 = t*(Kernel3(x,y,s_f)-Kernel3(x,y,s_c));  
  
        f_xx += x*x * k2;  
        f_yy += y*y * k2;  
        f_xy += x*y * k2;  
        f_xxx += x*x*x * k3;  
        f_xxy += x*x*y * k3;  
        f_xyy += x*y*y * k3;  
        f_yyy += y*y*y * k3;  
    }  
}
```

## H. Implementation: The Multi-Vector Signal

```
double f_p  = f_xx +f_yy ;
double f_m  = f_xx -f_yy ;
double f_x  = f_xxx+f_xyy ;
double f_y  = f_xxy+f_yyy ;
double f_xm = f_xxx-f_xyy ;
double f_ym = f_xxy-f_yyy ;

double e = pow(f_p/2,2)-pow(f_xy ,2) -pow(f_m/2 ,2);
double d = pow(f_x/2,2)-pow(f_xxy ,2)-pow(f_xm/2 ,2);
double b = pow(f_y/2,2)-pow(f_xyy ,2)-pow(f_ym/2 ,2);
double a = f_x/2*f_y/2 -f_xxy*f_xyy -f_xm/2*f_ym/2;

double gp = 0.5*(d+b);
double gm = 0.5*(d-b);

double e2 = sqrt(pow(a,2)-b*d);

Orientation = atan2(a,gm);
ApexAngle   = atan2(e2 ,gp);

double s2m = pow(gp/e2 ,2)+1;
double s   = sqrt(pow(a,2)+pow(gm,2));

double c   = 4*(s-gp)*s2m;
double z   = pow(f_x ,2)+pow(f_y ,2)+c;

Amplitude  = sqrt(pow(f_p ,2)+z);
Phase      = atan2(sqrt(z) ,f_p);

double fe12 = sqrt(pow(f_p ,2)-e*s2m);
double fe1  = f_p/2 + fe12;
double fe2  = f_p/2 - fe12;

double fo  = sqrt(pow(f_x ,2)+pow(f_y ,2)+4*(s-gp)*s2m);

double fo12 = sqrt(pow(fo/2,2)-2*s*s2m);
double fo1  = fo/2 + fo12;
double fo2  = fo/2 - fo12;

Phase1 = atan2(fo1 ,fe1);
Phase2 = atan2(fo2 ,fe2);

Amplitude1 = sqrt(pow(fe1 ,2)+pow(fo1 ,2));
Amplitude2 = sqrt(pow(fe2 ,2)+pow(fo2 ,2));
```

```
}
```

The second order generalized 2D Hilbert convolution kernels in the spatial domain with scale space parameter  $s$  will be determined by

```
double Kernel2(double x,double y,double s)
{
    double S=pow(s,2),K=pow(x,2)+pow(y,2);
    double d=pow(K,2)*pow(S+K,1.5)*2*M_PI;
    return -(s*(2*S+3*K)-2*pow(S+K,1.5))/d;
}
```

and the third order generalized 2D Hilbert convolution kernels in the spatial domain with scale space parameter  $s$  will be determined by

```
double Kernel3(double x,double y,double s)
{
    double ss = pow(s,2);
    double kk = pow(x,2) + pow(y,2);

    double d = 2*M_PI*pow(kk,3)*pow(ss + kk,1.5);
    return -(ss*(8*ss+12*kk)+3*pow(kk,2)-8*s*pow(ss+kk,1.5))/d;
}
```



# Bibliography

- [1] G. Ambartsoumian and P. Kuchment. On the injectivity of the circular radon transform. *Inverse Problems*, 21(2):473, 2005.
- [2] S. Axler, P. Bourdon, and W. Ramey. *Harmonic Function Theory (Graduate Texts in Mathematics)*, volume 137. Springer, 2002.
- [3] P. R. Beaudet. Rotationally invariant image operators. In *ICPR78*, pages 579–583, 1978.
- [4] S. Bernstein. Inverse Probleme. Technical report, TU Bergakademie Freiberg, 2007.
- [5] J. Beyerer and F. P. Leon. The Radon transform in digital image processing. *Automatisierungstechnik*, 50(10):472–480, 2002.
- [6] R. N. Bracewell. *Fourier Analysis and Imaging*. Kluwer Academic Plenum Publishers, 2003.
- [7] F. Brackx, B. De Knock, and H. De Schepper. Generalized multidimensional Hilbert transforms in Clifford analysis. *International Journal of Mathematics and Mathematical Sciences*, 2006. doi:10.1155/IJMMS/2006/98145.
- [8] T. Brox, A. Bruhn, N. Papenbergh, and J. Weickert. High accuracy optical flow estimation based on a theory for warping. In *ECCV*, volume 4 of *LNCS 3024*, pages 25–36. Springer, 2004.
- [9] T. Bülow and G. Sommer. Hypercomplex signals - a novel extension of the analytic signal to the multidimensional case. *IEEE Transactions on Signal Processing*, 49(11):2844–2852, 2001.
- [10] G. Carneiro and A. D. Jepson. Phase-based local features. In *7th European Conference on Computer Vision-Part I*, volume 2350 of *LNCS*, pages 282–296. Springer-Verlag, Berlin, Heidelberg, New York, 2002.
- [11] P. E. Danielsson, Q. Lin, and Q. Z. Ye. Efficient detection of second-degree variations in 2D and 3D images. *Journal of Visual Communication and Image Representation*, 12(3):255–305, 2001.
- [12] R. Delanghe. Clifford analysis: History and perspective. *Computational Methods and Function Theory*, 1(1):107–153, 2001.

## Bibliography

- [13] R. Delanghe. On some properties of the Hilbert transform in Euclidean space. *Bull. Belg. Math. Soc. Simon Stevin*, 11(2):163–180, 2004.
- [14] M. P. do Carmo. *Differential Geometry of Curves and Surfaces*. Prentice-Hall, 1976.
- [15] M. Felsberg. *Low-Level Image Processing with the Structure Multivector*. PhD thesis, 2002.
- [16] M. Felsberg and G. Sommer. The monogenic signal. *IEEE Transactions on Signal Processing*, 49(12):3136–3144, 2001.
- [17] M. Felsberg and G. Sommer. Image Features Based on a New Approach to 2D Rotation Invariant Quadrature Filters. In *Computer Vision - ECCV 2002* eds A. Heyden and G. Sparr and M. Nielsen and P. Johansen, volume 2350 of *Lecture Notes in Computer Science*, pages 369–383, 2002.
- [18] M. Felsberg and G. Sommer. The monogenic scale-space: A unifying approach to phase-based image processing in scale-space. *Journal of Mathematical Imaging and Vision*, 21:5–26, 2004.
- [19] D. J. Fleet and A. D. Jepson. Stability of phase information. *IEEE Transactions on Pattern Analysis and Machine Intelligence*, 15(12):1253–1268, 1993.
- [20] D. J. Fleet, A. D. Jepson, and M. R. M. Jenkin. Phase-based disparity measurement. *CVGIP: Image Understanding*, 53, 1991.
- [21] O. Fleischmann. 2D Signal Analysis by Generalized Hilber Transforms. Master’s thesis, Department of Computer Science, Kiel University, Germany, 2008.
- [22] O. Fleischmann, L. Wietzke, and G. Sommer. A novel curvature estimator for digital curves and images. In M. Goesele, S. Roth, A. Kuijper, B. Schiele, and K. Schindler, editors, *Pattern Recognition*, volume 6376 of *Lecture Notes in Computer Science*, pages 442–451. Springer Berlin / Heidelberg, 2010.
- [23] O. Fleischmann, L. Wietzke, and G. Sommer. The Hilbert Transform on the Two-Sphere: A Spectral Characterization. *Mathematical Geosciences*, 42(7):857–876, 2010.
- [24] O. Fleischmann, L. Wietzke, and G. Sommer. Image Analysis by Conformal Embedding. *Journal of Mathematical Imaging and Vision*, 40(3):305–325, 2011.
- [25] W. Foerstner and E. Gulch. A fast operator for detection and precise location of distinct points, corners and centres of circular features. *Proc. Intercommission Conf. Fast Processing of Photogrammetric Data*, pages 281–305, 1987.
- [26] D. Gabor. Theory of communication. *Journal IEE, London*, 93(26):429–457, 1946.



- [27] I. S. Gradshteyn and I. M. Ryzhik. *Table of Integrals, Series, and Products*. Academic Press Elsevier, Amsterdam, Boston, Heidelberg, London, New York, Oxford, Paris, San Diego, San Francisco, Singapore, Sydney, Tokio, 2007.
- [28] G. H. Granlund and H. Knutsson. *Signal Processing for Computer Vision*. Kluwer Academic Publisher, Dordrecht, 1995.
- [29] V. Grau, H. Becher, and J. Alison Noble. Registration of multiview real-time 3-d echocardiographic sequences. In *MICCAI (1)*, pages 612–619, 2006.
- [30] K. Gürlebeck, K. Habetha, and W. Sprössig. *Funktionentheorie in der Ebene und im Raum (Grundstudium Mathematik)*. Birkhäuser, Basel, 2006.
- [31] S. L. Hahn. *Hilbert Transforms in Signal Processing*. Artech House Inc, Boston, London, 1996.
- [32] C. Harris and M. Stephens. A combined corner and edge detector. In *The Fourth Alvey Vision Conference*, pages 147–151, 1988.
- [33] D. Hestenes and G. Sobczyk. *Clifford Algebra to Geometric Calculus, A Unified Language for Mathematics and Physics*. Fundamental Theories of Physics. Kluwer Academic Publishers, Dordrecht, Boston, London, 1999.
- [34] T. Huang, J. Burnett, and A. Deczky. The importance of phase in image processing filters. *IEEE Trans. on Acoustics, Speech and Signal Processing*, 23(6):529–542, 1975.
- [35] T. Iwaniec and G. Martin. *Geometric Function Theory and Non-linear Analysis*. Oxford University Press, USA, 2002.
- [36] B. Jähne. *Digital Image Processing*. Springer, 2001.
- [37] L. Kitchen and A. Rosenfeld. Gray level corner detection. *Pattern Recognition Letters*, 1(2):95–102, 1982.
- [38] U. Köthe and M. Felsberg. Riesz-transforms vs. derivatives: On the relationship between the boundary tensor and the energy tensor. In R. Kimmel, N. Sochen, and J. Weickert, editors, *Scale Space and PDE Methods in Computer Vision*, volume 3459 of *LNCS*, pages 179–191. Springer, 2005.
- [39] P. Kovési. Image features from phase congruency. *Journal of Computer Vision Research*, 1(3), 1999.
- [40] P. Kovési. Phase congruency detects corners and edges. In *The Australian Pattern Recognition Society Conference: DICTA 2003*, pages 309–318, 2003.

## Bibliography

- [41] M. Krause and G. Sommer. A 3D isotropic quadrature filter for motion estimation problems. In *Proc. Visual Communications and Image Processing, Beijing, China*, volume 5960, pages 1295–1306. The International Society for Optical Engineering, Bellingham, 2005.
- [42] H. Li, D. Hestenes, and A. Rockwood. Spherical conformal geometry with geometric algebra. In G. Sommer, editor, *Geometric Computing with Clifford Algebra*, pages 61–76. Springer, 2000.
- [43] J. Lichtenauer, E. A. Hendriks, and M. J. T. Reinders. Isophote properties as features for object detection. *CVPR (2)*, pages 649–654, 2005.
- [44] P. Lounesto. *Clifford Algebras and Spinors*. London Mathematical Society Lecture Note Series. Cambridge University Press, May 2001.
- [45] A. Markoe. *Analytic Tomography*. Cambridge University Press, Cambridge, 2006.
- [46] T. Needham. *Visual Complex Analysis*. Oxford University Press, Oxford, 1997.
- [47] A. V. Oppenheim and J. S. Lim. The importance of phase in signals. *Proceedings of the IEEE*, 69(5):529–541, 1981.
- [48] N. Papenberg, A. Bruhn, T. Brox, S. Didas, and J. Weickert. Highly accurate optic flow computation with theoretically justified warping. *International Journal of Computer Vision*, 67(2):141–158, 2006.
- [49] C. Perwass. *Geometric Algebra with Applications in Engineering*, volume 4 of *Geometry and Computing*. Springer-Verlag, Berlin, Heidelberg, 2009.
- [50] D. Reisfeld. The constrained phase congruency feature detector: simultaneous localization, classification and scale determination. *Pattern Recogn. Lett.*, 17(11):1161–1169, 1996.
- [51] B. Rieger and L. J. van Vliet. Representing orientation in n-dimensional spaces. In *CAIP*, volume 2756 of *LNCS*, pages 17–24. Springer-Verlag, Berlin, Heidelberg, New York, 2003.
- [52] S. M. Smith and J. M. Brady. Susan - a new approach to low level image processing. *International Journal of Computer Vision*, 23:45–78, 1995.
- [53] G. Sobczyk and G. Erlebacher. Hybrid matrix geometric algebra. In H. Li, P. J. Olver, and G. Sommer, editors, *Computer Algebra and Geometric Algebra with Applications*, volume 3519 of *LNCS*, pages 191–206. Springer-Verlag, Berlin, Heidelberg, New York, 2005.
- [54] G. Sommer, editor. *Geometric computing with Clifford algebras: theoretical foundations and applications in computer vision and robotics*. Springer-Verlag, London, UK, 2001.

- [55] G. Sommer. *Computer Vision I*. Lecture Notes, Inst. f. Informatik u. Prakt. Math. der Christian-Albrechts-Universität zu Kiel, 2007.
- [56] E. M. Stein. *Singular Integrals and Differentiability Properties of Functions*. Princeton University Press, Princeton, 1971.
- [57] I. Stuke, T. Aach, E. Barth, and C. Mota. Analysing superimposed oriented patterns. In *6th IEEE Southwest Symposium on Image Analysis and Interpretation*, pages 133–137. IEEE Computer Society, 2004.
- [58] Y. Tian. Matrix theory over the complex quaternion algebra, 2000.
- [59] J. van de Weijer, L. J. van Vliet, P. W. Verbeek, and M. van Ginkel. Curvature estimation in oriented patterns using curvilinear models applied to gradient vector fields. 23(9):1035–1042, 2001.
- [60] M. van Ginkel, J. van de Weijer, L. J. van Vliet, and P. W. Verbeek. Curvature estimation from orientation fields. In B. K. Ersboll, editor, *11th Scandinavian Conference on Image Analysis*, pages 545–551. Pattern Recognition Society of Denmark, 1999.
- [61] W. Wang, N. Ishii, S. G. Hanson, Y. Miyamoto, and M. Takeda. Phase singularities in analytic signal of white-light speckle pattern with application to micro-displacement measurement. *Optics Communications*, 248:59–68, 2005.
- [62] H. Weyl. *The Theory of Groups and Quantum Mechanics*. Dover, New York, 1928.
- [63] L. Wietzke, O. Fleischmann, A. Sedlazeck, and G. Sommer. Local Structure Analysis by Isotropic Hilbert Transforms. In M. Goesele, S. Roth, A. Kuijper, B. Schiele, and K. Schindler, editors, *Pattern Recognition*, volume 6376 of *Lecture Notes in Computer Science*, pages 131–140. Springer Berlin / Heidelberg, 2010.
- [64] L. Wietzke, O. Fleischmann, and G. Sommer. 2D image analysis by generalized Hilbert transforms in conformal space. In *ECCV (2)*, volume 5303 of *LNCS*, pages 638–649. Springer-Verlag, Berlin, Heidelberg, New York, 2008.
- [65] L. Wietzke, O. Fleischmann, and G. Sommer. The solution of the interference problem of 2d waves by means of Clifford structures. In T. E. Simos, editor, *International Conference on Numerical Analysis and Applied Mathematics, ICNAAM*, American Institute of Physics Conference Series. AIP Conference Proceedings, Melville, New York, 2009.
- [66] L. Wietzke and G. Sommer. The 2D analytic signal. Technical Report 0802, Kiel University, Department of Computer Science, 2008.
- [67] L. Wietzke and G. Sommer. The conformal monogenic signal. In Gerhard Rigoll, editor, *DAGM, Pattern Recognition*, volume 5096 of *LNCS*, pages 527–536. Springer-Verlag, Berlin, Heidelberg, New York, 2008.

- [68] L. Wietzke and G. Sommer. The relation of inverse problems and isotropic 2D signal analysis. In *Mathematics in Signal Processing 8*. Institute of Mathematics and its Applications, 2008.
- [69] L. Wietzke and G. Sommer. Nonlinear motion detection. In X. Jiang and N. Petkov, editors, *Computer Analysis of Images and Patterns, International Conference CAIP*, LNCS, pages 1122–1129. Springer, 2009.
- [70] L. Wietzke and G. Sommer. The Signal Multi-Vector. *Journal of Mathematical Imaging and Vision*, 37(2):132–150, 2010.
- [71] L. Wietzke, G. Sommer, and O. Fleischmann. The geometry of 2D image signals. In *CVPR 2009*, pages 1690–1697. IEEE Computer Society on Computer Vision and Pattern Recognition, 2009.
- [72] L. Wietzke, G. Sommer, O. Fleischmann, and C. Schmaltz. The conformal monogenic signal of image sequences. In D. Cremers, B. Rosenhahn, and A. L. Yuille, editors, *Dagstuhl Workshop: Statistical and Geometrical Approaches to Visual Motion Analysis*, volume 5604 of *LNCS*, pages 305–322. Springer-Verlag, Berlin, Heidelberg, 2009.
- [73] L. Wietzke, G. Sommer, C. Schmaltz, and J. Weickert. Analysis of the curvature tensor from the viewpoint of signal processing. In T. E. Simos, editor, *American Institute of Physics Conference Series*, volume 1046, pages 150–153, 2008.
- [74] L. Wietzke, G. Sommer, C. Schmaltz, and J. Weickert. Differential geometry of monogenic signal representations. In G. Sommer and R. Klette, editors, *Robot Vision*, volume 4931 of *LNCS*, pages 454–465. Springer-Verlag, Berlin, Heidelberg, New York, 2008.
- [75] Z. Xiaoxun and J. Yunde. Local steerable phase (lsp) feature for face representation and recognition. In *CVPR '06: Proceedings of the 2006 IEEE Computer Society Conference on Computer Vision and Pattern Recognition*, pages 1363–1368. IEEE Computer Society, 2006.
- [76] D. Zang. *Signal Modeling for Two-Dimensional Image Structures and Scale-Space Based Image Analysis*. PhD thesis, 2007.
- [77] D. Zang, L. Wietzke, C. Schmaltz, and G. Sommer. Dense optical flow estimation from the monogenic curvature tensor. In *Scale Space and Variational Methods*, volume 4485 of *LNCS*, pages 239–250. Springer-Verlag, Berlin, Heidelberg, New York, 2007.
- [78] C. Zetsche and E. Barth. Fundamental limits of linear filters in the visual processing of two-dimensional signals. *Vision Research*, 30:1111–1117, 1990.